

INVESTIGATION OF GASEOUS HYDROGEN LEAK DETECTION
USING RAMAN SCATTERING AND LASER-INDUCED BREAKDOWN
SPECTROSCOPY

By

ALLEN JOSEPH BALL

A THESIS PRESENTED TO THE GRADUATE SCHOOL
OF THE UNIVERSITY OF FLORIDA IN PARTIAL FULFILLMENT
OF THE REQUIREMENTS FOR THE DEGREE OF
MASTER OF SCIENCE

UNIVERSITY OF FLORIDA

2005

Copyright 2005

by

Allen Joseph Ball

ACKNOWLEDGMENTS

I would like to express my great appreciation to Dr. David Hahn for his guidance and shared wealth of knowledge. In addition, his understanding and enduring patience allowed me to explore my varied academic interests while still achieving a comprehensive graduate engineering education. I would also like to thank my fellow lab members, namely Kathryn Maseillo, Gregory Yoder, Prasoon Diwakar, Kibum Kim, Brian Fisher, Vince Hohreiter, Cary Henry, Brett Windom and Ben Dixon, for their assistance during my research and willingness to engage in stimulating conversation. I would like to make a special note of gratitude for Vince Hohreiter for his assistance and joint involvement in my laser-induced breakdown spectroscopy research. I want to express my appreciation to Dr. Robert Youngquist for his initiation of my research project and his aid in receiving a NASA Graduate Student Research Program Fellowship. Finally, I thank my parents, John and Beth Ball, for their continued emotional and financial support during my tenure at the University of Florida

TABLE OF CONTENTS

	<u>page</u>
ACKNOWLEDGMENTS	iii
LIST OF TABLES	vi
LIST OF FIGURES	viii
ABSTRACT	xiii
1 INTRODUCTION	1
1.1 Gaseous Hydrogen as an Energy Medium.....	6
1.2 Hydrogen Safety	7
1.3 Hydrogen Detection and Monitoring Schemes.....	10
1.3.1 Chemisorbing, Solid-state Sensors	11
1.3.2 Acoustic Hydrogen Sensors	23
1.3.3 Mass Spectrometry-based Hydrogen Detection Schemes	25
1.3.4 Optical Spectroscopic Hydrogen Detection Schemes	26
1.4 Research Motivation and Breadth	27
2 FUNDAMENTAL SCIENCE AND BACKGROUND.....	29
2.1 Raman Spectroscopy	29
2.1.1 Spontaneous Raman Scattering	29
2.1.2 Raman Scattering of Hydrogen Gas	37
2.1.3 Existing hydrogen leak detection schemes using Raman scattering	40
2.2 Laser-Induced Breakdown Spectroscopy	44
2.2.1 Plasma Generation and Emission.....	45
2.2.2 LIBS of Hydrogen Gas	47
2.2.3 Practical LIBS-based hydrogen detection schemes.....	49
3 EXPERIMENTAL METHODS.....	51
3.1 Laboratory Hydrogen Detection using Raman Spectroscopy	51
3.1.1 Experimental Apparatus	52
3.1.2 Preliminary Raman Scattering Investigation.....	59
3.1.3 Detection limit determination.....	62
3.1.4 Optical Configuration Effects on Detection Limit	67
3.1.5 Theoretical Photon Arrival Rate Determination.....	70

3.1.6	CCD detection limit studies and spectral visualization	71
3.1.7	Raman Field Detection Instrument.....	73
3.2	Laboratory Hydrogen Detection using LIBS.....	76
3.2.1	Experimental Apparatus for Comparison of Gas Phase and Substrate LIBS	77
3.2.2	Comparison of a Gaseous versus Substrate-Initiated Plasma.....	80
3.2.3	Spectral Analysis for Gas-phase and Surface LIBS	83
3.2.4	Experimental Apparatus for Surface Degradation Studies.....	89
3.2.5	Surface Degradation Investigation	93
4	RESULTS AND DISCUSSION OF HYDROGEN DETECTION BY RAMAN BACKSCATTERING	96
4.1	Preliminary Remote Hydrogen Detection Study	96
4.2	Detection Limit Determination.....	103
4.3	Optical Configuration Effects on Detection Limit	110
4.4	Limit of Detection using an ICCD.....	123
4.5	Raman Field Instrument	125
5	RESULTS and DISCUSSION OF HYDROGEN DETECTION BY LIBS.....	127
5.1	Gas-phase versus Substrate-initiated LIBS for Hydrogen Detection	127
5.2	Substrate Degradation Experiments.....	137
6	SUMMARY AND CONCLUSIONS	145
	LIST OF REFERENCES.....	150
	BIOGRAPHICAL SKETCH	157

LIST OF TABLES

<u>Table</u>	<u>page</u>
1.1 Combustion properties of gaseous hydrogen.....	7
1.2 N.A.S.A requirements for gas detection and monitoring.....	9
1.3 Diode response time constants at varying pressures.....	16
2.1 Raman shifts and absolute differential scattering cross-sections for Q-branch vibrational bands at two excitation wavelengths.....	39
2.2 Selected hydrogen atomic transition lines.....	48
3.1 All critical components and specifications for the laboratory Raman setup.....	54
3.2 Hydrogen concentrations used in preliminary Raman investigations. All samples were measured at 22° C.....	60
3.3 Wavelengths used for sample collection in preliminary scattering investigations.....	61
3.4 Concentrations used for the first detection limit study. All concentrations correspond to an ambient temperature of 25° C.....	63
3.5 Listing of attenuation factors corresponding to neutral density filters used to maintain signal linearity by excitation wavelength and concentration.....	64
3.6 Experimental configurations used for configuration detection limit studies.....	68
3.7 Components for the Raman field detection device.....	75
3.8 Listing of optical components with specifications for the laboratory LIBS apparatus for gas phase versus substrate LIBS comparison.....	79
3.9 Nitrogen and hydrogen flows used for LIBS gas phase and substrate-initiated experiments with the corresponding concentrations.....	83
3.10 Listing of optical components with specifications for the laboratory LIBS apparatus.....	91
4.1 Optical configurations examined and figure number for the scattering response.....	111

4.2 Photon arrival rate calculations by optic configuration for 355 nm incident radiation.....	119
--	-----

LIST OF FIGURES

<u>Figure</u>	<u>page</u>
1.1 Molecular structures of primary energy carriers exhibiting an increasing hydrogen to carbon ratio	4
1.2 Pd-Ni doped transistor response to hydrogen concentration under dry and humid conditions.....	13
1.3 Calibration curve for a platinum doped transistor at 30 C with error bars showing one standard deviation.....	14
1.4 Current change in Pd and Pt doped Schottky diode in response to changing hydrogen partial pressures at various temperatures.....	15
1.5 Voltage across a potentiometric sensor for increasing percentages of hydrogen in air by volume	18
1.6 Response time of a potentiometric hydrogen sensor to the introduction of hydrogen at various concentrations in air	18
1.7 Detection response of a palladium micromirror as a function of hydrogen concentration.....	20
1.8 Response time a palladium micromirror as a function of hydrogen concentration	20
2.1 Electrostatic potential maps showing the induction of an oscillating dipole in a symmetric diatomic molecule due to incident electromagnetic radiation. Charge density, initially uniform, is displaced upon interaction with the oscillating electric field of the incident radiation.....	30
2.2 Energy level diagram showing a comparison of elastic scattering transitions with inelastic Raman scattering transitions.	32
2.2 Arbitrary Raman spectrum exhibiting the frequency and intensity relationship between elastically scattered and inelastically scattered radiation.....	34
2.3 Signal as a function of hydrogen concentration for Alder-Golden et al. hydrogen leak detection system. Dotted curves represent RMS noise levels.	43
2.4 Example spectrum showing the H α line from hydrogen emission.....	49

3.1 Experimental apparatus used for laboratory hydrogen detection limit investigations	53
3.2 Stainless steel sample chamber used for all Raman hydrogen detection experiments	55
3.3 Photograph of collection optics used in laboratory remote Raman scattering experiments	57
3.4 Photograph of the complete laboratory setup for remote Raman scattering experiments	58
3.5 PMT signal showing the Raman scattering signal at 415.91 nm and the offline measurements with the average offline measurement	62
3.6 Scattering response at 355 nm showing a linear regression used for LOD determination	66
3.7 ICCD spectrum showing the Raman line at 415.91 nm for a pure hydrogen sample at atmospheric pressure	73
3.8 Optical head for the Raman field detection system showing the layout of all optic components	74
3.9 Portable Raman field detection instrument for hydrogen detection showing the collection optics, laser, power supply, and detection instrumentation	76
3.10 Laboratory LIBS configuration used for the study of hydrogen detection	78
3.11 A sample raw LIBS emission spectrum from a stainless steel substrate-initiated plasma in 16.62% H ₂ in nitrogen atmosphere	84
3.12 Two sample emission spectra showing the absolute analyte emission and the absolute blank emission in the H _α region for a stainless-steel substrate initiated plasma	86
3.13 Absolute H _α peak achieved as a result of blank subtraction. This peak exhibits a proportional response to concentration	87
3.14 Laboratory LIBS configuration used for the study of hydrogen detection	90
3.15 Three mass flow controllers used for control of sample concentrations during hydrogen detection studies	92
3.16 Collection optics used for collection of plasma emission from inside the sample chamber	92
3.17 Photograph of the LIBS laboratory system used for investigations of hydrogen detection	93

4.1	PMT scattering signals recorded for ten wavelengths around the Raman Stokes line for hydrogen at 10 psig in the sample cell.....	97
4.2	PMT scattering signals recorded for ten wavelengths around the Raman Stokes line for hydrogen at 20 psig in the sample cell.....	98
4.3	PMT scattering signals recorded for ten wavelengths around the Raman Stokes line for hydrogen at 30 psig in the sample cell.....	98
4.4	PMT signals showing scattering response on the Raman line at 415.91 nm and off the Raman line at 413.91 nm.	99
4.5	Absolute scattering response for decreasing hydrogen concentrations in one preliminary hydrogen detection trial.	101
4.6	Raman scattering response for preliminary hydrogen detection at 6.58m as a function of hydrogen concentration.	102
4.7	Raman scattering signal and one offline measurement for 100% hydrogen by volume at atmospheric pressure excited by 355 nm incident radiation.....	104
4.8	Raman scattering signal and one offline measurement for 100% hydrogen by volume at atmospheric pressure excited by 532 nm incident radiation.....	104
4.9	Absolute Raman scattering signal and offline noise signal for excitation of the 100% by volume hydrogen sample with 355 nm incident radiation.....	106
4.10	Absolute Raman scattering signal and offline signal for excitation of the 100% by volume hydrogen sample with 532 nm incident radiation.	106
4.11	Absolute Raman scattering signal and offline signal for excitation of the 3.125% by volume hydrogen sample with 355 nm incident radiation.	107
4.12	Absolute Raman scattering signal and offline signal for excitation of the 3.125% by volume hydrogen sample with 532 nm incident radiation.	108
4.13	Raman scattering response to hydrogen concentration for two excitation wavelengths.	109
4.14	Enlarged section of Figure 4.13 to show Raman scattering response to hydrogen concentration for two excitation wavelengths below a hydrogen concentration of 25% by volume.....	109
4.15	Scattering response for hydrogen at an incident wavelength of 355 nm, a pulse energy of 125 mJ/pulse, and collection lens diameter of 2”.....	112

4.16 Scattering response for hydrogen at an incident wavelength of 355 nm, a pulse energy of 125 mJ/pulse, and collection lens diameter of 2" for concentrations below 25% by volume.	113
4.17 Scattering response for hydrogen at an incident wavelength of 355 nm, a pulse energy of 250 mJ/pulse, and collection lens diameter of 2".....	114
4.18 Scattering response for hydrogen at an incident wavelength of 355 nm, a pulse energy of 250 mJ/pulse, and collection lens diameter of 2" for concentrations below 25% by volume.	114
4.19 Scattering response for hydrogen at an incident wavelength of 355 nm, a pulse energy of 125 mJ/pulse, and collection lens diameter of 4".....	115
4.20 Scattering response for hydrogen at an incident wavelength of 355 nm, a pulse energy of 125 mJ/pulse, and collection lens diameter of 4" for concentrations below 25% by volume.	116
4.21 Scattering response for hydrogen at an incident wavelength of 355 nm, a pulse energy of 250 mJ/pulse, and collection lens diameter of 4".....	117
4.22 Scattering response for hydrogen at an incident wavelength of 355 nm, a pulse energy of 250 mJ/pulse, and collection lens diameter of 4" for concentrations below 25% by volume.	118
4.23 Scattering responses for four optical configurations examined with 355 nm incident radiation. The lines exhibit the linear regression for each response.....	119
4.24 Scattering response at 12.5% hydrogen by volume versus the derived scaling parameter.	120
4.25 Scattering response for hydrogen at an incident wavelength of 532 nm, a pulse energy of 125 mJ/pulse, and collection lens diameter of 4".....	121
4.26 Scattering response for hydrogen at an incident wavelength of 532 nm, a pulse energy of 250 mJ/pulse, and collection lens diameter of 4".....	122
4.27 ICCD spectrum showing the Raman line for at 415.91 nm for a 100% sample of hydrogen at atmospheric pressure.	123
4.28 Scattering response for hydrogen at an incident wavelength of 355 nm as determined using an ICCD.	124
4.29 Scattering response for hydrogen at an incident wavelength of 355 nm as determined using an ICCD for concentrations below 25% by volume.	125
5.1 LIBS spectra of candidate substrate materials showing the H _α line for hydrogen from ambient water vapor at 1.5 % by volume.	129

5.2	Example plasma emission spectra for 65 ppm and 325 ppm hydrogen concentrations with the corresponding scaled background spectra.	131
5.3	Background subtracted LIBS spectra for four experimental hydrogen concentrations in nitrogen.	131
5.4	Gas phase and stainless steel LIBS emission response to hydrogen concentration below 4.4% by volume.	132
5.5	Gas phase and stainless steel LIBS emission response to hydrogen concentration. Linear regressions are shown for data below 1.13% hydrogen by volume.	133
5.6	Plasma electron densities at three sample hydrogen concentrations for substrate and gas phase initiated plasmas.	135
5.7	H _α emission for gas phase plasma formation.	136
5.8	Stainless steel surface crater formed by ablation after repeated detection limit studies at the same substrate location.	138
5.9	Hydrogen P/B ratios as a function of the total number of laser shots for stainless-steel initiated LIBS.	140
5.10	Stainless steel substrate crater after ablation by 18000 laser shots in a hydrogen and nitrogen atmosphere.	141
5.11	Average hydrogen P/B ratios as a function of the total number of laser shots for stainless-steel initiated LIBS.	142
5.12	Stainless steel substrate craters after ablation by 45,000 laser shots in a hydrogen and nitrogen atmosphere.	143

Abstract of Thesis Presented to the Graduate School
of the University of Florida in Partial Fulfillment of the
Requirements for the Degree of Master of Science

INVESTIGATION OF GASEOUS HYDROGEN LEAK DETECTION USING
RAMAN SCATTERING AND LASER-INDUCED BREAKDOWN SPECTROSCOPY

By

Allen J. Ball

May 2005

Chair: David Hahn

Major Department: Mechanical and Aerospace Engineering

Gaseous hydrogen is being widely promoted as the future primary energy carrier to replace current hydrocarbon fuels. Governments and industries are investing in research and development programs to develop hydrogen production, transport and storage technologies. In addition, hydrogen gas is currently used in chemical processing and aerospace applications. Hydrogen gas is combustible with a wide flammability range of about 4 to 75 percent, a low ignition energy, and a low gas density. With the expanding application of hydrogen gas coupled with its highly combustible nature, focus must be placed on safety. Detection and monitoring technologies are needed which can provide low limits of detection, high sensitivity, a wide detection range, fast response times and ease of implementation to ensure public safety. Current technologies such as chemisorbing sensors, acoustic sensors and mass spectrometry-based systems exhibit limitations in one of these metrics. This work examines the use of Raman scattering and

laser-induced breakdown spectroscopy as quantitative and practical hydrogen detection techniques.

Hydrogen detection by Raman scattering was examined in a remote, backscattering format in a laboratory setting. Binary mixtures of hydrogen and nitrogen, excited by a laser, were used to study the limit of detection and sensitivity for hydrogen detection by Raman scattering. In addition, various configurations of collection optics, laser pulse energies, and excitation wavelengths were examined to improve limits of detection by reducing noise and increasing photon collection efficiency. Linear responses were observed with a lowest achieved detection limit of 0.76% hydrogen by volume. Scaling in the response as a function of pulse energy and the square of the diameter of the collection optics was observed at individual hydrogen concentrations as expected from Raman theory. A field detection system based on Raman scattering was also constructed.

Laser-induced breakdown spectroscopy was also examined as a real-time, practical hydrogen point sensing technique. Laser pulses of 100 mJ and 55 mJ were used to create a gas phase breakdown in a sample gas stream and a solid substrate-initiated breakdown which entrained sample gas, respectively. Six metals were examined as substrates for surface breakdowns. Stainless steel was selected and a comparison of the responses of both LIBS formats was examined for changing hydrogen concentrations in a nitrogen background by measuring the H_{α} emission line at 656.28 nm for hydrogen. Both techniques exhibited linear responses with a substrate detection limit of 16 ppm and a gas phase detection limit of 23 ppm. Overall, both Raman scattering and LIBS were concluded to be viable techniques for practical hydrogen sensing, exhibiting high sensitivities and fast response times with a format well-suited for field implementation.

CHAPTER 1 INTRODUCTION

Increasing concern with current energy sources, specifically fossil fuels, has prompted the industrial and scientific communities to examine other sources for the growing energy needs of society. Fossil fuels have been the staple source of energy for most mechanical and electrical applications since before industrialization. Although fossil fuels are in widespread use with a large supporting infrastructure, there are many problems with dependence on fossil fuels. The consumption of oil, the principal fossil fuel in use, is increasing at an unprecedented rate. For the United States, this is of great concern. The United States already consumes 26 percent of the world oil output (Dunn 2002). An almost 50 percent increase is expected in oil demand by the year 2025 (DOE 2004). Coal consumption is expected to rise by 30 percent over the next twenty years (Dunn 2002). Petroleum, natural gas, and coal are all resources in limited supply as a result of their long geologic formation process. This limited supply coupled with such significant increases in consumption raises concerns about the future availability of fossil fuel energy sources.

A second important shortcoming of fossil fuels is their detrimental effect on the environment. Energy extraction from fossil fuels occurs principally through combustion. This combustion, whether it be in a power generating cycle, heat engine or any other fossil fuel based energy process produces many forms of pollution. The most notable pollution occurs in the form of gaseous emissions. Gases such as nitrous oxides, carbonaceous oxides, and sulfuric oxides are all emitted during combustion of fossil

fuels. A focus has been placed on carbon dioxide due to its purported effect on global climate change. More than 277 billions tons of carbon have been admitted into the atmosphere since 1751 due to fossil fuel combustion (Marland et al. 2000). Global carbon emissions are currently around 6.1 billion tons annually and expected to increase to 9.8 billion tons by 2020, thereby accelerating pollution and associated climate change (Dunn 2002). Over the span of history, carbon dioxide concentrations have increased from 280 to 369 parts per million (ppm) by volume, a 31 percent increase and the highest point in 420,000 years (Scripps 2000). Projections for the year 2100 show carbon dioxide levels from 650 to 970 ppm (Intergovernmental Panel on Climate Change [IPCC] 2001). Among sources, gaseous pollution from the petroleum-based transportation sector are rising faster than any other (Melaina 2003). In the U.S., 33 percent of the carbon emissions are from this sector (EIA 2000). In addition to these harmful gaseous species, a number of biologically hazardous metallics, particulate matter and organics are emitted into the air due to combustion processes. Particulate matter alone is responsible for 500,000 premature deaths annually (Dunn 2002). These species eventually precipitate out of the air causing pollution of the soil and aqueous environments. Direct contamination of the soil and aqueous environments is also achieved when solid carbonaceous byproducts and any associated impurities are eliminated after a combustion process. In addition to the effects of fossil fuel combustion, the procurement of fossil fuels is extremely taxing on the environment.

A third shortcoming of fossil fuels relates to the socioeconomic climate. Sustainable oil reserves are under the control of a limited number of countries yet fossil fuel dependence has pervaded most of the world. Therefore, any political disruptions or

strained international relations involving these countries controlling the reserves greatly effects the availability of the world's energy supply. The bulk of the petroleum reserves, some 65 percent, are located in the Middle East (EIA 2000). As of 2004, oil importation supplies 55 percent of the oil required for the U.S. (DOE 2004), with that number expected to rise to 72 percent if current trends continue (Dunn 2002). A similar rise from 56 to 76 percent in 2020 is expected for all industrial nations (UNDP 2000). This concentration of resources and dependence on importation can jeopardize energy supplies for a majority of the world in changing political climates.

While a continued discussion of the problems associated with current energy sources is beyond the scope of this document, the above noted increasing concerns associated with fossil fuel usage and the continuing desire to develop a clean, renewable energy source have resulted in an increased demand for new energy carriers. Energy consumption by humans in the twentieth century was ten times that of their ancestors in the previous 1000 years (Dunn 2002). This is a trend that is only expected to increase exponentially. A rise of around 60 percent in global energy consumption is expected over the next 20 years alone (EIA 2001). With regard to past energy carriers, there has been a trend of shifting from solids to liquids to gases as the principal form of energy since the mid-19th century (Ausubel 2000). Natural gas has become the second-leading energy source for power generation, overtaking coal in 1999, making it the fastest-growing fossil fuel in terms of use (Ausubel 2000). This shift towards natural gas use follows a shift towards increased hydrogen-to-carbon ratios in fuels. This trend is illustrated in Figure 1.1 with a comparison of the molecular structure of some of the modern fuels.

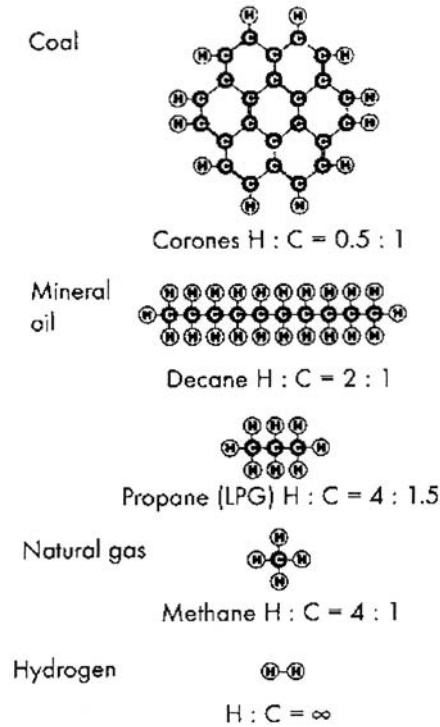


Figure 1.1 Molecular structures of primary energy carriers exhibiting an increasing hydrogen to carbon ratio. Source: Winter 2000

If wood is included as an energy source, the hydrogen-to-carbon ratio has gone from between 1:3 to 1:10 for wood to 1:2 for coal, 2:1 for oil, and finally 4:1 for natural gas during this process that has been entitled “decarbonization.” In the span of time, there was a six fold increase in the ratio of hydrogen-to-carbon between 1860 and 1890 (Dunn 2002). Based on these two trends, hydrogen gas seems to be the conclusion to a line of energy carriers and can aid in meeting the growing energy demands of human consumption.

Use of hydrogen is already widespread in the industrial processing and aerospace industries. Hydrogen use in the metallurgical, chemical, and ceramics industries comprises almost 50 percent of the 500 billion cubic meters of annual hydrogen consumption (Elam et al. 2003). About 80 billion cubic meters of hydrogen is produced in the U.S. annually (Dunn 2002). As far back as the Second World War, fuel shortages

prompted the U.S. military to examine hydrogen as a viable fuel (Hoffman 2001). As a result, liquid hydrogen became the primary fuel source for the U.S. space shuttle program of the National Aeronautics and Space Administration (NASA) and several other global space initiatives. Fuel cells are being designed and implemented to run on hydrogen fuel. This application was already established in aerospace as hydrogen has been used in fuel cells since the 1950s for space applications (Dunn 2002). These few examples illustrate that hydrogen is not just a future energy carrier, but rather an established energy source.

Future use of hydrogen as a fuel is almost a certainty with government and industry embarking on extensive hydrogen plans. The International Energy Agency (IEA) commissioned the Production and Utilization of Hydrogen program in 1977, referred to as the Hydrogen Agreement, to promote hydrogen use and hydrogen production and distribution research (Elam et al. 2003). The U.S. government has proposed \$1.2 billion for a New Hydrogen Fuel Initiative (DOE 2004). Continued fuel cell development includes over a 100 companies interested in commercializing fuel cells for applications as varied as cell phones, soda machines, laptop computers, vehicles, offices, factories, and homes (Dunn 2002). Automobile and fuel companies are spending between \$500 million and \$1 billion annually on research and development programs for hydrogen (Dunn 2002).

The expanding use of gaseous hydrogen as an energy source means that hydrogen storage and handling will have a growing importance. Hydrogen is a flammable gas and therefore safety issues arise with any handling and storage applications. The use of a combustible energy carrier first requires an understanding of its ignition, combustion, and

potential detonation behavior (Fischer and Eichert 1998). For this reason, a brief examination of hydrogen gas properties, with focus on safety, is now given.

1.1 Gaseous Hydrogen as an Energy Medium

Atomic hydrogen is the most basic element, composed of one electron and one proton, and accounts for more than 90 percent of the universe by mass (HTAP 1999). Elemental hydrogen has a low atomic weight of approximately 1.008 g/mol. As a result, both its melting temperature and vaporization temperature are low, -259 °C and -253 °C, respectively. Therefore hydrogen exists as a gas under most working conditions. Gaseous hydrogen is composed of symmetric, diatomic molecules with one covalent bond adjoining the two atoms. Gaseous hydrogen is non-toxic, has no color, odor, or taste, and thus is imperceptible by a person (McAuliffe 1986) The addition of odorants to hydrogen has been considered to aid in detection of hydrogen leaks, but these odorants can poison fuel cells and are often too large to diffuse through leaks easily navigated by the small hydrogen molecule (Romm 2004). The low molecular weight of the diatomic molecule, approximately 2.016 g/mol, means that hydrogen gas is much lighter than air, thus hydrogen diffuses upward and burns upward in contrast with many other gaseous fuels (McAuliffe 1986). In addition, hydrogen flames are nearly invisible (Romm 2004). The combustible properties of hydrogen gas are of interest for both its use as a fuel and for safety. Table 1.1 gives hydrogen properties that are associated with combustion and thus pertinent to safety considerations. As observed in the table, hydrogen has a higher heating value almost three times that of methane and propane and a similar ratio in comparison to gasoline (Tan et al. 2003). Therefore, hydrogen is highly energetic fuel by mass and appears to be an improvement over conventional fuels.

Table 1.1 Combustion properties of gaseous hydrogen.

Parameter	Hydrogen H ₂	Methane CH ₄	Propane C ₃ H ₈
Gas Density at STP ^a (kg/m ³)	0.0838	0.6512	1.87
Self-ignition temperature (K)	858	813	760
Minimum ignition energy in air (mJ)	0.02	0.29	0.26
Ignition limits in air (vol-%)	4-75	5.3-15	2.1-9.5
Flame temperature in air ^b (K)	2318	2148	2385
Detonation limits in air (vol. %)	13-59	6.3-14	
Detonation velocity in air ^b (km/s)	2	1.8	1.85
Detonation overpressure (bar)	14.7	16.8	18.25
Lower heating value (kJ/g)	119.93	50.02	46.35
Higher heating value (kJ/g)	141.86	55.53	50.41
Gas Specific heat ^a (J/gK)	14.89	2.22	1.67
Velocity of sound in gas at STP ^a (m/s)	1294	448	260
Stoichiometric mixture in air (vol. %)	29.53	9.48	4.03
Diffusion coefficient in air at STP ^a (cm ² /s)	0.61	0.16	0.12
Explosion energy ^c at STP ^a (kg TNT/m ³)	2.02	7.03	20.5
Explosion energy ^c (g TNT/g fuel)	24	11	10
Explosion energy ^c (g TNT/kJ)	0.17	0.19	0.2

^a STP: standard temperature and pressure, 293.15 K, 1.013 bar.

^b Stoichiometric mixture

^c Theoretical maximum; actual value approx. 10 % of theo. maximum

Source: Hord 1976

This benefit is negated by a much lower gas density for hydrogen as seen in Table 1.1 in comparison to methane and propane. As a result, hydrogen must be compressed to higher levels than other gaseous fuels to achieve similar energy extraction from comparable fuel volumes. These high pressures can pose many safety risks for storage and handling processes. Another difference seen in Table 1.1 between hydrogen and the gaseous hydrocarbons is the broad flammability range in air. Hydrogen can be ignited over a concentration range of about 4 to 75% by volume. Coupled with a low ignition energy and higher explosion energy by mass, uncontained hydrogen fuel presents a formidable safety hazard.

1.2 Hydrogen Safety

The previous description of hydrogen as a fuel demonstrated that hydrogen is a highly energetic and combustible gas. It is for this reason that hydrogen is seen as a

promising fuel and why care must be taken in its handling and storage. While hydrogen use is prevalent in industrial applications, its expansion in society means an increased focus on safety. Undetected hydrogen leaks already comprise 22 percent of current hydrogen accidents (Romm p106). A similar percentage in the public setting would be unacceptable. “Hydrogen safety is an issue of every aspect from production to utilization and continues to be of the utmost importance; not only to those researching, designing and working with it; but to the general public, local authorities, insurance agents, etc.” (p 603 Elam et al.2003).

Monitoring and leak detection must be a key focus of all hydrogen handling, storage and transmission activities. One projection is that the transition to hydrogen would first make use of the existing natural gas network of pipelines to achieve distribution (Dunn 2002). As exhibited in an earlier section, hydrogen has a much lower gas density than methane thus creating the possibility for failure of joints and seals in existing pipeline networks. Hydrogen can be safely transported in specifically designed pipelines. This is demonstrated by the lengthy hydrogen pipelines in some of the leading industrial nations: 210 km in Germany, 400 km from France to Belgium, and over 720 km throughout the U.S. (Amos 1998). Construction of such pipelines for widespread use would not be feasible in the initial transition to hydrogen and even these pipelines have inherent risk associated with the high pressure at which they are operated. Hydrogen also tends to degrade materials over time by processes such as embrittlement and destruction, induced crack generation, blistering, flakes, and cold-cracking of welded joints (Goltsov 2002). Normally, molecular hydrogen should be relatively inert in pipelines but with very pure and compressed hydrogen, as NASA has determined,

embrittlement is a possibility especially around pipeline welds (McAuliffée p50). These effects of hydrogen on materials have similar safety implications for storage vessels. Safe and economic transportation of hydrogen is key to hydrogen becoming the next energy carrier (Dunn 2002). As a result, hydrogen leak monitoring is a necessity for safety.

Governments recognize the need to address hydrogen safety as an essential element of their hydrogen development programs. One of the guiding principles of the IEA Hydrogen Agreement is that “barriers, both technical and non-technical, to the introduction of hydrogen are being reduced through advances in renewable energy technologies and hydrogen systems including progress in addressing hydrogen storage and safety concerns” (Elam et al. 2003). In the U.S. Hydrogen Initiative, phase one requires the demonstration of “critical path” technologies and safety assurance before any commitment is made to a hydrogen infrastructure (DOE 2004). N.A.S.A. has outlined requirements for hydrogen gas monitoring in the space shuttle program as shown in Table 1.2.

Table 1.2 N.A.S.A requirements for gas detection and monitoring.

Performance criteria	Basic requirements ^a
Accuracy (% error)	<10% or 5 ppm, whichever is less
Precision (% deviation)	<5% or 3 ppm, whichever is greater
Detection limit (ppm)	H ₂ : 25; He: 100; O ₂ : 25; Ar: 10
Response time (sec)	10 (0 ppm raised to 500 ppm)
Recovery time (sec)	30 (500 ppm lowered to 0 ppm)

^aRequirement for all gases, unless otherwise stated.

Source: Ottens 2002.

Hydrogen leak detection and monitoring is thus critical not only for safety, but for the expansion of hydrogen as an energy carrier. Technologies are needed to meet this

demand for monitoring that can provide reliable, continuous detection of low hydrogen concentration levels for all handling, transport and storage applications

1.3 Hydrogen Detection and Monitoring Schemes

The safety concerns regarding the handling and transport of hydrogen have resulted in the examination of many detection schemes for hydrogen monitoring applications. The predominance of detection systems, either currently available or under investigation, can be classified into four categories. The first category is chemisorbing solid-state sensors which use a thin-film surface that interacts chemically with hydrogen and in response undergoes a change in one of several physical properties. The second category encompasses several types of acoustic sensors. Acoustic hydrogen sensors use the difference in density and speed of sound between hydrogen and other gases to achieve detection. The third classification for hydrogen detection schemes are those based on mass spectrometry. In these detection systems, hydrogen ions are separated based on mass in a magnetic field and a resulting mass spectrum is used for identity and quantification. The final category is optical spectroscopic methods. This includes the methods that are the focus of this paper. Optical spectroscopic techniques may use a range of identifying characteristics, such as atomic or vibrational transitions. Atomic emission schemes use an excitation source to induce atomic transitions or complete ionization in a sample of hydrogen gas. As the molecules of hydrogen return to their lowest energy state after excitation or ionization, electromagnetic radiation is released and collected to produce an emission spectrum. Using known emission schemes for hydrogen, the presence and concentration of hydrogen can be determined. In contrast, vibrational schemes, such as Raman scattering, use a quantum of energy to excite a vibrational mode and measure the subsequent relaxation through photon emission to

determine the presence and concentration of hydrogen. There are many devices currently available or under development that fall into these four detection categories. A brief comparison of the technologies available in each category is now given. In addition, important metrics of performance such as detection limit, sensitivity, response time, recovery time, and detection range are highlighted.

1.3.1 Chemisorbing, Solid-state Sensors

This is a broad category of sensors comprising the bulk of hydrogen sensing technologies available. These sensors are often classified as point gas sensors. The basic principle on which these hydrogen sensors function is that hydrogen concentration in a sample gas volume can be detected by monitoring the change in the physical properties of a chemisorbing film layer. There are numerous chemisorbing layers that have been developed with a variety of compositions but in general, the layer is doped with a metal, usually palladium, which is responsible for interacting with gaseous hydrogen in a surrounding sample volume. These metallic layers adsorb hydrogen to form hydrides when in contact with free hydrogen gas thus changing their solid crystal structure (Bevenot 2000). This crystal modification induces changes in the electrical, optical and acoustic properties of the chemisorbing layers. Chemisorbing sensors can be divided into three groups based on which one of the three physical properties is used for sensing (Dong 2003). The combination of composition and the type of solid-state sensor has created a number of devices. The remainder of this section presents examples from each category of chemisorbing sensors for the purpose of examining their metrics and limitations.

Solid-state semiconductors with a hydrogen sensitive layer are the most common of the chemisorbing hydrogen sensors. These sensors exhibit a change in electrical

conductivity proportional to the amount of hydrogen adsorbed onto the surface layer at equilibrium (Scharnagl et al. 2001). The first semiconductor hydrogen sensor can be found in 1975 with the MOSFET transistor proposed by Lundstrom and Svensson. As a result of this development, the use of palladium doped MOS field effect transistors for hydrogen detection has been a common practice for more than 25 years (Scharnagl et al. 2001). While commonly used for sensing, these sensors have drawbacks. Usually conductance sensors operate at several hundred degrees centigrade making them unpractical for use as field detection device (Scharnagl et. al. 2001). Also, due to the interaction of the surface with hydrogen, these sensors show reduced detection ability with ageing (Tardy 2004). Blistering in the palladium layers of MOS transistors at high hydrogen concentrations is one effect of ageing that limits detection range (Armgarth 1982). Chemisorbing semi-conducting sensors also show a significant response and recovery time due the requirement of adsorption and desorption of hydrogen on the active surface. A few examples of recently developed semi-conducting hydrogen sensors are now presented to examine improvements and continued limitations in these types of sensors.

Scharnagl et al. tried to combat blistering of past semi conducting transistor sensors by using alloys of Pd-Ni and Pd-Ag as the sensitive layer, thereby stabilizing the palladium. While effective in stabilizing the palladium layer, a constant sensor temperature of either 25 or 100° C was necessary for detection and the transistors exhibit lengthy response times. A graph of the Pd-Ni sensor response to three concentrations of hydrogen in synthetic air is shown in Figure 1.2. The linear response on a semi logarithmic scale should be noted. A decrease in signal response is observed with

increasing hydrogen concentration. This shows that saturation can be achieved with this sensor thus limiting detection range.

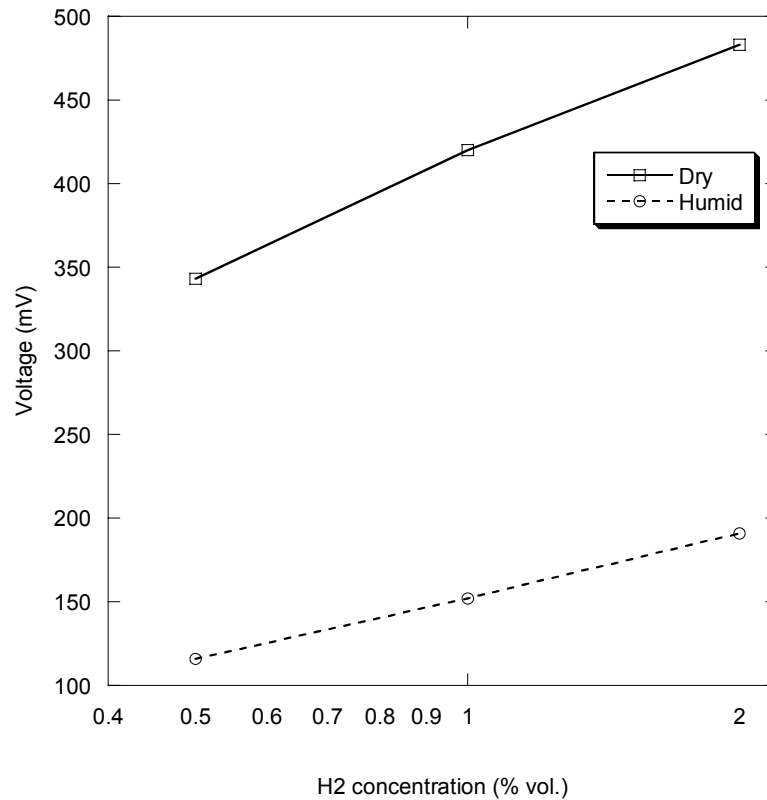


Figure 1.2 Pd-Ni doped transistor response to hydrogen concentration under dry and humid conditions. Source: Scharnagl et. al. 2001

For a 0.1% by volume mixture of hydrogen and synthetic air, an 80% signal took 10 seconds to achieve for the Pd-Ni doped transistor. In addition to the response time, 40 minute gas cycles were required due to saturation and recovery of the Pd-Ni layer with more than 40 minutes required for hydrogen gas concentrations higher than 0.1%. For 1% hydrogen, only 50% of the maximum signal was achieved in 20 seconds while equilibrium took 20 minutes. Another drawback noted for the Pd-Ni layer was a strongly reduced response with humid sample gas. For the Pd-Ag layer, similar response times were observed but the response levels were lower at 100 °C. Baseline drift was also

observed after repeated gas exposure. While successful at showing stabilized palladium alloy layers could detect hydrogen ultimately over a concentration of 0.1%-2% by volume, the Pd-Ag layer could not detect hydrogen at elevated temperatures or maintain a constant signal and both layers exhibited multi-second response times.

Platinum and iridium have also been examined as chemiabsorbing dopants for semiconducting transistor devices (Schnargl, Karthigeyan et al. 2001). Platinum exhibited a saturation tendency, like palladium, to increasing hydrogen concentration as shown by a decrease in signal rise in Figure 1.3.

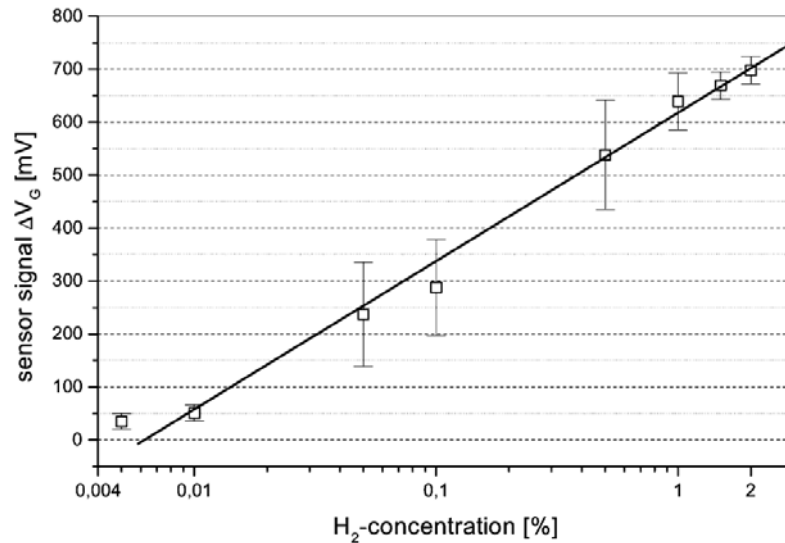


Figure 1.3 Calibration curve for a platinum doped transistor at 30°C with error bars showing one standard deviation. Source: Schnargl, Karthigeyan et al. 2001

A 90% signal response for each concentration was observed within 10 seconds. Long recovery times for desorption were observed with almost 3 hours needed for 2% by volume concentrations of hydrogen in synthetic air. The iridium doped transistor exhibited small signal responses at 1000 parts per million (ppm) and 2% hydrogen samples with long response times of more than 40 minutes and 15 hours respectively. A

return to baseline levels after exposure wasn't achieved in 15 hours. In addition, humidity was found to decrease platinum response while increasing iridium signals.

Kang and Gurbuz explored the use of another chemisorbing semiconductor type, the Schottky diode, for hydrogen detection. Two GaAs Schottky diodes, one doped with palladium and the other with platinum, were constructed and examined for hydrogen detection ability. Schottky diodes like all diodes control current flow. With the doped diodes, changes in current flow were observed with changes in ambient hydrogen concentration due to the adsorption of the hydrogen into the surface layer. Figure 1.4 shows the current response to changes in hydrogen partial pressures.

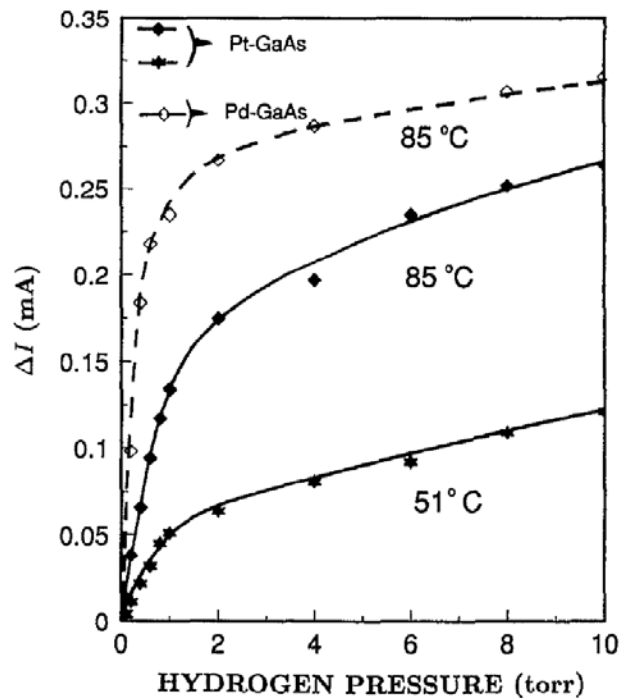


Figure 1.4 Current change in Pd and Pt doped Schottky diode in response to changing hydrogen partial pressures at three temperatures. Source: Wang and Gurbuz 1994.

While the Schottky diodes did exhibit a response to changing hydrogen concentrations, a tendency toward saturation is again observed for both sensors. Above room temperature

operating temperatures were also required for sensor operation. Similar to other semiconducting sensors, response times were in the multiple second range, decreasing for larger concentrations. Table 1.3 gives the time constants for both diodes at various partial hydrogen pressures.

Table 1.3 Diode response time constants at varying pressures.

Sensor	Pressure (Torr)	Time constant (s)
Pd-GaAs	1	16
	9	4
Pt-GaAs	1	104
	3	98
	5	71
	7	62
	9	57

Source: Kang and Gurbuz 1994

Between the two sensors, the palladium-doped diode showed better sensitivity than platinum diode to low hydrogen concentration, as shown by the slope in Figure 1.4, as well as a quicker response time.

Similar behavior to the chemisorbing semiconductors presented has been demonstrated with many other metallic-doped active layer configurations. Uwira et al. reported the use of a palladium-doped copper phthalocyanine (Cu-Pc) p-type semiconductor to achieve detection limits around well below 1 ppm at 95 °C and multiple minute response times. Large hydrogen concentrations up to 1000 ppm lead to saturation with a conductance decrease of more than 90%. Shukla et al. reported hydrogen detection with a tin oxide film semiconductor over a range of 1-4% hydrogen by volume. A maximum sensitivity of 394% was observed at 4% by volume and a 94% sensitivity at 1% by volume at room temperature. No information on response time was given. Wong et al. described the use of carbon nanotubes impregnated into a thin-layered Pd/CNTs/n⁺-Si structure. The carbon nanotubes are supposed to aid in hydrogen molecular adsorption

into the surface prior to dissociation by palladium. When examined in the presence of hydrogen gas at room temperature and 80 °C, a reduction in current through the composite sensor was observed in a fashion similar to Schottky diodes. While Wong et al. demonstrated the ability to detect the presence of hydrogen and commented on absorption mechanisms, proportionality to concentration was not examined and further research is required. Additional surface dopants such as Si_3N_4 (Dobos 1984), Ta_2O_5 (Dobos 1984), $\text{Al}_2\text{O}_3\text{-SiO}_2$ (Lundstrom and Svensson 1985), Al_2O_3 (Okuyama 1997), $\text{SiO}_2\text{-SiC}$ (Arbab 1993; Chen 1997), SiC (Baranzahi 1996), ZnO (Basu 1994), TiO_2 (Kobayashi 1994), and diamond thin film (Kang 1995) have all been used for chemisorbing semiconductors. Overall semiconducting devices with chemisorbing layers have all exhibited the ability to detect low concentrations of hydrogen with high sensitivity but they all suffer from multi-second response times, limited detection range, saturation and a lack of robustness due to surface degradation, poisoning and operating temperature dependency. In addition, the small sample volumes examined by these point gas sensors means entire arrays of sensors would be needed for any macroscopic hydrogen monitoring scheme.

A second type of chemisorbing electrical solid state sensors in use is solid electrolytes with variable ionic conductivity. An example of this sensor is described by Maffei and Kuriakose and entails the use of a hydronium Nasicon disc, a conducting electrolyte, with two electrodes, one silver-based and one palladium. As with the other sensors, hydrogen adsorption changes the electrical characteristics of the potentiometric sensor. Figure 1.5 shows the response of the sensor in air for an increasing volumetric percentage of hydrogen.

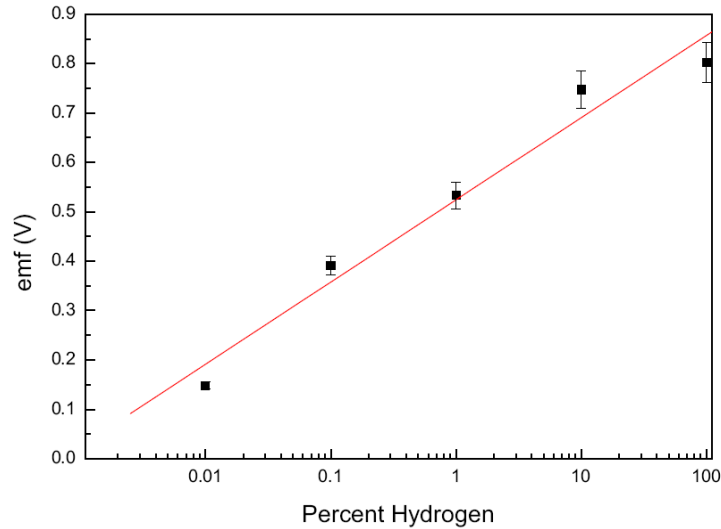


Figure 1.5 Voltage across a potentiometric sensor for increasing percentages of hydrogen in air by volume. Source: Maffei and Kuriakose 2004

As with the semiconducting sensors, a semi logarithmic scale was presented due to the decreasing signal change of the chemisorbing layer with increasing hydrogen concentration. In contrast to the semiconducting sensors, results were presented up to 100% hydrogen and saturation was not achieved. Figure 1.6 shows the response time of the sensor to brief hydrogen exposures of various concentrations.

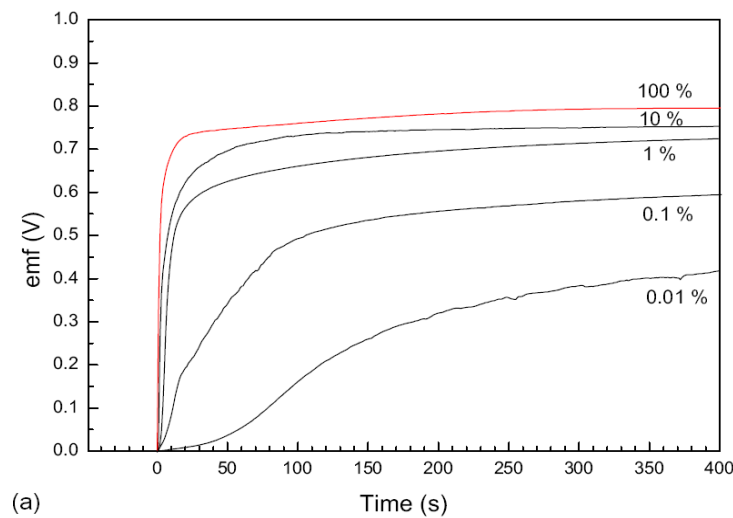


Figure 1.6 Response time of a potentiometric hydrogen sensor to the introduction of hydrogen at various concentrations in air. Source: Maffei and Kuriakose 2004

An extremely short response time is seen for high concentrations due to the increased rate of adsorption associated with high concentrations, but response time recedes to over 200 seconds for low concentrations.

A second form of the chemisorbing solid-state sensor used for hydrogen detection is based on measuring the change in optical properties of the active layer. As with the electrical property-based sensors, palladium is the metallic surface dopant used most commonly. Several configurations have been developed based on this principle namely palladium doped micromirrors (Bevenot 2000, Butler 1993), surface plasmon resonance (Chadwick 1993, Bevenot 2002), intensity variations of electrochromatic materials (Ito 1992, Hamagami 1993), interferometric measurements (Davis 1986, Bearzotti 1982), and fiber Bragg gratings (Peng 1999, Tang 1999). Palladium micromirrors and surface plasmon resonance optical fibers are now examined to exemplify the characteristic responses of chemisorbing optical hydrogen sensors.

Bevenot et al. 2000 developed a palladium micromirror sensor which exhibits a change in reflectivity to an incident diode laser due to adsorption of the hydrogen. The micromirror was mounted on the end of an optical fiber and exposed to a range of hydrogen concentration from 1 to 100% by volume. Figure 1.7 shows the response of the sensor as a function of hydrogen concentration and Figure 1.8 shows the response time as a function of hydrogen concentration. Figure 1.7 shows that a response was first seen around 1% when phase transition of the palladium occurred. A saturating response, similar to the semiconducting sensors, was observed for hydrogen concentrations greater than 10%.

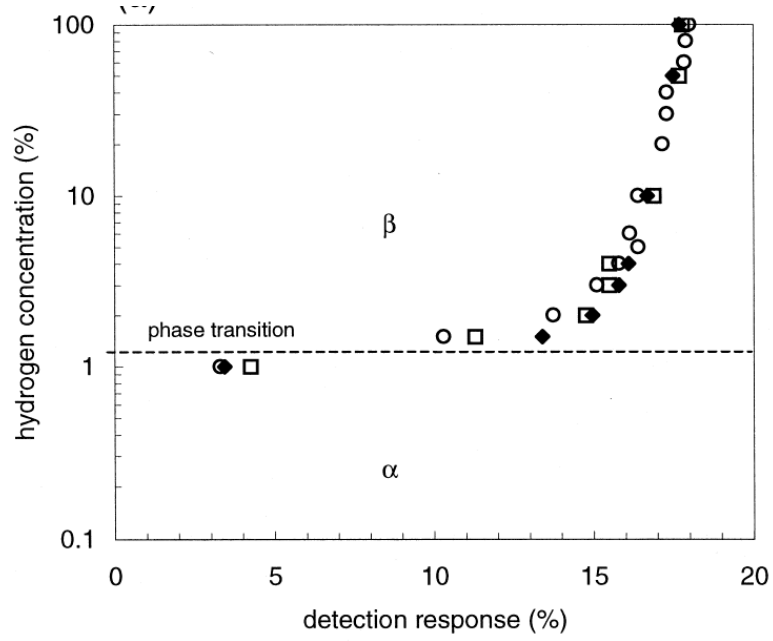


Figure 1.7 Detection response of a palladium micromirror as a function of hydrogen concentration. Source: Bevenot 2000.

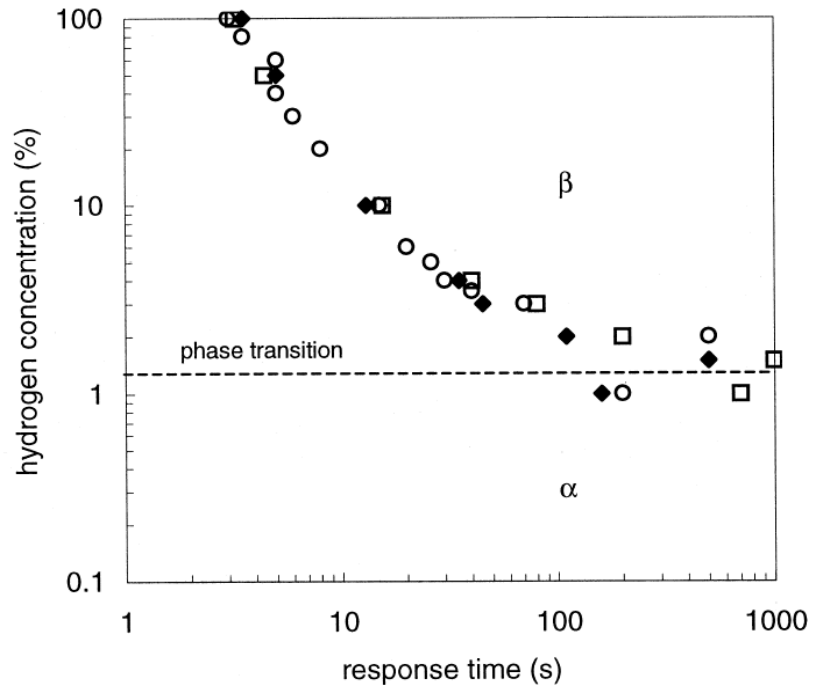


Figure 1.8 Response time of a palladium micromirror as a function of hydrogen concentration. Source: Bevenot 2000

Response times were observed to exponentially increase as hydrogen concentration decreased exhibiting a 14 second response at 4% by volume. In addition, maximum response was seen at low temperatures while low response was seen at high temperatures whereas response times were longer at low temperatures and shorter at high temperatures.

Surface plasmon resonance sensors also examine the change in optical properties of palladium in the presence of hydrogen. Tobiska et al. presents a surface plasmon resonance sensor in which an optical fiber is embedded in a palladium substrate. A diode laser is used to illuminate the fiber and a detector with a collimating lens and polarizer is used to monitor changes in the transmitted light through the fiber. In the presence of varying concentrations of hydrogen, adsorption into the palladium causes a change in its complex permittivity. As a result, the transmission of transverse magnetic (TM) polarized light increases and the transmission of transverse electric (TE) polarized light decreases. This plasmon sensor was examined only at the lower explosive limit of hydrogen, 4% by volume. A TM polarization response of 51% and TE polarization response of -5% were seen upon introduction of the hydrogen sample. Response time was observed to grow from 74 seconds to 150 seconds over sensor cycling and recovery time grew from 540 seconds to 680 seconds. A full day was required to achieve complete desorption of hydrogen from the sensor and a return to original signal levels. The resolution of the sensor was estimated at 0.2% by volume of hydrogen in nitrogen. It should be noted that the author also observed poisoning and unpredictable changes in response time if the sensor was not kept under a pure gas flow.

The final class of chemisorbant hydrogen sensors are the surface acoustic wave (SAW) sensors. These sensors involve the incorporation of the active layer onto a solid

piezoelectric substrate. Application of current at a specific frequency generates a surface acoustic wave under the palladium layer that experiences shifts in frequency based on hydrogen adsorption in the layer (Jakubik et al. 2002). D'Amico et al. developed the first SAW sensors using thin palladium layers and achieved a small response even at three percent hydrogen by volume (D'Amico 1989). Recently, bilayer films of palladium and other metalloceramics, namely nickel phthalocyanine and copper phthalocyanine, have been proposed by Jakubik et al. Hydrogen detection was observed over a concentration range of 0.5 to 3% hydrogen by volume in nitrogen. Response times of 100 seconds for 0.5% and 1000 seconds for 1.5% were exhibited with recovery times around 200 seconds. Sensitivity was shown to have an inverse relationship with temperature.

While all forms of the solid-state sensors presented here provide a compact, functional hydrogen detection scheme for low hydrogen concentrations around or below the lower flammability limit of 4% hydrogen by volume, several drawbacks are noted from the examples presented. For the detection of hydrogen, solid-state sensors must first adsorb the gas until equilibrium is achieved on the solid surface which results in a delayed response time for the detection of hydrogen thereby reducing the ability for rapid detection (Dong 2003). Response times of all the above sensors were at least 10 seconds with many achieving a steady signal after a period of minutes. Due to adsorption, a recovery time is needed for the diffusion of hydrogen from the active film layers before successive sensing can occur. This time period is much greater than the response time in all cases resulting in limited repeatability of measurements in a short time period. In addition, the reactive surface is also prone to "poisoning" due to its chemisorbent property. Other chemical species can adsorb onto the surface which not only hinders

hydrogen absorption, but also changes the physical properties of the material. This affects the accuracy of the sensor for hydrogen detection. Finally, saturation tendency results in reduced signal sensitivity at increased concentrations thus making broad detection ranges difficult to achieve for most sensors (Dong 2003).

1.3.2 Acoustic Hydrogen Sensors

As discussed previously, acoustic hydrogen sensors take advantage of differences in the densities and speeds of sound between hydrogen and other gases, particularly air, to achieve detection. Often these two properties are combined into a single parameter, the acoustic impedance, which is the product of the speed of sound and the density for a gas. Due to the dependence on both properties, the acoustic impedance shows even greater variation between hydrogen and other gases. Hydrogen has an acoustic impedance that is approximately a quarter of the impedance for air, a mass density 1/15 of air, and a speed of sound four times that of air. The lower molecular weight of hydrogen also results in a much greater acoustic velocity for hydrogen in comparison to most gases except for helium (Dong 2003). Two acoustic hydrogen sensors are now presented to examine the detection limits, response times, detection range and sensitivity of acoustic hydrogen sensors.

Dong et al. developed an acoustic hydrogen sensor entitled a piezoelectric-sound-resonance cavity (PSRC). This sensor is constructed of two piezoelectric discs placed at opposite ends of a cylindrical cavity. A hole in one of the piezoelectric discs allows sample gas to enter and exit the chamber. An AC voltage is applied across on disc causing a bending motion which upon release, generates a resonant standing wave in the cavity. The other disc is used to record the changes in the frequency and acoustic intensity of the standing wave by monitoring the voltage and phase output of the disc.

Through experimentation it was shown that the output voltage and phase responded linearly to a change in hydrogen concentration with a limit of sensitivity below 10 ppm. Some concern is associated with this measurement because a calibrated electrochemical reaction was used to generate low hydrogen concentrations. The calibration of the electrochemical reaction was achieved using a semiconductive hydrogen sensor. As already noted, semiconductive hydrogen sensors suffer from delayed response time thus introducing error into the calibration of gas production and consequently into the calibration of the PSRC. With this noted, the PSRC exhibited a linear response up to a concentration of 0.2 ppm and a response time of 1.2 sec to changes in concentration.

A second acoustic sensor has been presented by Barberi et. al. in which an acoustic wave is generated by a sensitizer, a black body that produces an acoustic wave in response to excitation by narrow pulse radiation. The acoustic wave is independent of wavelength thus allowing for the use of any narrow pulsed radiation source. A small diode laser was used for testing of this system. After the wave is generated, its propagation time through a gas is examined with an acoustic detector in the same fashion as for the PSRC acoustic sensor. Again, a linear response of the shift in propagation time was observed with increasing hydrogen concentration up to around 0.25% by weight. Sensitivity was found to be approximately 200 ppm. The author did not comment on response time.

The two acoustic hydrogen sensors discussed here have shown low detection limits and reduced response times are obtainable with acoustic hydrogen sensors in comparison to solid-state detection schemes. While showing these improvements, it must be noted that acoustic properties of gases are temperature dependent thus application as a

hydrogen monitoring device would require a controlled sampling environment. In addition, these acoustic hydrogen sensors still require localized hydrogen sampling without the possibility of remote sampling and in the case of the PSRC acoustic sensor, are constructed of piezoelectric materials which can have significant cost implications for use in large numbers.

1.3.3 Mass Spectrometry-based Hydrogen Detection Schemes

Mass spectrometric methods are currently being employed for the purpose of hydrogen leak detection in the U.S. space program. Mass spectrometry is a common technique employed in the laboratory to determine molecular composition. This method of analysis should not be confused with spectroscopy in which radiation absorption or emission is used to determine composition. Mass spectrometry uses a beam of highly energetic electrons to separate molecules into charged components and then measures the masses of these fragments through manipulation in a magnetic field (Wade 2003). The data obtained from this process allows for a reconstruction of the analyte's constituent molecules and a determination of concentration of the analyte.

Mass spectrometry is one of the primary technologies currently in use for hydrogen leak detection for the U.S. space shuttle program. In the past, NASA has used multiple systems to monitor for hydrogen leaks prior to launch. The Prime Hazardous Gas Detection System (HSDS) and Backup HSDS were the primary systems, incorporating a linear quadropole and fixed sector mass spectrometer, respectively, for detection (Griffin 2002). The Hydrogen Umbilical Mass Spectrometer (HUMS) and Portable Aft Mass Spectrometer (PAMS) were two more systems developed to detect hydrogen leaks in a helium background (Naylor et al.). These systems were all limited by delays greater than 20 seconds and transport lines greater than 200 feet. Griffin et al. developed a new

HSDS 2000 system which combines the functions of all previous systems and can be positioned on the mobile launch platform. The system again uses a series of pumps and transport lines to draw samples from locations around the shuttle and launch pad to two quadrupole mass spectrometers. Tests of the systems were performed using mixtures of hydrogen, helium, oxygen and argon in a nitrogen balance at concentrations of 0, 500, and 5000 ppm. Calibration curves were not provided by Griffin but it was stated that detection limits of less than 25 ppm were achieved. Ottens et al. examined the same detection setup in a laboratory at the same concentrations. A limit of detection of 12 ppm was found with a response time of 8 seconds and a recovery time 6 seconds. The results were repeatable with a precision of 2.0%. Griffin et al. noted a drift in the hydrogen measurements attributed to water infiltration into the system.

1.3.4 Optical Spectroscopic Hydrogen Detection Schemes

This category encompasses hydrogen sensing technologies in which a characteristic emission spectrum of electromagnetic radiation is used for hydrogen identification after excitation. The methods examined in this paper, namely time-resolved Raman scattering and Laser-Induced Breakdown Spectroscopy (LIBS) fall into this category. In addition to being the focus of this paper, Raman spectroscopy has been the technique on which previous optical spectroscopic detection schemes have been developed. For this reason, any existing detection schemes using these technologies are presented in the following chapter after an introduction to each form of spectroscopy has been provided.

All four classes of hydrogen sensing technologies presented have demonstrated the ability to detect hydrogen gas in a background atmosphere. While effective in detection, all exhibit limitations in one or more of the following areas: detection limits, detection range, response time, sensitivity, and durability.

1.4 Research Motivation and Breadth

New hydrogen detection and monitoring schemes are needed for the expanding hydrogen public and commercial infrastructure as well as for continued aerospace application. These detection schemes must ensure safety by providing low limits of detection, a broad detection range, high sensitivity, and almost instantaneous response times in a compact, robust, and functional format. The focus of this work is to examine two optical spectroscopic techniques for use in hydrogen leak detection schemes and their ability to satisfy the aforementioned criteria. The spectroscopic techniques considered are time-resolved Raman scattering and Laser-Induced Breakdown Spectroscopy (LIBS). Time-resolved Raman scattering is a technique in which characteristic spectral emission is monitored after excitation of an analyte to identify the component species. LIBS is a technique in which the spectral emission from an laser-induced plasma and the associated ionization of an analyte is examined to identify component species. While a more detailed description of the fundamental processes involved with each technique is presented in the following chapter, the these two techniques lend themselves to low concentration species detection, a broad detection range, high sensitivity, real-time feedback and implementation in a simple, rugged format thereby providing the motivation for this research. In addition, Raman scattering is well-suited for remote detection and LIBS is a promising point source sensing technology. The specific goals of this research are:

1. Demonstrate the ability to detect hydrogen using both time-resolved laser-initiated Raman scattering and time-resolved Laser-Induced Breakdown Spectroscopy.

2. Investigate the effects of excitation wavelength and optical configuration on the detection of hydrogen by Raman scattering.
3. Compare and contrast the use of a gaseous breakdown versus a substrate-initiated breakdown for LIBS hydrogen detection.
4. Determine experimental limits of detection and sensitivity for hydrogen detection using both approaches.
5. Investigate the effect of substrate degradation on detection limits for LIBS hydrogen detection.
6. Implement and perform initial testing of a portable field detection apparatus using both detection methodologies.

The following documentation provides an introduction to each analytical technique and presents a discussion of all results pertaining to the outlined research goals.

CHAPTER 2 FUNDAMENTAL SCIENCE AND BACKGROUND

This chapter presents a description of the physical processes characteristic to spontaneous Raman spectroscopy and Laser Induced Breakdown Spectroscopy (LIBS). In addition, application of each spectroscopic technique to hydrogen detection is discussed along with any current hydrogen detection schemes using each technique and the associated limitations of those technologies.

2.1 Raman Spectroscopy

Electromagnetic radiation can interact with molecules in many ways. The effects of this interaction are varied based upon the energy content of the electromagnetic wave and the nature of the heterogeneity. Radiation can either be scattered, absorbed or emitted. Spontaneous Raman spectroscopy is a form of molecular spectroscopy that probes vibrational level transitions occurring in response to interaction with electromagnetic radiation for species identification. A fundamental look at spontaneous Raman scattering is now presented along with a specific examination of Raman for hydrogen gas and current Raman detection schemes for hydrogen leak detection.

2.1.1 Spontaneous Raman Scattering

When electromagnetic radiation impinges on molecules, the associated electric field of the radiation induces an oscillating dipole moment in the molecule by displacing electron density at the frequency of the incident wave. A visual representation is shown in Figure 2.1 using an electrostatic potential map of an arbitrary, symmetric diatomic molecule.

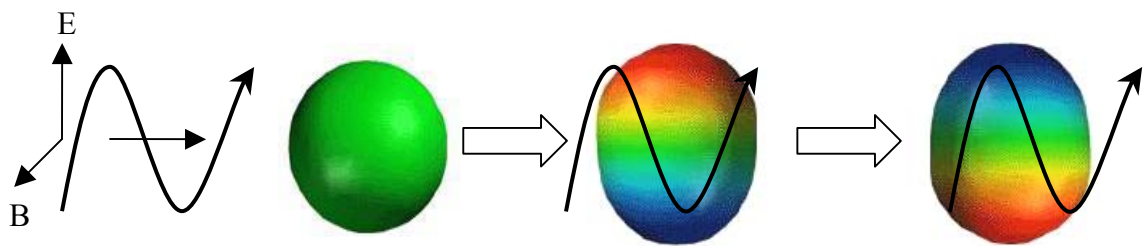


Figure 2.1 Electrostatic potential maps showing the induction of an oscillating dipole in a symmetric diatomic molecule due to incident electromagnetic radiation. Charge density, initially uniform, is displaced upon interaction with the oscillating electric field of the incident radiation.

The interaction of a molecule with electromagnetic radiation can be examined using a classical wave model or a quantum mechanical viewpoint. Approaching from a quantum mechanical viewpoint, the energy of an incident photon of radiation is $h\nu_{inc}$ where h is Planck's constant and ν_{inc} is the frequency of the incident radiation. As stated previously, the induced dipole moment oscillates at the incident frequency of ν_{inc} ($\nu=c/\lambda$). If the molecule has no permanent dipole moment, this oscillation can induce a dipole moment. The energy coupled into the oscillation of the induced dipole moment can result in vibratory quantum transitions in the molecule.

Initially, the ground state vibrational level is the most highly populated with only a small proportion of electrons occupying higher vibration states at room temperature. This distribution is governed by the Boltzmann Distribution which is given in Equation 2.1 where n_i is the number of atoms per volume in an energy state, n_t is the total number of atoms per volume, g_i is the statistical weight of the energy state, E_i is the excitation energy to achieve state i , k is Boltzmann's constant, T is absolute temperature, and $Z(T)$ is the partition function given by Equation 2.2.

$$n_i = \frac{n_t g_i e^{-E_i/kT}}{Z(T)} \quad \text{Equation 2.1}$$

$$Z(T) = \sum_{i=0}^{\infty} g_i e^{-E_i/kT} \quad \text{Equation 2.2}$$

Upon excitation through induced dipole oscillation, electrons from the lower vibrational state are excited to a higher vibrational level. If the excitation energy exactly matches the difference in energy between two quantum levels, the energy is absorbed into the molecule. This process is used in infrared absorption spectroscopy (IR) and will not be examined in this work. If the energy increase does not match a specific electronic transition, electrons are promoted to a virtual vibrational or vibrational-rotational state. This virtual energy level is unstable and a subsequent release of energy occurs in the form of a photon in a process known as scattering. In general, scattering cannot be separated into two distinct events as with absorption and emission. Scattering occurs in less than 10^{-14} seconds (Nafie 2001) and is classified as either elastic or inelastic. Elastic scattering occurs when the emitted or scattered photon contains the same quanta of energy as the incident exciting photon. Inelastic scattering occurs when a portion of the imparted energy from the incident photon is retained by the molecule, thus the scattered photon exhibits a shift in frequency from the incident photon. If the retained energy is linked to a vibrational or vibrational-rotational mode of the molecule, the inelastic scattering is entitled Raman scattering. The magnitude of the shift in frequency of the scattered light is unique for a molecule and a given vibrational state and is constant and independent of the excitation source frequency (Baranska 1987). If the shift occurs to a lower photon frequency, thus lower energy, it is entitled a Stokes shift and the corresponding emission band, a Stokes band. Stokes shifts occur when the final vibrational state of the molecule is greater than the initial vibrational state, hence energy is added to the molecule. A shift to a higher photon frequency, thus higher energy, is referred to as an Anti-Stokes shift generating an Anti-Stokes band, hence energy is added

to the photon. These shifts are presented in Equation 2.3 and Equation 2.4 in terms of photon energy.

$$h\nu_{Stokes} = h\nu_{incident} - h\nu_{vibration} \quad \text{Equation 2.3}$$

$$h\nu_{Anti-Stokes} = h\nu_{incident} + h\nu_{vibration} \quad \text{Equation 2.4}$$

Anti-Stokes shifts can occur because the relaxation of the molecule during the scattering interaction allows the molecule to return to a lower vibrational energy state than the molecule was at prior to excitation, thereby passing the vibrational quanta to the now inelastically scattered photon. Figure 2.2 shows an energy level diagram to illustrate differences between elastic and inelastic Raman scattering.

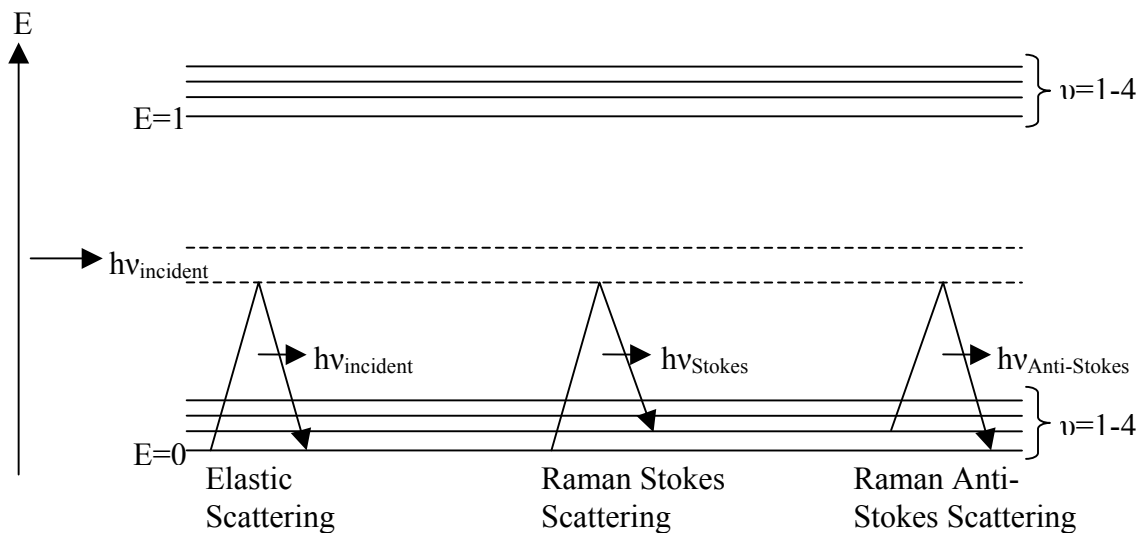


Figure 2.2 Energy level diagram showing a comparison of elastic scattering transitions with inelastic Raman scattering transitions.

As shown in Figure 2.2, the shift in frequency corresponds to a specific vibrational level (Ingle and Crouch 1998). Raman scattering can also take place between virtual vibrational levels when the incident photon exceeds an electronic transition energy. This process is known as Resonance Raman Scattering and will not be examined in this text. The Raman shift observed in the frequency of the scattered photon is usually quantified

by wave number. The relation between frequency, ν , wavelength, λ , energy, E , the speed of light, c , and wave number, $\bar{\nu}$, is given by Equation 2.5,

$$\bar{\nu} = \frac{\nu}{c} = \frac{1}{\lambda} = \frac{E}{hc} \quad \text{Equation 2.5}$$

Wave number is usually expressed in dimensions of cm^{-1} . Since the shift in frequency of the scattered photons is species dependent, Raman scattering can be used for species identification. Collection and dispersion of the scattered radiation produces a scattering spectrum which can be examined for characteristic Raman bands and their intensities to identify species and concentrations present in the analyte. This method of molecular spectroscopy is therefore entitled spontaneous Raman spectroscopy.

As stated previously, at lower temperatures such as room temperature, the ground vibrational state is the most highly populated with electrons as dictated by Boltzmann's Distribution. For this reason, Stokes shifts occur more frequently under standard conditions thus producing more intense scattered radiation. The Anti-Stokes Raman band intensities are enhanced at elevated temperatures. Figure 2.2 shows the qualitative relationship between Rayleigh scattered lines and Raman scattered lines in a scattering spectrum at room temperature. While intensities are arbitrary, they are meant to display a relationship among the lines. Typically, Rayleigh scattering intensities are many orders of magnitude greater than Raman intensities, as discussed below.

Raman scattering occurs as a result of transitions between vibrational and/or rotational energy levels of molecules, therefore it cannot be used for atomic identification. In addition, for an analyte to be Raman active, certain conditions regarding the interaction of the molecule with incident electromagnetic radiation must be met.

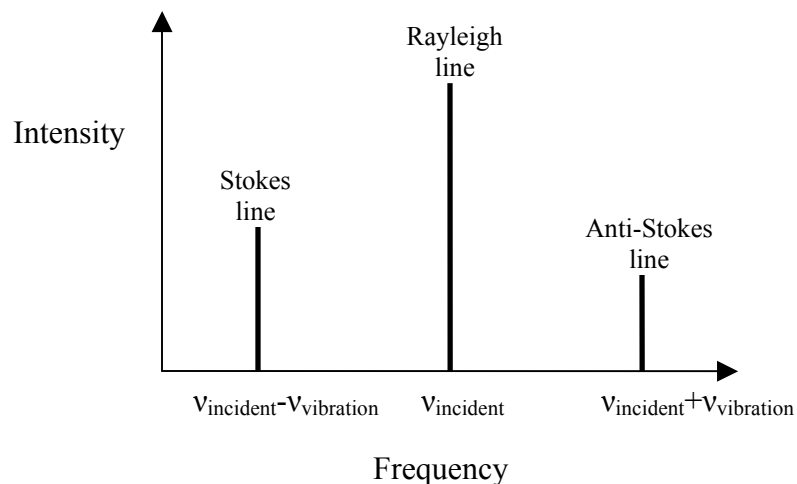


Figure 2.2 Arbitrary Raman spectrum exhibiting the frequency and intensity relationship between elastically scattered and inelastically scattered radiation. Source: Ingle and Crouch 1998.

The induced dipole moment, μ , is proportional to the intensity of the electric field associated with the incident photon as shown in Equation 2.6.

$$\bar{\mu} = \alpha_{ij} \bar{E} \quad \text{Equation 2.6}$$

The tensor, α_{ij} , is known as the polarizability and is species dependent. As shown Equation, 2.6, the induced dipole moment is a vector thus it can have different magnitudes in each coordinate direction in a molecule. The polarizability is a symmetric tensor ($i=3, j=3$) whose nine values determine the motile behavior of electrons in space in response to imposed electric fields. Equation 2.7 shows the components of the polarizability for an orthogonal coordinate system (x,y,z).

$$\alpha_{ij} = \begin{bmatrix} \alpha_{xx} & \alpha_{xy} & \alpha_{xz} \\ \alpha_{yx} & \alpha_{yy} & \alpha_{yz} \\ \alpha_{zx} & \alpha_{zy} & \alpha_{zz} \end{bmatrix} \quad \text{Equation 2.7}$$

The polarizability matrix is always non-zero and is a function of molecular size and shape with units of volume (Baranska 1987). The polarizability is usually anisotropic and smaller for single bonded molecules than molecules with higher bond orders although

isotropic molecules do exist. For a molecule to be Raman active, the induced oscillation in response to incident electromagnetic radiation must result in a *change* in the polarizability of the molecule. This criterion is mathematically given by Equation 2.8 where Q is the normal component of vibration at the point of zero displacement.

$$\alpha'_{ij} = \left(\frac{\partial \alpha_{ij}}{\partial Q} \right)_0 \neq 0 \quad \text{Equation 2.8}$$

Graphically, this criteria is defined as a non-zero slope on the plot of polarizability magnitude as a function of vibratory displacement at the location of zero displacement. In addition, for symmetric molecules there exists a rule of mutual exclusion with IR absorption activity. The rule states that if a center of symmetry exists in a molecule, an induced oscillation that is Raman active cannot be IR active and vice versa. For reference, a permanent dipole moment and a change in the permanent dipole moment of a molecule at zero displacement in response to an induced oscillation, as stated in Equation 2.9, are required for IR activity.

$$\bar{\mu}' = \left(\frac{\partial \bar{\mu}}{\partial Q} \right)_0 \neq 0 \quad \text{Equation 2.9}$$

If the polarizability criterion and mutual exclusion principle are satisfied, spontaneous Raman scattering can occur. The specific Raman activity of hydrogen gas will be discussed in the following section.

The intensity of Raman scattered radiation is much lower than that of elastically scattered light. Elastically scattered light is usually 10^3 - 10^4 times greater in intensity as compared to Raman bands (Baranska1987). As shown in Equation 2.10, Raman intensity is dependent on many factors namely the differential scattering cross section σ' , the source irradiance E_0 , the number of gas molecules present N, the temperature T, the

vibrational partition function Q_v , and the vibrational degeneracy $g_{v,i}$, and energy level $E_{v,i}$, of a molecule in the initial vibrational state v^i . In addition, Equation 2.11 shows the differential scattering cross section is proportional to the fourth power of the excitation frequency ν_{inc} (Long 2002).

$$I_R = \sigma' E_0 N g_{v^i} \frac{\exp(-E_{v^i} / kT)}{Q_v} \quad \text{Equation 2.10}$$

$$\sigma' \propto \nu_{inc}^4 \quad \text{Equation 2.11}$$

Two important components of the given equations are the fourth power dependence of the scattering cross section on incident frequency and the intensity dependence on number density of molecules at a specific energy state. Significant gains in Raman scattering intensity can thus be gained by an increase in the excitation frequency (reduction in wavelength). The dependence of the intensity on number density is what allows Raman spectroscopy to be used as a quantitative technique in addition to its use as a structural probe. Therefore, higher concentrations of scatterers in the excited volume will yield larger scattering intensities. The other dependencies of intensity also must be considered. Raman spectroscopy requires a light source with sufficient irradiance, E_0 , to produce detectable signal intensity at the shifted frequency of Raman band. In addition, a monochromatic light source is desirable to produce a single wavelength Raman band. Lasers are thus ideal excitation sources for Raman scattering (Baranska 1987). In addition, the Raman scattering cross-section is dependent on the frequency of the incident radiation. Higher frequencies, or higher photon energies, increase the Raman cross-section thus increasing scattering intensities. Finally, there is angular dependence for Raman scattering on the incident radiation polarization. The scattering cross section has

angular dependence for horizontally polarized incident radiation. Also, based on molecular structure, depolarization of the scattered radiation can occur. The depolarization ratio, ρ , relates the radiant power of perpendicularly polarized scattered radiation to the radiant power of the parallel polarized scattered radiation with respect to the incident radiation polarization as shown in Equation 2.12.

$$\rho = \frac{(\Phi_R)_{perpendicular}}{(\Phi_R)_{parallel}} \quad \text{Equation 2.12}$$

With this noted, the scattering cross section has no dependence on vertically polarized excitation radiation and there is no depolarization associated with symmetric, diatomic molecules such as hydrogen. As discussed in Chapter 3, a vertically polarized source was used to avoid any angular dependence for the scattered radiation. In addition, the radiant power was collected over all scattered polarizations at the angle of interest, therefore, no further comment will be made on polarization. The reader is referred to text for further information on polarization effects. (Lewis and Edwards pp3-10). Finally, Equation 2.10 shows the dependence of scattering power on temperature. As temperature increases, so does the scattered intensity therefore temperature must be taken into account when spontaneous Raman scattering is used as a quantitative technique.

In this body of work, spontaneous Raman spectroscopy is time-resolved in addition to being spectrally-resolved. Knowledge of excitation source timing, i.e. laser q-switch timing, coupled with known optical path lengths allows investigation of Raman bands in specific time regimes. This method aids in signal discrimination and noise mitigation.

2.1.2 Raman Scattering of Hydrogen Gas

Hydrogen gas is composed of diatomic, symmetric, linear molecules with no permanent dipole moment due to the balance of electronegativity between the two

identical component atoms. Therefore, hydrogen cannot be IR active since it does not have a permanent dipole moment. For Raman activity, as previously discussed, the analyte must exhibit a change in polarizability in response to vibratory oscillation. As the normally symmetric electron density of hydrogen is shifted during vibration, an incident electronic field of the excitation radiation will induce a constantly varying dipole moment in the hydrogen molecule. The varying dipole in turn influences the ability of the hydrogen molecule to change polarization in response to other external forces, therefore changing the polarizability of the molecule. With the requirement for spontaneous Raman scattering satisfied, hydrogen will emit Stokes and anti-Stokes radiation which can be detected and quantified. Practical detection requires scattering intensities high enough to achieve detection beyond the level of background noise, which can be difficult because of the magnitude difference between the inelastic and elastically scattered radiation, although the wavelength shift helps to overcome this issue. As stated before, radiant power of the Raman scattered radiation is a function of excitation photon energy, therefore higher frequency photons are preferred for excitation. Table 2.1 gives differential Raman scattering cross-sections for the Q-branch vibrational transitions in hydrogen and four other species at the two experimental excitation intensities used in this study, as well as the Raman shift for the Q-branch for all species. The presented scattering cross sections in Table 2.1 show that hydrogen not only scatters light inelastically at greater amounts than other similar species, but more importantly that at 355 nm the differential scattering cross section is about seven times greater than the cross section at 532 nm.

Table 2.1 Raman shifts and absolute differential scattering cross-sections for Q-branch vibrational bands at two excitation wavelengths.

Molecule	Raman Shift (cm ⁻¹)	Differential Absolute Scattering Cross Section by Excitation wavelength (cm ² /sr)	
		355 nm	532 nm
Hydrogen, H ₂	4156	9.66E-30	1.43E-30
Nitrogen, N ₂	2331	2.31E-30	3.97E-31
Oxygen, O ₂	1555	2.31E-30	3.91E-31
Carbon monoxide, CO	2143	2.08E-30	3.63E-31
Carbon dioxide, CO ₂	1285	1.62E-30	1.62E-30
	1388	2.31E-30	4.71E-31

Source: Schrotter and Klockner pp137-138

This is expected from the theory presented in the earlier section and is a driving factor for using lower wavelength excitation sources. Another concern for detection and quantification of the spontaneous Raman scattering signal is the ability to spectrally resolve the signal from the much more intense elastically scattered light. As Table 2.1 shows, the Raman shift for hydrogen gas is significantly larger in wave number than for other species, at the incident wavelengths of 355 nm and 532 nm, the scattered radiation signal translates to approximately a 60 nm or 150 nm shift, respectively, from the elastically scattered light at the incident wavelength. In contrast to the absorption cross section, spectral discrimination is thus improved at higher wavelengths. Regardless, the line is still close to the Rayleigh scattered radiation at the incident frequency, therefore filtering during experimentation is necessary to avoid stray elastically scattered light from being detected.

Raman scattering is examined in this body of work as a practical hydrogen detection scheme for two reasons. The first and most important reason is the ability to provide remote detection. Using a compact laser system, hydrogen detection could be performed in field environments where the investigator may be separated from the area of

inspection. All that is required with this technique, specifically backscatter Raman spectroscopy, is a linear path to the area of inspection. One exception is that due to the flammability limits of hydrogen, care must be taken in any practical application to avoid generating combustion on surrounding surfaces as such an interaction would possibly initiate hydrogen combustion. A second benefit of Raman scattering is that it could provide a real-time detection technique. This is important not only for continuous monitoring applications but also due to the hazards of leaking hydrogen gas. For these benefits to be realized, low detection limits and high sensitivity must first be documented.

2.1.3 Existing Hydrogen Leak Detection Schemes using Raman Scattering

Spontaneous Raman scattering has long been a common laboratory technique for species identification and quantification. The development of the laser with its ability to provide a high intensity, monochromatic light source was an important advance in Raman spectroscopy. The laser yields photon energies much greater than those of previous continuum light sources thereby greatly increasing the intensity of Raman bands.

Although lasers helped make significant advances in laboratory Raman spectroscopy, the use of spontaneous Raman scattering for practical chemical monitoring in the field is still limited due to band intensities at practical sampling distances. A few spontaneous Raman-based systems have been developed for use as gaseous hydrogen detectors in the field environment. The following documentation describes these detection schemes and as with the presentation of previous detectors, examines the metrics and limitations of each system.

De Groot developed a hydrogen leak detection system for NASA to detect hydrogen gas leaks during shuttle operations. The system developed consisted of delivery and collection optics coupled into an optical probe head. A fiber optic line was

used to transfer the excitation source radiation, a continuous wave (cw) 514.5 nm Argon Ion laser beam chopped with an optical chopper at 300 to 500 Hz, radiation to the optical head and a second fiber optic line was used to return the collected scattered radiation to laboratory instrumentation. The incident laser beam was turned by a 45° dichroic mirror followed by a focusing lens to focus the radiation on a sample volume. Scattered light from the gaseous sample volume was collimated onto the mirror by the same lens used to focus the laser beam and then turned by another 45° mirror and focused by a lens into a collection fiber. The author chose a 180° backscatter orientation based on preliminary scattering intensity calculations which exhibited an advantage in spatial resolution over a 90° orientation. The instrumentation used to process the scattered radiation consisted of a Raman notch filter at the incident laser frequency, a spectrometer coupled to a photomultiplier tube (PMT), a lock-in amplifier and a signal readout. The Q-branch line used for hydrogen detection was located at 654.6 nm and a 2.12 % hydrogen mixture in air was used for system evaluation. While the author was able to detect nitrogen Raman bands with this configuration, hydrogen Raman bands were almost undetectable with only a slight, non-quantifiable increase in intensity at the Raman band location comparable to the background noise level. The small signal also fluctuated above and below the noise level. De Groot cited possible laser mode hopping and noise caused by scattered radiation as reasons for undetectable hydrogen line intensities. He suggested using a PMT with higher quantum efficiency, a pierced mirror to reduce incident laser scattering, larger diameter collection optics and fiber optics, and the use of a laser with higher photon energy.

Alder-Golden et. al also developed a spontaneous Raman sensing system for trace hydrogen gas detection. This system was designed specifically for the Mobile Launch Platform for the space shuttle. A cw 488.0 nm Argon Ion laser and a He-Ne laser source were tested in combination with a chopper wheel as excitation sources. The incident laser beam was directed by dielectric mirrors through a focal lens into a multi-pass sample chamber with a Herriott-type configuration. A gaseous sample was injected with a flow injector into the sample chamber and the incident laser beam was passed through the sample 30 times. The resulting scattered light was collected by lenses coupled with a bandpass filter centered at the corresponding Q-branch at 612 nm and focused onto a PMT. The PMT signal was processed using a lock in amplifier to separate out the Raman scattering signal from ambient background light. Gas mixtures containing hydrogen concentrations from 400 ppm to 100% hydrogen were used for device characterization. The scattering signal was found to be directly proportional to the hydrogen concentration for both laser sources as shown in Figure 2.3. A more sensitive version of the Ar-Ion system was developed for field testing and a detection limit below 100 ppm was quoted at atmospheric pressure. The He-Ne was not tested in a field configuration but predicated detection limits were given as 60 ppm. As shown in Figure 2.3, the Ar-Ion laser configuration with its higher energy achieved a greater sensitivity than the He-Ne laser. All observed noise was attributed to stray scattered light, and dark noise, and noise from electrical instrumentation, with the exception of the increase in noise seen at higher concentrations as shown in Figure 2.3. This noise was attributed primarily to shot noise from the Raman signal.

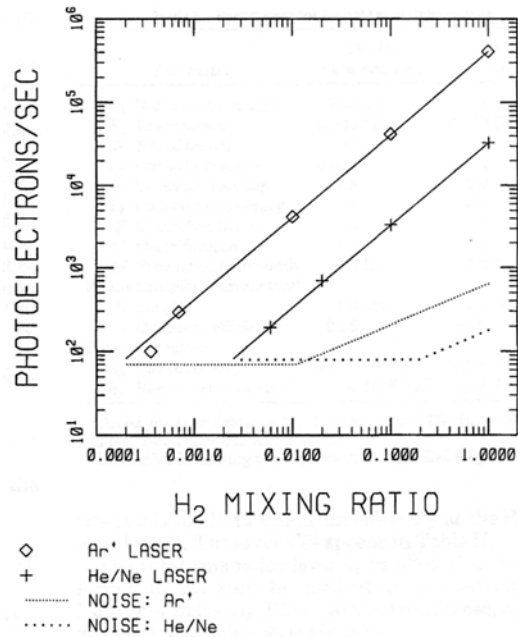


Figure 2.3 Signal as a function of hydrogen concentration for the Alder-Golden et al. hydrogen leak detection system. Dotted curves represent RMS noise levels.

Many other investigations of Raman scattering in hydrogen gas have been performed in a laboratory setting using not only spontaneous Raman spectroscopy with the Stokes and Anti-Stokes, but also using stimulated Raman spectroscopy, coherent anti-Stokes Raman spectroscopy (CARS), thermal lens Raman spectroscopy (TLRS), and resonance Raman scattering. For further information on these investigations of hydrogen gas, the reader is referred to literature (Oki et al. 2000, Seliskar et al. 1983, Vasa et al. 2002, Papayannis et al. 1998, Morozov et al. 1998, Meng et al. 2000, Lallemand et al. 1966, Huo et al. 1992, Ghosh et al. 1997, Lallemand and Simova 1968, Wang et al. 1998, Oksengorn 1993, Krylov et al. 1996, Villeneuve et al. 1998, Hancock et al. 1997, Barrett 1976, Audivert and Lukasik 1977, Bloembergen et al. 1967, Duardo et al. 1968, Wilkerson et al. 1991, O'hira and Okuno 1996, Yagi and Huo 1996). To the author's knowledge, the detection systems presented by de Groot and Alder-Golden et al. are the

only practical hydrogen gas detection and quantification schemes using spontaneous Raman scattering.

Spontaneous Raman scattering provides an effective detection tool as shown by the detection limits and sensitivities of the two given systems. While the systems were more effective in these aspects of detection than most of the schemes presented in Chapter 1, further development of a Raman detection system is needed. The de Groot system, while easily implemented except for the need for close proximity to the sampling volume, was unable to achieve significant scattering intensities. With the Alder-Golden et al. system, detection using Stokes scattering with a low detection limit was achieved but the system again required close proximity to the sampling volume and used complex sampling delivery and optics configurations. With improvements such as a simplified configuration based on remote detection, increased laser photon energy, and time-resolved fast response detection, Raman is believed to be a sensitive analytical technique for hydrogen leak detection.

2.2 Laser-Induced Breakdown Spectroscopy

Laser-Induced Breakdown Spectroscopy is a form of atomic emission spectroscopy. In LIBS, a high intensity source of irradiance is used to overcome the dielectric threshold of sample gas, liquid or solid volume thereby inducing ionization of the analyte's constituent molecules and atoms. This ionization produces a plasma consisting of a conglomeration of all ionized molecules and a cloud of free electrons. After the source of irradiance is removed, free electrons and ions recombine to form atoms and molecules, losing energy in the process. The excess electronic energy is given off in the form of photons which can be collected to generate an emission

spectrum. Using known emission lines for atomic species, quantitative detection of analyte species can be achieved.

2.2.1 Plasma Generation and Emission

The first step of LIBS is a generation of a plasma in the analyte sample volume. For plasma formation, an initial seed electron with sufficient energy to initiate ionization is required. For sources with short wavelengths or high irradiances, this electron can be provided by multiphoton ionization (MPI) of molecules in the sample volume. Multiphoton ionization occurs when sufficient photons are absorbed by a single molecule or atom to induce ionization (Radziemski and Cramers 1989). With longer wavelengths or lower irradiances, plasma formation is initiated by either the interaction of molecules in the sample volume with a cosmic ray, or thermionic emission after sufficient heating by the source of irradiance (Radziemski and Cramers 1989). Once a seed electron of sufficient energy is present, two mechanisms are responsible for growth and further electron generation in the plasma. The first is the absorption of photon energy from the irradiance source by an electron upon collision with a neutral species. When electrons gain sufficient energy through absorption, they can collide with a neutral molecule and ionize the molecule. This produces a second unbound electron while retaining sufficient energy to exceed ionization levels and therefore remaining unbound as illustrated by Equation 2.13 where e^- symbolizes an electron and M symbolizes a molecule.



The production of two electrons from one will lead to cascade ionization through which electron concentration will increase exponentially with time provided the incident irradiation source continues (Radziemski and Cramers 1987). The second mechanism for

plasma growth is MPI which was described above and can be represented by Equation 2.14.



A minimum number of photons, m , is required for multiphoton ionization to occur as given by Equation 2.15 where ε_I is the ionization potential.

$$m > \left\lceil \frac{\varepsilon_I}{h\nu} + 1 \right\rceil \quad \text{Equation 2.15}$$

As discussed previously, MPI is only significant at energetic wavelengths, usually much less than 1 μm , therefore its importance is highly dependent on experimental configuration and is often more relevant to pure gas breakdown. A third mechanism for growth of plasmas initiated on solids is thermal runaway. In this process, shock waves produced in the air as a result of vaporization of the solid are coupled with radiative heating through photon absorption to generate more electrons which in turn increase the absorption rate (Radziemski and Cremers 1987). Through the three mechanisms presented, plasma formation and growth can occur when a sample volume is exposed to a high irradiance source.

After the source of irradiance is terminated, free electrons recombine with ions to form atoms and molecules. This process is much longer temporally than the time needed for plasma generation. As stated previously, upon recombination electrons lose ionization energies pertaining to the particular electronic state to which they return. These energies are emitted as photons which can be spectrally resolved using a spectrometer and associated detection optics. In addition, neutral atoms emit as their electrons return to their normal, lower energy levels. A study of the emission spectrum from a plasma will show a broad continuum of emission that decays with time and

wavelength. Emission lines for individual atomic species produce intensity peaks on top of the continuum proportional to atomic concentration. For short delay times after plasma generation the continuum dominates the spectrum. As the continuum decays with time, emission lines appear. The first emission lines are from atoms still in an ionic state after recombination, followed by neutral atoms and finally at long delays molecular emission can be observed if sufficient emission intensity exists. Using time-resolved LIBS to only collect emission in a specified delay window after plasma generation, individual species can be identified and quantified using known emission lines.

2.2.2 LIBS of Hydrogen Gas

LIBS is an atomic emission spectroscopic technique, therefore identification and quantification of hydrogen gas molecules must practically be accomplished by examining the hydrogen atomic emission from the plasma. For this reason, care must be taken to prevent other hydrogen containing species from entering the sample volume otherwise false identification of hydrogen gas can occur. This requirement is addressed for detection implementation later in this work. With this noted, plasma generation must first be achieved by exceeding the dielectric threshold for breakdown in the gaseous sample volume. For reference, the breakdown threshold in air has been observed to range from 10-1600 GW/cm², therefore breakdown varies greatly with experimental conditions (Simeonsson and Mizeolek 1994, Smith et al. 2001). Due to this variation, a high irradiance source, such as a focused laser beam, is imperative to ensure uniform breakdown in the sample volume. Once breakdown is achieved, hydrogen emission from plasmas is characterized by specific spectral emission lines corresponding to photons released during atomic transitions. The location of these lines can be calculated for specific transitions using binding energies for hydrogen electrons and associated

transition probabilities. Hydrogen lines for transitions involving the first three energy states were some of the first spectral lines ever calculated and are divided into the Lyman, Balmer, and Paschen series based on the investigator who discovered the transitions.

Table 2.2 gives some selected emission lines for each series along with the energy levels involved in each transition.

Table 2.2 Selected hydrogen atomic transition lines.

Series	Quantum Number		Energy levels		Emission Wavelength (nm)
	j (lower state)	k (upper state)	E _j (cm ⁻¹)	E _k (cm ⁻¹)	
Lyman	1	2	0	82,259.27	121.57
	1	3	0	97,492.32	102.57
	1	4	0	102,823.9	97.25
	1	5	0	105,291.65	94.97
	1	6	0	106,632.16	93.78
	1	∞	0	-	92.26
Balmer	2	3	82,259.27	97,492.32	656.27
	2	4	82,259.27	102,823.9	486.13
	2	5	82,259.27	105,291.65	343.04
	2	6	82,259.27	106,632.16	410.17
	2	∞	82,259.27	-	383.54
Paschen	3	4	97,492.36	102,823.9	533.16
	3	5	97,492.36	105,291.65	779.93
	3	6	97,492.36	106,632.16	913.98
	3	∞	97,492.36	-	994.81

Source: NIST Atomic Spectra Database

All of the given atomic transitions for hydrogen can be used for species identification and quantification, but certain lines are preferred based on relative intensity and detection regime. Traditionally, the first transition in the Balmer series between $j=2$ and $k=3$ is used for spectroscopy because it has a higher relative intensity compared to the other lines and occurs in the red regime of the visible spectrum. Figure 2.4 gives an example spectrum for this atomic transition line which is referred to as the H_α line.

This line was chosen for identification of hydrogen in this study due not only to its intensity but also because its properties have been widely characterized. The broad width

of the line can be attributed to broadening mechanisms, particularly Stark broadening, associated with the behavior of the electrons in the plasma. Stark-broadening occurs as a result of electrons impacting one another during translation in the plasma thus slightly shifting their energy in response to a transfer of collision energy. This shift in energy changes the energies of the photons released during atomic transitions thus causing a variation in the energy of emitted photons. A range of photon energies are responsible for broadening of the line as shown Figure 2.4. Through theoretical modeling of plasma dynamics, the full width at half max (FWHM) of the transition line can be correlated to electron density for plasma analysis. A description of Stark-broadening calculations are presented in Chapter 3.

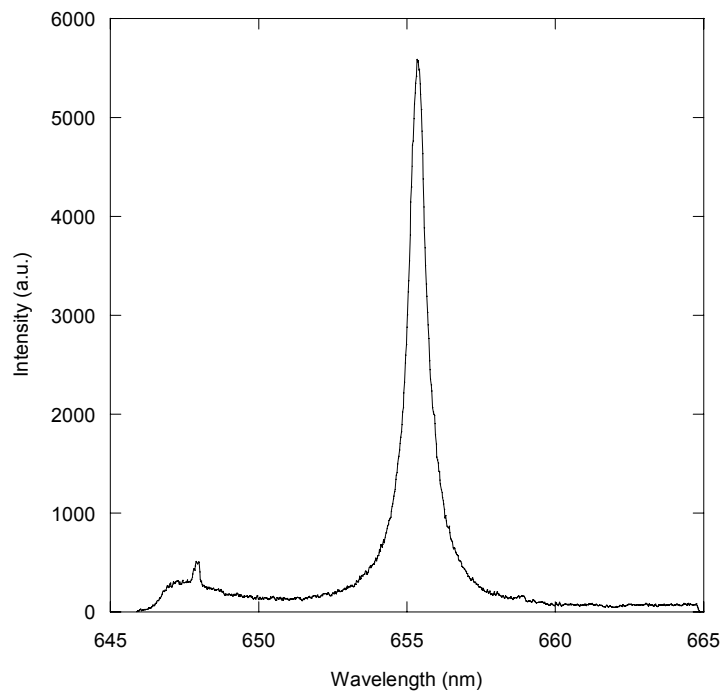


Figure 2.4 Example spectrum showing the H_{α} line from hydrogen emission.

2.2.3 Practical LIBS-based hydrogen detection schemes

To the knowledge of the author, no previous schemes have been presented using the LIBS technique for the practical detection of hydrogen gas. With that stated, LIBS

has been used for the practical detection of many other gaseous species. Dudragne et al. reported on the use of LIBS for detection of fluorine, chlorine, sulfur and carbon in air for pollution monitoring applications. Detection and quantification of all species were achieved with the following detection limits: 36 ppm for carbon, 20 ppm for fluorine, 90 ppm for chlorine, and 1500 ppm for sulfur. The authors noted that while improvements in sulfur detection schemes were still needed and an order of magnitude increase in sensitivity was needed to achieve detection for the tested toxic agents, LIBS provides advantages over other detection schemes by allowing *in situ* detection, simple instrumentation to avoid contamination, automated detection, and multiphase detection. Williamson et al. reported on detection of halon replacement compounds for fire suppression testing and atmospheric pollution monitoring. Fluoride emission lines were used for detection with detection limits of 38 to 60 ppm achieved for different laser energies. It was determined that the *in situ* and real-time measurement abilities of LIBS made it a promising technique for fire suppression testing. Tran et al. also examined fluoride emission as part of a study on gaseous and particulate fluoride emission using LIBS with applications to the aluminum processing industry. Detection limits of 5 mg/m³ in a helium gas sheath and 40 mg/m³ in air were realized for gaseous fluorides while 0.5 mg/m³ and 9 mg/m³ were found with the same respective conditions for particulate fluorides. These detection schemes for gaseous species demonstrate that LIBS can obtain low limits of detection while being simplistic enough to allow for easy implementation. With the possibility of real-time monitoring, LIBS is believed to be a second technology that allows for improved hydrogen leak detection and increased hydrogen safety in a point sensing format.

CHAPTER 3 EXPERIMENTAL METHODS

Two spectroscopic techniques were examined as potential detection techniques for gaseous hydrogen: spontaneous Raman spectroscopy and laser-induced breakdown spectroscopy (LIBS). Investigation of each technique required a specific experimental setup and associated methodologies. In addition, multiple optical configurations were attempted to examine the effect of component parameters on detection ability and scanning electron microscopy was used for substrate characterization. The content of this chapter illustrates and describes each experimental setup for both employed spectroscopic techniques as well as the associated procedures and analysis methodologies employed. The results of all experimentation are examined in Chapter 4 and Chapter 5.

3.1 Laboratory Hydrogen Detection using Raman Spectroscopy

A backscatter orientation was chosen for the Raman instrumentation. As discussed in Chapter 3, spontaneous Raman scattered light has no angular dependency for vertically polarized incident light. The backscatter orientation was chosen as the preferred orientation for several important reasons. The most important benefit of this orientation is optical alignment of the sample. If collection of the scattered light is achieved at any angle between 0° and 180° with respect to the incident excitation axis, any adjustment of the sample distance along the incident axis results in optical misalignment of the collection axis. In the backscatter configuration, the collected light is coaxial with the incident beam thus any change in sample distance does not disturb the collection axis but rather only affects the focal point location. For large sampling distances, the light is

essentially collimated once it reaches the collection optics thereby reducing any effect of variation in focal point location. Employing a collection lens with a long focal length also minimizes the focal point variation at closer regimes. A second advantage of a backscatter orientation is that all required optics and hardware for excitation and collection can be combined at one location. This allows single event optical alignment with the sample location thus minimizing uncertainty in measurements. This orientation also has obvious benefits for any practical application of Raman spectroscopy for field detection by allowing a single location for all equipment and testing. Using the backscatter orientation, a laboratory Raman hydrogen detection scheme was constructed to examine the detection limits and sensitivity of remote hydrogen detection by spontaneous Raman spectroscopy.

3.1.1 Experimental Apparatus

Figure 3.1 illustrates the experimental apparatus used to perform all laboratory hydrogen detection investigations of Raman backscattering. While optical layout was maintained for all experiments, the components were interchanged contingent upon the parameters of the experiment, namely optic size, filter configuration and excitation wavelength. A comprehensive listing of all primary optical components comprising the laboratory Raman setup shown in Figure 3.1 is given in Table 3.1 including all specifications and manufacturer information. The excitation source for this system was a Q-switched, 1064 nm Neodinium:Yttrium-Aluminum-Garnet (Nd:YAG) laser operating at a 10 Hz repetition rate with an approximate 5 cm beam diameter. The use of a solid-state Nd:YAG laser was preferred in this application due to the high power output. The laser was used in both the frequency-doubled and frequency-tripled configuration to achieve experimental excitation wavelengths of 532 nm and 355 nm respectively.

Frequency changes were accomplished by the use of non-linear doubling and tripling crystals. The laser was used with an internal seeding laser to provide temporal stability for the laser pulse. Upon exiting the laser, the laser beam was turned by two 45° dichroic mirrors rated at the desired harmonic frequency, dependent on the experiment.

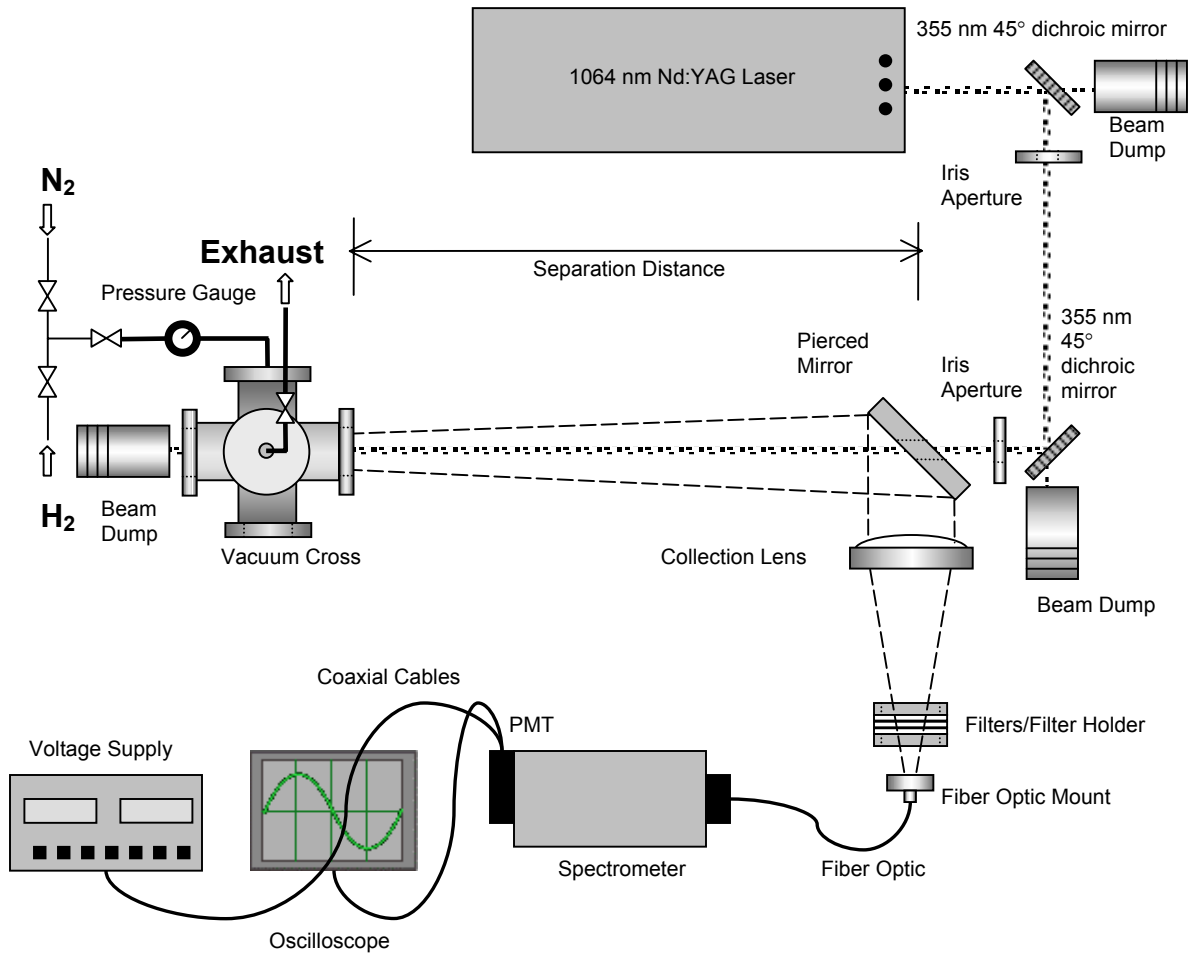


Figure 3.1 Experimental apparatus used for laboratory hydrogen detection limit investigations by Raman scattering. The incident laser is depicted by the speckled line and the backscattered light is illustrated by the dashed lines. A PMT and CCD coupled to the spectrometer were used for detection limit studies although only the PMT is illustrated.

Table 3.1 All critical components and specifications for the laboratory Raman setup. All components correspond to those shown in Figure 3.1 and are listed in order along the laser propagation path. Components labeled with an asterisk (*) were interchanged based on experimental configuration. Components with a cross (†) were used only for the CCD based experiments.

Component	Specifications	Vendor	Part No.	Quantity
Laser	Nd:YAG 1064 nm, frequency doubled/tripled 532/355 nm, 10Hz repetition rate, pulse energy varied	Continuum	Precision II	1
1 st Turning Mirror*	First laser turning mirror, 45° dichroic, 355 nm, 2" diameter	CVI Laser Coporation	Y3-2037-45-UNP	1
2 nd Turning Mirror*	Second laser turning mirror, 45 ° dichroic ,355 nm, 2 inch diameter	CVI Laser Coporation	Y3-2037-45-UNP	1
1 st Turning Mirror*	First laser turning mirror, 45 °, 532 nm, 2 inch diameter	CVI Laser Coporation	Y3-2037-45-UNP	1
2 nd Turning Mirror*	Second laser turning mirror, 45 °, 532 nm, 2 inch diameter	CVI Laser Coporation	Y3-2037-45-UNP	1
Square Pierced Mirror*	75 mm x 75mm x 1mm, center pierced-0.5 inch ±0.2" diameter	Rolyn Optics	60.245	1
Square Pierced Mirror*	100 mm x100 mmx1 mm, center pierced-0.5 inch +0.2" diameter	Rolyn Optics	60.2475	1
Collection Lens*	2" Plano-convex	CVI Laser Coporation	PLCX-50.8-51.5-UV-355	1
Collection Lens*	4" Plano-convex	Comar	160-PG-100	1
High Pass Filter*	395 nm cutoff	Comar	395-GY-50	1
High Pass Filter*	375 nm cutoff	Comar	375-GY-50	1
High Pass Filter*	385 nm cutoff	CVI Laser Coporation	CC-GC-385-1.00-2	1
High Pass Filter*	630 nm cutoff	Comar	630-GY-50	1
Line Filter*		Comar	685-IH-25	
Neutral Density Filters	Various Attenuations Used	Optics for Research	FEU-	3
Spectrometer	0.3 m Grating Monochromator/Spectrograph	Action Research Corporation	SpectraPro 300i	1
CCD†	Intensified CCD, WinSpec software	Princeton Instruments	PI-MAX	1
Photomultiplier Tube (PMT)	Photomultiplier Tube	Hammatsu	Type: R2949 No. QQ0181	1
PMT Housing	Housing for Hammatsu R2949 Tube	Products for Research, Inc.	PR1402CE	1
Oscilloscope	4 Gs/s, 50 Ohm coupled resistor, 2 channel	Lecroy	Waverunner LT372	1
Power Supply	High Voltage Power Supply	Stanford Research Systems, Inc.	Model PS325	1
Gas Chamber	304 stainless steel 2" O.D. 5 way gas cell, UV quartz front window, Glass back/side window, copper gaskets	Huntington Labs	VF-5200	1
Software	Spectroscopic Software	Princeton Instruments	Winspec	1

An iris aperture following each dichroic mirror was adjusted to just larger than the beam diameter to eliminate any residual wavelengths from frequency conversion. This was possible because the dichroic mirrors are designed for optimum 45° first-surface reflectivity at the chosen wavelength and thus “turn” other wavelengths with different angles of reflection for the first and second surface. Once on axis with the sample, the laser beam was passed through the center of a 45° pierced mirror before it was passed through the five-flanged stainless steel sample chamber at the experimentally designated separation distance. The sample distance was measured from the center of the chamber to the center of the pierced collection mirror.

The sample chamber used was a sealed five-way stainless steel vacuum cross chamber with two ultraviolet grade quartz flange windows along the sample axis and a glass flange window for visual monitoring perpendicular to the sample axis. Attached to the other two cross flanges were a gas input flange with an attached valved fitting tree plumbed to gas cylinders and a dial pressure gauge, and a gas output flange on the top of the cross with an attached valve for exhausting the gas chamber.

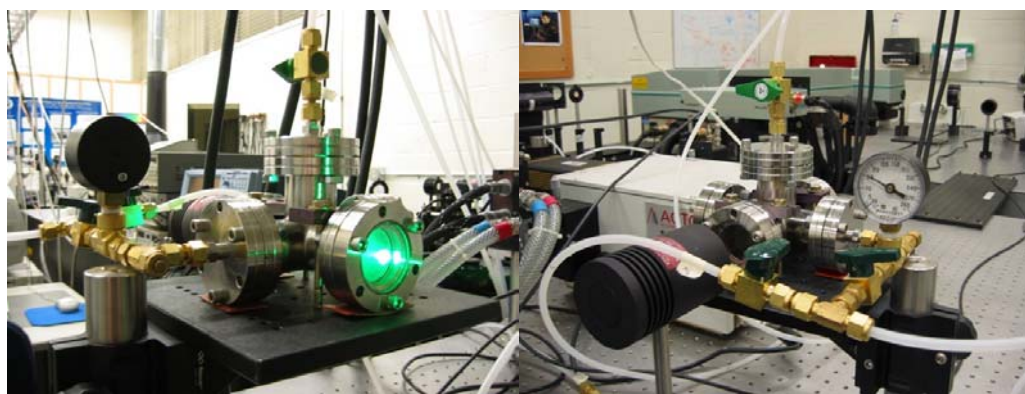


Figure 3.2 Stainless steel sample chamber used for all Raman hydrogen detection experiments.

Once the beam passed through the sample chamber, it was terminated in a cylindrical, conical termination, beam dump mounted behind the second quartz window. A front and rear picture of the sample chamber are given in Figure 3.2. Due to the high pulse energies being used in this experiment, reflected radiation had sufficient intensity to ablate collection optics. Therefore, care was taken to prevent back reflections from the front surfaces of the quartz windows from entering the detection optics along the beam axis. This was accomplished by rotating the sample chamber on its support pole 5-10° to angle the back reflections to an off axis beam dump in front of the chamber in which they were terminated. This rotation and associated reflections are not depicted in Figure 3.1.

As shown in Figure 3.1 by the dashed lines, the Raman shifted back-scattered photons from the sample were collected by means of a square pierced mirror. The pierced mirror was set at an angle of approximately 45° to direct the backscattered photons into a perpendicular collection lens. The pierced hole only accounted for an approximate five percent loss in collected photons with respect to the full area, so its effect was considered negligible. Two collection lenses were examined for the Raman setup: a two inch diameter plano-convex lens and a four inch diameter plano-convex lens. The two lenses were examined to determine the increase in photon collection efficiency associated with lens scaling. The collection lens focused the backscattered light through a filter holder containing either high pass filters and/or line filters, depending on the experiment, to eliminate the radiation scattered at the incident laser wavelength and fluorescence radiation. Even though a diffraction grating is eventually used to separate the wavelengths in the spectrometer, the intensity of the reflected and Raleigh scattered

incident wavelength light is such that it would contribute to overall noise in the system as stray light if not removed. The collection optics and filter stackup are show in Figure 3.3

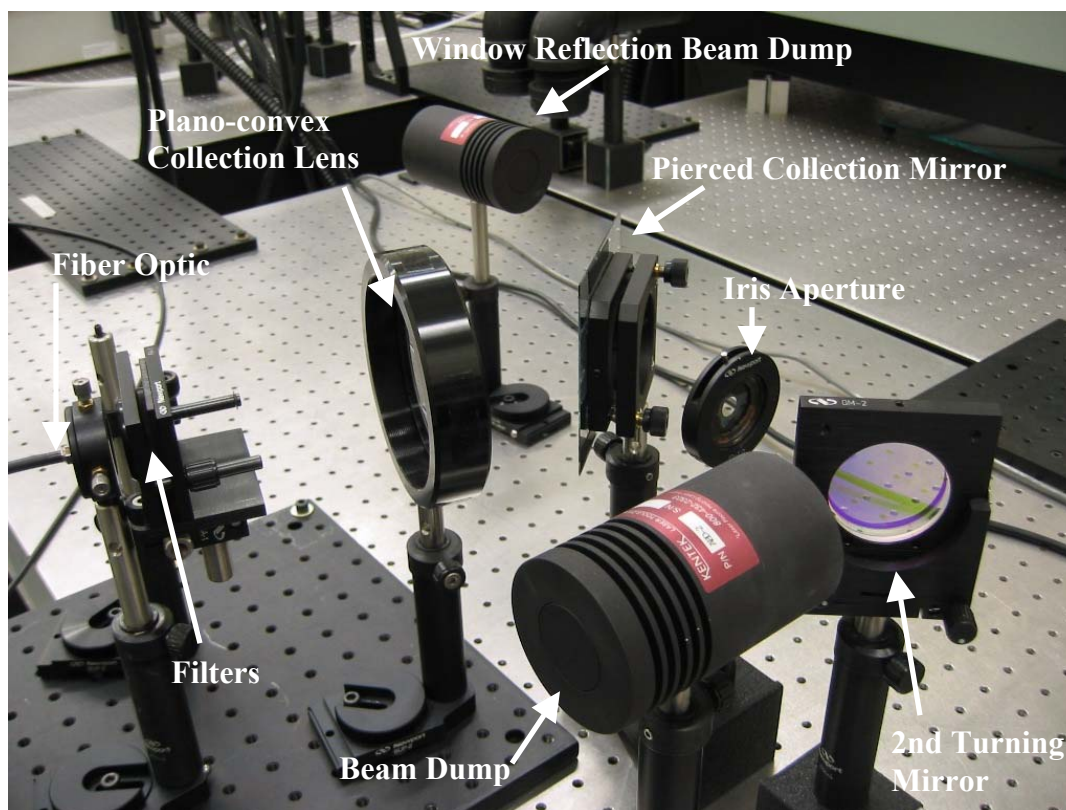


Figure 3.3 Photograph of collection optics used in the laboratory remote Raman scattering experiments.

The focused, scattered radiation was collected into a 17-fiber bundled fiber optic with a 1.2 mm diameter and input into a blazed grating diffraction spectrometer. The groove spacings of the gratings used were 1200 g/mm in the photomultiplier tube (PMT) configuration and 2400 g/mm in the intensified charge-coupled device (ICCD) configuration. Entrance slits and exit slits for the spectrometer were set at 20 μm and 50 μm , respectively, for the 2.26 m separation distance experiments and 70 μm and 50 μm , respectively, for detection at 6.58 m. The entrance and exit slits were chosen qualitatively by examining signal output with the goal of minimizing noise off the hydrogen line and maximizing signal on the line. For the predominance of the detection

limit studies, a PMT was used to quantify the scattered photons. The ICCD was used for signal characterization and select detection limit studies. In the PMT configuration, a 50 ohm terminator was coupled to a magnetically shielded output coaxial cable to transfer the signal to a digital oscilloscope. The oscilloscope sampled at a rate of 4 GS/s and 150 shots were averaged for each recorded scattering signal. With the ICCD configuration, the diffracted light from the spectrometer was focused onto the intensifier which allowed amplification of the signal through the photoelectric effect. Once intensified, the spectral profile was collected on the 1024x256 CCD chip and coupled to Winspec software which allowed spectral visualization and recording. The PMT voltages and CCD binning and gain are given below in the respective sections on each experiment with any additional experimental parameters not addressed in this description. Figure 3.4 shows a picture of the complete laboratory Raman detection system.

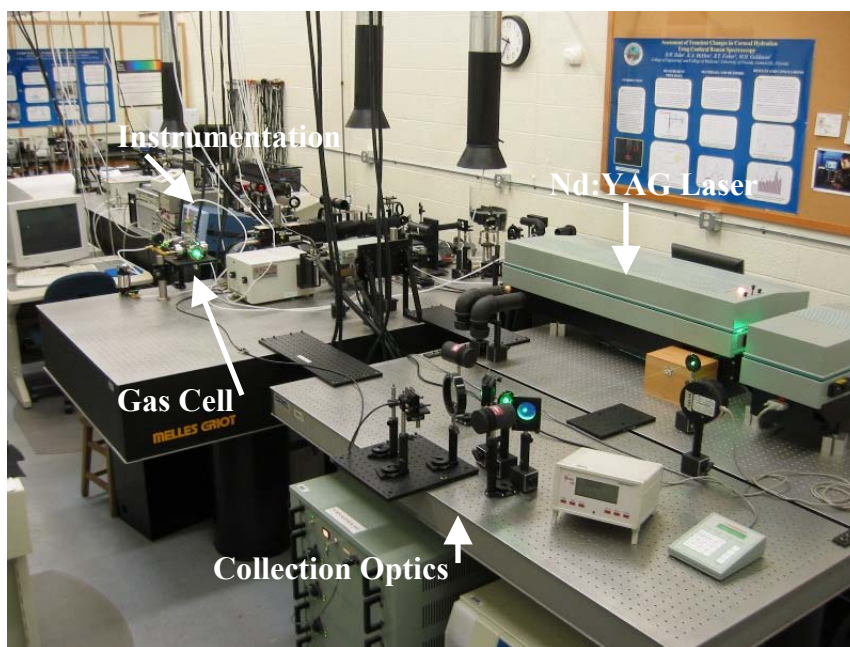


Figure 3.4 Photograph of the complete laboratory setup for the remote Raman scattering experiments.

3.1.2 Preliminary Raman Scattering Investigation

A preliminary set of experiments were conducted using the Raman backscattering setup shown in Figure 3.1 to determine if detection of hydrogen at a significant concentration level could be achieved. A 75 mm square pierced collection mirror and 2” plano-convex collection lens were used for signal collection. A separation distance of 6.58 m was used between the cell and the collection mirror. For noise reduction, a single high pass filter was used with a cutoff of 385 nm in the initial investigation. A PMT voltage of 782 V was chosen to yield as much gain as possible for the detected signal while maintaining signal linearity. Pure pressurized hydrogen and/or industrial grade nitrogen were used for experimentation in the gas cell to achieve a range of hydrogen concentrations for these initial experiments. The concentrations were achieved by pressurizing the cell at 30 psig with hydrogen and decreasing the pressure incrementally by 5 psig down to 0 psig during the course of the experiment. After measurement at 0 psig, the cell was repressurized up to 14.69 psig or 1 atm then exhausted back to 0 psig to achieve a 50/50 hydrogen to nitrogen mixture. The same procedure was repeated for the final measurement to achieve a 25/75 hydrogen to nitrogen mixture. Using the ambient temperature of 22° C for all experiments as measured by a thermocouple on the gas cell, Table 3.2 gives the concentrations achieved in the sample cell over the pressure range used in the experiments. Excitation was achieved at 355 nm with a 10 Hz repetition rate and a pulse energy of 215 mJ/pulse. As shown in Chapter 2, Raman shifted photons with a shift of 4156 cm^{-1} at an incident wavelength of 355 nm are observed at 416.01 nm. Since the exact calibration of the spectrometer was not initially known, any signals recorded with the 416.01 nm setting on the spectrometer might have been from wavelengths off the hydrogen Raman peak.

Table 3.2 Hydrogen concentrations used in the preliminary Raman investigations. All samples were tested at 22° C.

Total Cell Pressure (psig)	Hydrogen % by volume	H2 Concentration (mol/L)
30	100	0.126
25	100	0.121
20	100	0.105
15	100	0.090
10	100	0.075
0	100	0.045
0	50	0.022
0	25	0.011

Therefore, a set of preliminary measurements were recorded over a range of wavelengths from 415.51-416.51 nm to find the spectral location of the Raman line. For these measurements, the scattering signal was measured at ten wavelengths from 415.51 nm to 416.51 nm for three different pressures, namely 10, 20 and 30 psig. All hydrogen scattered light was observed at a delay of 0.27 μ s with respect to the Q-switch trigger. The resulting signals were examined by wavelength to determine the wavelength of maximum intensity signifying the center of the Raman line. These results are presented in Chapter 4. It was found from these measurements that maximum scattering signal corresponded to the spectrometer centered on 415.91 nm. This location was then used for all on-peak measurements of the scattering signal.

Three sample sets of data were taken in the preliminary experiment to examine the scattering response to concentration. Each sample set consisted of PMT signals recorded for the nine wavelengths given in Table 3.3. The reason for sampling over the given range of wavelengths was to achieve two signals off the hydrogen peak, at 413.91 nm and 417.91, to be used as baseline measurements. In addition, signals corresponding

to multiple wavelengths around 415.91 nm were taken to monitor any unexpected spectral shift in the maximum signal.

Table 3.3 Wavelengths used for sample collection in the preliminary scattering investigations.

Sampling Wavelength (nm)	Signal
413.91	Baseline
414.91	
415.41	
415.71	
415.91	H ₂ Peak
416.11	
416.41	
416.91	
417.91	Baseline

Using the measured offline signals and Raman on-line signal, scattering response could be examined as a function of concentration.

The analysis of all PMT Raman scattering signals first required the elimination of all background noise from the Raman scattering signal. For the preliminary experiments, simple noise subtraction was used. To accomplish this, two baseline measurements corresponding to 413.91 nm and 417.91 nm were averaged to yield one average baseline noise signal. Figure 3.5 shows two arbitrary baseline PMT measurements as well as the average baseline and the hydrogen peak signal corresponding to the scattered light at 415.91 nm from the spectrometer. Determination of the origin of each of the two peaks observed in each signal will be discussed in Chapter 4 but for analysis purposes it is stated that the first peak shown is due to stray light and the second peak is the scattering response used for analysis. The PMT output is a negative voltage due to the negative source voltage used to power the PMT but all processed signals will be presented in an inverted format for clarity.

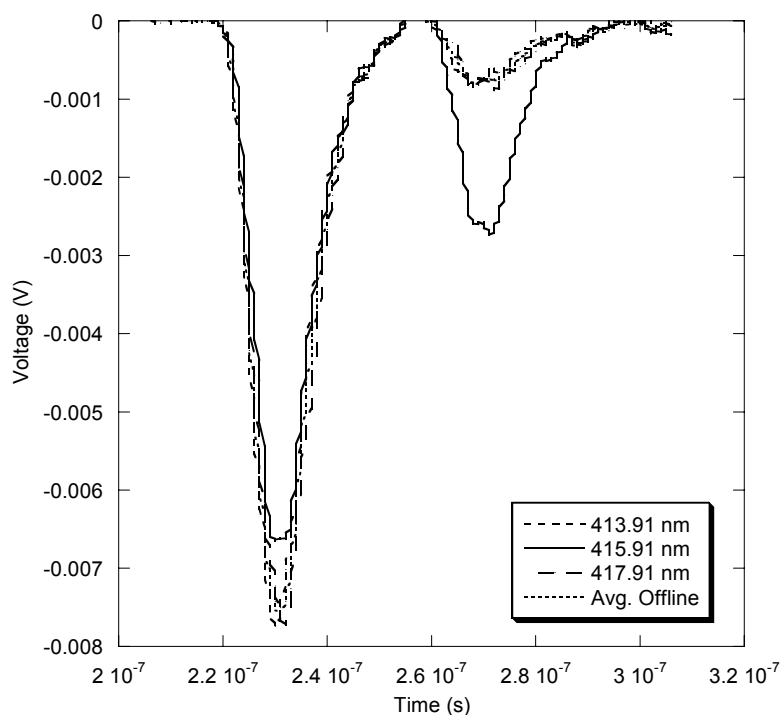


Figure 3.5 PMT signals showing the Raman scattering signal at 415.91 nm and the two offline measurements along with their average.

The average offline signal was subtracted from the Raman scattering signal to yield an absolute Raman scattering signal. Discretized integration of the absolute signal was used to quantify the scattering signal for examination of the response to hydrogen concentration variation.

3.1.3 Detection limit determination

Once preliminary investigations showed the ability of hydrogen to be remotely detected using spontaneous Raman backscattering, experiments were conducted to determine if limits of detection for hydrogen lower than the flammability limit of 4% by volume could be achieved. In addition, two excitation energies were examined to demonstrate the dependence of the detection limit on incident wavelength.

For these experiments, the Raman system shown in Figure 3.1 was again used but the separation distance was reduced to 2.26 m to increase photon collection efficiency.

The 75mm square pierced collection mirror and 2" collection lens were again used. Both 355 nm and 532 nm radiation were used for excitation at a pulse energy of 244 mJ/pulse. The laser turning mirrors were interchanged according to wavelength as specified in Table 3.1. A single high pass filter with a 385 nm cutoff for the 355 nm experiments or a 685 nm cutoff for the 532 nm experiments was used to reduce scattered light at the incident frequency. As before, scattering signal measurement was achieved using a PMT and oscilloscope. A constant 20 μm entrance slit width and a 50 μm exit slit width for the spectrometer were used at both wavelengths.

Concentrations were tested spanning two orders of magnitude across the lower flammability limit of 4% by volume. The concentrations tested are given in Table 3.4 for all detection limit experiments.

Table 3.4 Concentrations used for the first detection limit study. All concentrations correspond to an ambient temperature of 25° C.

Pressure (psig)	% H ₂ by volume	Concentration (mol/L)
0	100	0.04090
0	50	0.02045
0	25	0.01022
0	12.5	0.00511
0	6.25	0.00256
0	3.125	0.00128
0	1.5625	0.00064
0	0.78125	0.00032

These concentrations were achieved as before using a pressure manipulation procedure. For the first measurement, the gas cell was pressurized using pure hydrogen and vented repeatedly to expel all other gases from the cell and achieve a pure hydrogen sample. A final pressurization was done after gas expulsion and the cell was subsequently vented to atmospheric pressure for the first measurement of 100% hydrogen. After signal collection, the cell was pressurized with industrial grade nitrogen to 14.69 psig and then

vented back to atmospheric pressure to achieve a mixture with 50% hydrogen by volume. This procedure was repeated to achieve all subsequent concentrations.

The concentrations spanned two orders of magnitude therefore scattering signal intensity varied by several orders of magnitude. To achieve high gain at low scattering intensities yet maintain linearity over this range, neutral density filters coupled with a high PMT voltage of -900 V were used for all measurements. Neutral density filters attenuate radiation at all wavelengths by an amount dependent on their rating. Filters were interchanged between concentrations as needed to maintain linearity for all measurements. Table 3.5 lists the attenuation factor of the filter used at each concentration and excitation wavelength. The attenuation factor is the value by which the signal intensity is divided using that particular filter.

Table 3.5 Listing of attenuation factors corresponding to neutral density filters used to maintain signal linearity by excitation wavelength and concentration.

% H ₂ by volume	Concentration (mol/L)	Attenuation factor	
		355 nm	532 nm
100	0.04090	5.99	2.00
50	0.02045	5.99	2.00
25	0.01022	3.99	1.00
12.5	0.00511	2.00	1.00
6.25	0.00256	2.00	1.00
3.125	0.00128	2.00	1.00
1.5625	0.00064	1.00	1.00
0.78125	0.00032	1.00	1.00

The effect of individual attenuation was removed during analysis by multiplying measured signals by the corresponding attenuation factor prior to calculations.

Signal collection was performed as for previous scattering measurements except only two offline measurements separated by 1 nm were taken for each Raman on-line measurement. For the 355 nm experiments, offline measurements were taken at 414.91

nm and 416.91 nm. As with the Raman line corresponding to 355 nm excitation, the Raman shift of 4156 cm^{-1} with 532 nm excitation was not observed at the theoretical line location of 683.03 nm due to calibration effects of the spectrometer. By the same scanning method used for 355 nm excitation, it was found that the Raman line for 532 nm excitation was located at 682.98 nm. The corresponding offline measurements were taken at 681.98 and 683.98 nm. In addition to these measurements, a dark noise measurement was taken with the laser shutter closed and all other experimental conditions held constant to examine the dark noise associated with the experimental system. Three sample sets, each containing measurements for the concentrations shown in Table 3.5, were taken at each excitation wavelength for a total of six data sets.

The collected Raman scattering signals and offline measurements were analyzed by first finding an average offline signal as before. The dark noise was then subtracted from both the average offline signal and the Raman line signal. This yielded an average offline signal that is only a result of optical noise, namely shot noise, stray light and fluorescence. Examination of this signal with the purpose of increasing the signal to noise ratio for all measurements is discussed in Chapter 4. The offline optical noise signal was then subtracted from the dark noise-removed Raman line signal and the resulting absolute peak was discretely integrated to achieve the scattering signal for each concentration and excitation wavelength.

With the scattering signals known as a function of concentration, a limit of detection (LOD) was calculated based on three times the standard deviation in the noise level. The detection limit determines the minimum detectable concentration within statistical significance. The limit of detection was calculated by Equation 4.1 where σ

was the standard deviation of the noise and m was the slope or sensitivity of scattering response curve in L/mol.

$$LOD = \frac{3\sigma}{m} \quad \text{Equation 4.1}$$

To calculate the limit of detection, a linear regression of the scattering response to concentration and the fluctuation in the offline background noise level were needed.

Figure 3.6 shows the scattering response for 355 nm excitation along with the associated linear regression of the response.

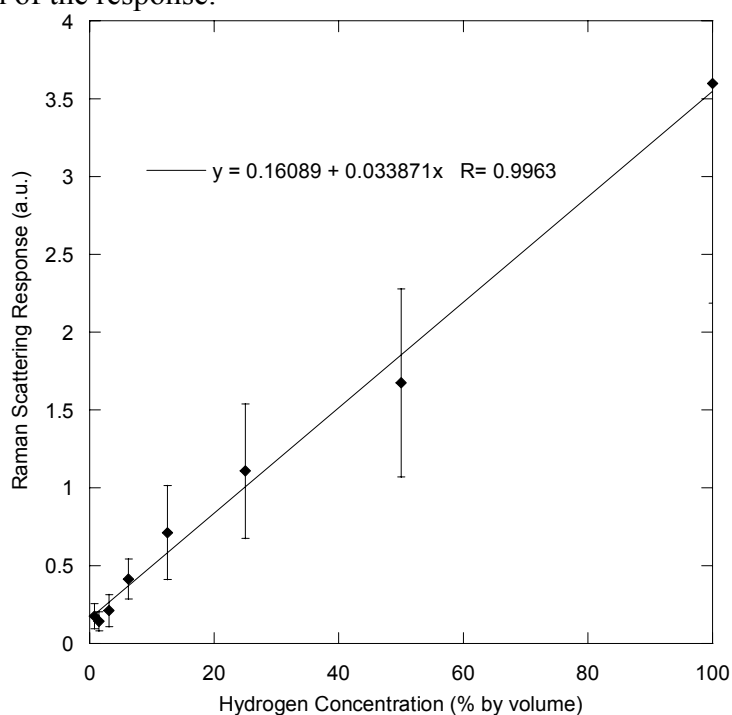


Figure 3.6 Scattering response at 355 nm showing a linear regression used for LOD determination.

As shown by the grouped data points in Figure 3.6, the final experimental measurement at 0.7812 % hydrogen by volume was at the noise level therefore it was not a detectable a signal but rather noise itself. The standard deviation in noise was found by examining the standard deviation for the previously calculated scattering response at 0.7812%. With

the standard deviation of the noise known, the limit of detection was calculated for the averaged 355 nm and 532 nm sample sets. These results are presented in Chapter 4.

3.1.4 Optical Configuration Effects on Detection Limit

With detection limits examined in the previous experiments, experimental parameters were subsequently examined to determine if detection limits could be decreased, sensitivity could be improved and an increase in signal to noise could be achieved. In addition to reexamining differences in scattering response at the two incident wavelengths of 355 nm and 532 nm with added optical filters for noise reduction, variation of the collection lens from 2" to 4" with the collection mirror increased to a 100 mm square pierced mirror and the use of two excitation pulse energies of 125 mJ/pulse and 250 mJ/pulse for each incident wavelength were examined.

A note should be made on the pulse energies used for all Raman detection limit experiments. The pulse energies were measured using a Scientech Model AC5001 Calorimeter placed in the beam path prior to the second turning mirror but after the first iris aperture. Thus these energies account for the optical losses associated with the first dichroic turning mirror and the first iris aperture. It must be noted that further losses are associated with optics past the point of measurement. The second turning mirror had a one percent optical loss, the second iris aperture a five percent associated loss, and a four percent loss was associated with the quartz gas cell window. Accounting for these losses, the true pulse energies seen by the gas sample in the cell during experimentation were approximately 113 mJ/pulse and 226 mJ/pulse. With these actual energies noted, the pulse energies will be referenced in the remainder of this work by the power meter pulse energies of 125 mJ/pulse and 250 mJ/pulse.

The experimental setup for these investigations used a separation distance between the mirror and collection optics of 2.36 m due to repositioning of the experiment to accommodate large collection optics. As noted above, the collection mirror was increased to a 100 mm square pierced mirror to increase the solid angle of collection. The specifications for this mirror along with any additional components for these experiments are listed in Table 3.1. Two additional high pass filters with cutoffs at 395 nm and 375 nm were added in addition to the line filter with a 385 nm cutoff for the 355 nm experiments to aid in noise reduction. For the 532 nm experiments, a line filter centered at 685 nm was added in addition to the 630 nm high pass filter to again reduce noise due to stray light. Black felt was used to mask off the collection optics from the collection lens back to the fiber holder for added noise reduction. As stated before, experiments were performed using either a 2" or 4" plano-convex collection lens, a pulse energy of 125 mJ/pulse or 250 mJ/pulse and an excitation wavelength of 355 nm or 532 nm. The lower 125 mJ pulse energy was examined for field detection purposes since a field deployable laser will not be able to achieve pulse energies as high as the Continuum laser used for laboratory investigations. Table 3.6 lists the exact configurations of optical components examined for hydrogen detection ability.

Table 3.6 Experimental configurations used for configurational detection limit studies.

Wavelength (nm)	Pulse Energy (mJ/pulse)	Collection Lens Diameter (in)	Number of Data Sets
355	125	2	4
355	250	2	4
355	125	4	4
355	250	4	4
532	125	4	4
532	250	4	4

For all experiments, a PMT voltage of 980 V was used and signal linearity was maintained across the examined concentration range through the use of neutral density filters as discussed for the previous experiments. The concentrations used were also the same as the previous experiment, as listed in Table 3.5, and were achieved by the same pressurization and venting process described previously for the sample chamber. For each set of experimental parameters shown in Table 3.6, four sets of data were taken each containing two offline measurements and one Raman scattering on-line measurement at each hydrogen concentration. A separation distance of 2 nm was used between the on and offline measurements to reduce the effect of a broad scattering signal on the offline measurements. For 355 nm excitation, the offline measurements were recorded at 413.91 nm and 417.91 nm with the Raman line at 415.91 nm and for the 532 nm experiments, offline measurements were taken at 680.98 nm and 684.98 nm with the Raman line located at 682.98 nm. With the signals collected, an average baseline subtracted offline signal and a baseline subtracted Raman scattering signal were calculated. Instead of subtracting the average offline signal from the Raman scattering signal, the peak of each signal was discretely integrated and the resulting integrated area of the average offline signal was subtracted from the integrated area of the Raman scattering signal to achieve the scattering response. This procedure was invoked to more accurately achieve the absolute Raman scattering signal for each concentration. With all absolute Raman scattering signals calculated, a plot of the scattering response as a function of hydrogen concentration was found and a linear regression was performed. Finally, the limit of detection for each configuration was calculated following Equation 4.1.

3.1.5 Theoretical Photon Arrival Rate Determination

Theoretical photon arrival rates at the collection lens were calculated for backscattering from a free spherical sample volume in air at the detection limits achieved in the configuration experiments. The photon arrival rate, as it pertains to field detection, is the rate at which scattered photons fall incident on the collection lens. A significant number of photons are important to ensure that ample signal intensity exists for detection after losses in optical components such as fiber optics and spectrometer slits.

Spontaneously scattered Raman light in response to incident vertically polarized light scatters uniformly over a solid angle of 4π steradians. The sample volume probed for these experiments consisted of a 9.0 mm diameter cylindrical sample volume with a length of six inches in the gas cell. These dimensions translate to a sample volume of 9.695 cm^3 . Considering a spherical free sample gas volume of the same size, an approximation of the photon arrival rate at the 4" collection lens was determined by Equation 3.2. The quantities involved in the calculation are as follows: N is the number density (molecules/ cm^3), σ' is the differential scattering cross section (cm^2/sr), F_{inc} is the fluence of the incident laser pulse (mJ/cm^2), dV is the differential scattering volume (cm^3), $d\Omega$ is the differential scattering angle (sr), h is Planck's constant of $6.626 (10^{-34}) \text{ kg}\cdot\text{m}^2/\text{s}$ and ν_{inc} is the frequency of the incident photons (Hz).

$$S_{\text{Raman}} = \frac{N\sigma' F_{\text{inc}} dV d\Omega}{h\nu_{\text{inc}}} \quad \text{Equation 3.2}$$

The number density can be obtained from the concentration (mol/L) and Avogadro's number, $6.022(10^{23})$ molecules/mol. The differential scattering cross section for hydrogen at the excitation wavelengths under study are given in Chapter 2. The differential solid angle is the only quantity that is not readily determined. The solid angle

for a differential spherical surface illuminated by a point source is given by Equation 3.3 where dA is the differential spherical surface area and r is the radius to the illuminated surface.

$$d\Omega = \frac{dA}{r^2} \quad \text{Equation 3.3}$$

While the collection mirror used in the experiment is not a convex spherical surface and the sample volume has a finite cross section, certain approximations can be made based on sampling distance. From the inverse square law that relates irradiance to distance, a source may be approximated as a point source if the five times rule is obeyed. This rule states that the distance between the source and irradiated surface must be at least five times the largest dimension of the source. For the experiments performed in this body of work, the source was the circular cross section of the laser beam with a 9.0 mm diameter. The corresponding minimum distance for approximation of the hydrogen source as a point source is thus 45 mm. All separation distances used in this experiment were much greater than 45 mm therefore the sample can be approximated as a point source of Raman scattered radiation. With regard to the use of a flat surface, less than one percent error is introduced by using a flat surface in place of a spherical surface for solid angles less than 0.03 sr. All solid angles calculated in this work also met this requirement therefore flat collection optics had little effect on photon arrival rate calculation. The photon arrival rates calculated for different scattering configurations are given in Chapter 4.

3.1.6 CCD detection limit studies and spectral visualization

A final set of laboratory experiments were conducted with an ICCD used in place of the PMT for comparison of detection limits between the two detectors. A similar optic configuration to previous experiments was used with excitation at 355 nm, a 4" collection

lens and a pulse energy of 250 mJ/pulse. The separation distance was again set at 2.26 m and hydrogen/nitrogen mixtures at 25°C were used at the concentrations listed in Table 3.5. Three high pass filters with cutoff wavelengths of 395 nm, 375 nm and 385 nm as listed in Table 3.1 were again used for elimination of scattered or stray light at the incident wavelength. The spectrometer grating was adjusted to 2400 grooves/mm to increase signal resolution on the ICCD. The ICCD was operated at a gain of 250 with a gate delay of 50 ns and a gate width of 250 ns. The gate delay and width were set by qualitative examination of signal intensity.

The ICCD records a time accumulated spectrum around the Raman line of interest as opposed to the transient signal of the PMT for one wavelength, therefore offline measurements were not needed. In order to examine the scattering response, three ICCD spectra were recorded for the Raman line at each concentration. Each spectra consisted of 150 accumulated shots therefore each spectrum was divided by 150 to achieve an average spectrum similar the 150 shot average recorded in PMT measurements. Figure 3.7 shows one averaged spectrum for hydrogen at 100% by volume. The spectrum shows a relatively constant high baseline signal at an approximate intensity of 260 due to background noise and dark noise, as well as the inherent ICCD offset. To determine scattering response, this baseline signal had to be quantified. Using a relatively constant region of the spectrum as shown in Figure 3.7, an average baseline intensity was calculated by averaging all spectral intensities in this region. This average baseline intensity was then multiplied by the peak width in pixels to achieve an integrated baseline signal.

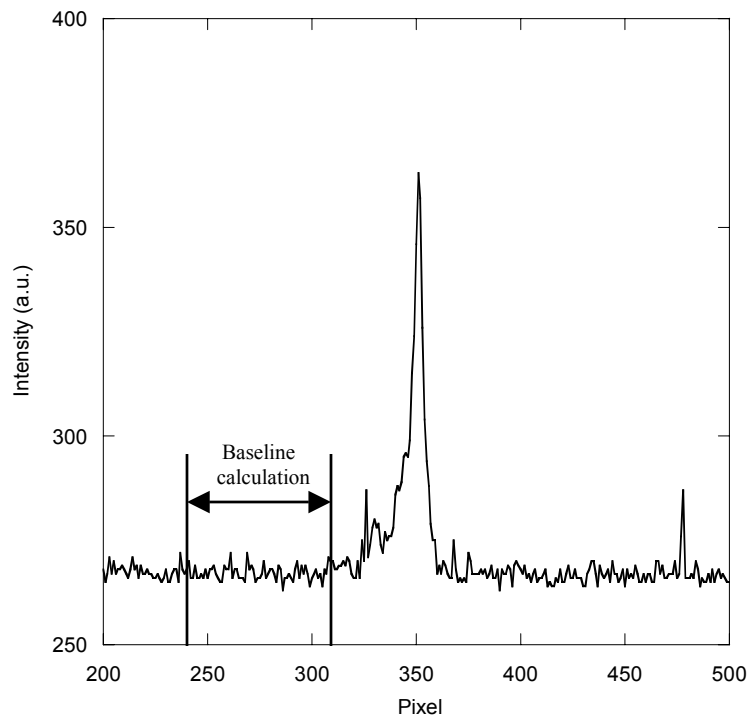


Figure 3.7 ICCD spectrum showing the Raman line at 415.91 nm for a pure hydrogen sample at atmospheric pressure. The location of baseline determination is shown.

The peak signal peak was then integrated over its full width and the integrated baseline signal was subtracted to achieve an absolute scattering response. This procedure was followed for each concentration in all three sample sets. After calculation, the scattering responses at each concentration were averaged to achieve the average Raman scattering response. Detection limits were then determined from this response in the manner described for all previous measurements.

3.1.7 Raman Field Detection Instrument

Having achieved limits of detection well below the lower flammability limit of hydrogen with high sensitivity and an increased signal-to-noise ratio (SNR), a Raman field instrument was designed to conduct hydrogen detection tests in a field environment. Construction of the field instrument was based on the same backscattering orientation

used in the laboratory with the goal of achieving a compact, robust field system. Figure 3.8 shows a picture of the optic head component layout of the field detection device and Table 3.7 gives a listing of all the components with their specifications.

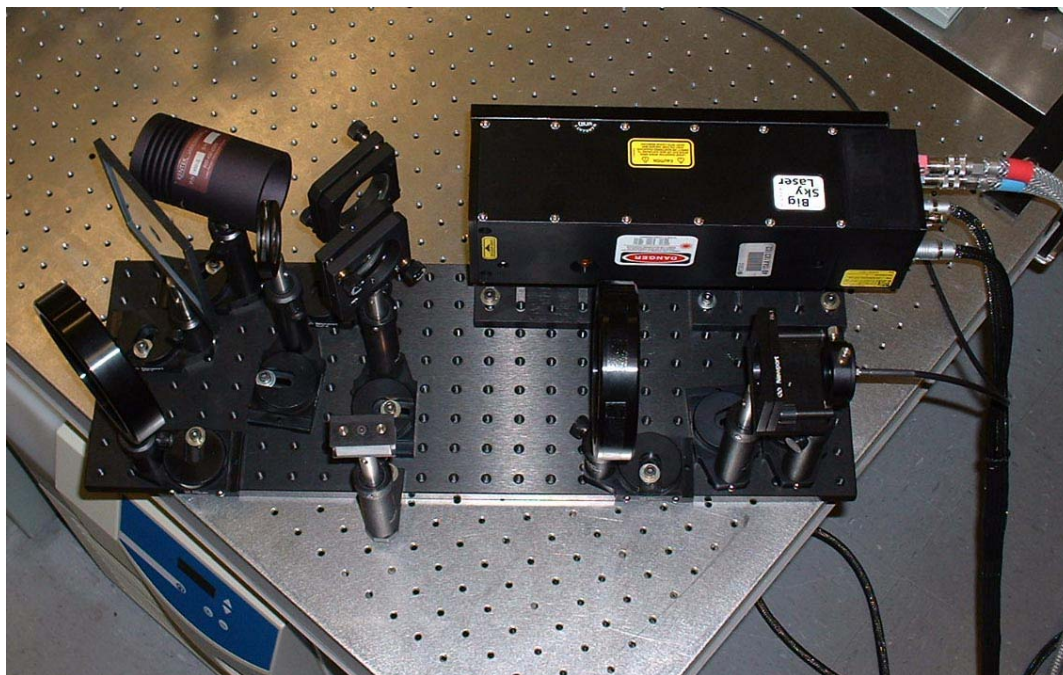


Figure 3.8 Optical head for the Raman field detection system showing the layout of all optic components.

The 1064 nm Nd:YAG Big Sky laser used for the field detection instrument had a custom configuration allowing frequency tripling to 355 nm with a pulse energy of 93 mJ/pulse in a compact, sealed and durable format. The use of 355 nm excitation was maintained even with concerns of noise caused by fluorescence because of the significant improvement in sensitivity and detection limits observed in the prior experiments due to the fourth order dependence of the scattering signal on incident wavelength. Two turning mirrors and an iris aperture were used to extract the residual 1064 nm and 532 nm laser radiation from the desired 355 nm radiation before it was passed through the 4" pierced

mirror for delivery to the sample volume. A 100 mm square pierced mirror along with a 4" round mirror and a 4" collection lens were use to collect and scatter the light.

Table 3.7 Components for the Raman field detection device.

Component	Specifications	Vendor	Part No.	Quantity
Laser	Nd:YAG 1064 nm, frequency tripled/doubled 355/532 nm, 10Hz repetition rate, pulse energy varied	Big Sky	Custom CFR	1
Mirror	First laser turning mirror, 45 degree mirror, 355 nm, 2 inch diameter	CVI Laser Coporation	Y3-2037-45-UNP	1
Mirror	Second laser turning mirror, 45 degree mirror, 355 nm, 2 inch diameter	CVI Laser Coporation	Y3-2037-45-UNP	1
Square Pierced Mirror	Backscatter collection mirror, 100 mmx100mmx1mm, center pierced-0.5 inch +-0.2" diameter	Rolyn Optics	60.2475	1
Circular Turning mirror	Melles Griot	Melles Griot	01MFG030/028	1
Collection Lens	4" backscatter collection lense, Plano-convex	Comar	160-PG-100	1
High Pass Filter*	395 nm cutoff	Comar	395-GY-50	1
High Pass Filter*	375 nm cutoff	Comar	375-GY-50	1
High Pass Filter*	385 nm cutoff	CVI Laser Coporation	CC-GC-385-1.00-2	1
Razor Edge Filter*	364 nm 99% cutoff	Semrock	LP01-364RU-25	1
Spectrometer	0.3m Grating Monochromator/Spectrograph	Action Research Corporation	SpectraPro 300i	1
Photomultiplier Tube(PMT)	Photomultiplier Tube	Hamatsu	Type: R2949 No. QQ0181	2
PMT Housing	Housing for Hamatsu R2949 Tube	Products for Research, Inc.	PR1402CE	1
Oscilloscope	4 Gs/s, 50 Ohm coupled resistor, 2 channel	Lecroy	Waverunner LT372	1
Power Supply	High Voltage Power Supply	Stanford Research Systems, Inc.	Model PS325	1

As with the incident frequency, these optics were chosen based on results from the laboratory investigations. Collection was made through the three filter stackup used in the configuration experiments. The use of a razor edge high pass filter was also examined to further reduce stray light and fluorescence noise. The testing of the field system is not included within the scope of this work but will be tested as part of future

work on hydrogen detection. Additional pictures of the constructed field device are shown in Figure 3.9.



Figure 3.9 Portable Raman field detection instrument for hydrogen detection showing the collection optics, laser, power supply, and detection instrumentation.

3.2 Laboratory Hydrogen Detection using LIBS

Laser Induced Breakdown Spectroscopy was examined in a laboratory setting to determine the limits of detection and sensitivity for hydrogen detection. As with the optical configuration for Raman spectroscopy, a backscatter orientation was chosen for collection of the atomic emission from the laser-induced plasma. While the use of LIBS for hydrogen detection does not involve propagation of emitted photons over a large distance as with the scattered photons in the remote Raman investigations, the backscatter orientation is still preferred for the associated ease of spatial alignment and for the common location of all collection optics. In addition, a backscatter orientation is necessary for substrate-initiated LIBS in which the plasma first forms on the surface and

envelopes the surrounding gas in the sample volume. A detector must be placed in the hemisphere in front of the substrate otherwise the substrate blocks photons for collection. In addition, mounting of the substrate, particularly in a gas cell as required for hydrogen detection, does not allow any angle of collection other than direct backscatter for detection. With a backscattering orientation chosen, a laboratory LIBS configuration was setup to test the limits of detection and sensitivity for a gas-initiated breakdown and a substrate-initiated breakdown. In addition, an initial investigation was performed into the lifetime and degradation of the substrate for surface-initiated LIBS.

3.2.1 Experimental Apparatus for Comparison of Gas Phase and Substrate LIBS

A laboratory LIBS setup was constructed with a backscatter orientation as shown in Figure 3.10 for an investigation of gas phase and substrate LIBS for hydrogen detection. A comprehensive listing of all included components is given in Table 3.8. A Q-switched, 1064 nm pulsed Nd:YAG laser with an 8 ns pulse width operating at 2.5 Hz was chosen as the source of irradiance for generation of the laser-induced plasma. The laser was operated at one of two pulse energies during experimentation depending on the parameters of the particular experiment. The two pulse energies used were 55 mJ/pulse and 100 mJ/pulse corresponding to voltage settings for the laser of 1.23 kV and 1.37 kV, respectively. These pulse energies were measured with a Scientech Model AC5001 Calorimeter after the focusing lens. The lower pulse energy was preferred due to its relevance to a compact field detection device but the lower pulse energy was only able to generate a substrate-initiated breakdown. The higher pulse energy was required to achieve a gaseous breakdown. The laser beam was passed through an iris aperture to ensure a concentric beam profile and then it was passed through a 0.5 inch hole in the center of a 75mm square collection mirror. A 250 mm focal length plano-convex lens

was used for focusing of the incident laser beam and attenuation/collimation of the LIBS emission. The laser beam was focused through the front window of the sample chamber to achieve breakdown at the focal spot.

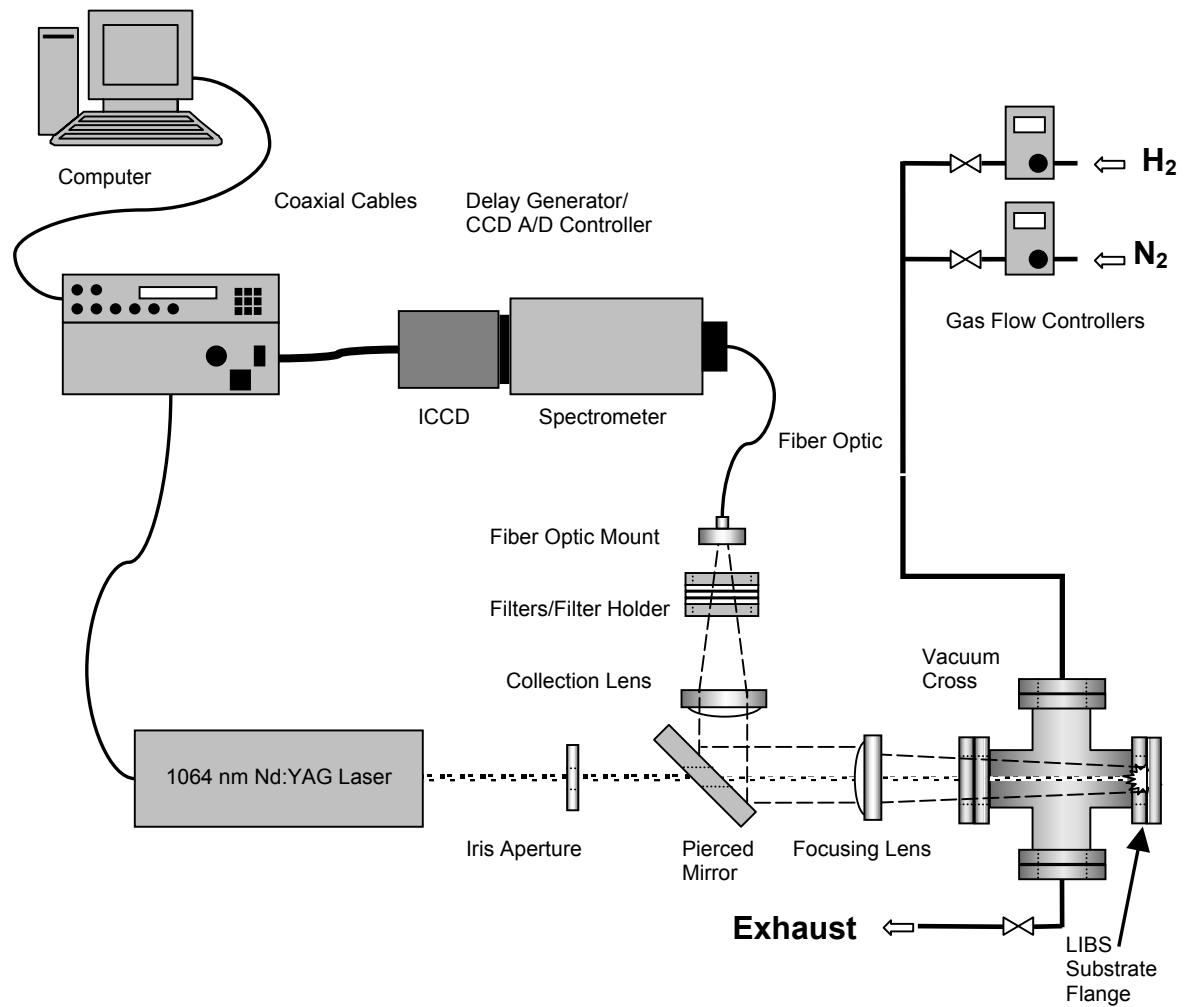


Figure 3.10 Laboratory LIBS configuration used for the hydrogen detection studies. This configuration is shown in a substrate-initiated plasma configuration but gaseous breakdowns were also achieved with this configuration by repositioning the focusing lens to achieve a focal spot in the center of the sample chamber.

Table 3.8 Listing of the optical components with specifications for the laboratory LIBS apparatus for gas-phase versus substrate LIBS comparisons.

Component	Specifications	Vendor	Part No.	Quantity
Laser	1064 nm, 5 Hz, 100 mJ/pulse (1.37 setting), 55 mJ/pulse (1.23 setting)	Big Sky Laser Technologies Inc.	Model: 230A8000 S/N1	1
Focusing Lens	Plano-convex, 250 mm focal length, 2" diameter			1
Square Pierced Mirror	75 mmx75mmx1mm, center pierced-0.5 inch +-0.2" diameter	Rolyn Optics	60.245	1
Gas Chamber	2" O.D., 304 stainless steel 4-way gas cell, solid back flange, UV grade quartz front window, copper gaskets	Huntington Labs		1
Collection Lens	100 mm focal length	CVI Laser Coporation	PLCX-50.8-51.5-UV-1064	1
Neutral Density Filters	0.3 attenuation rating used	Newport		A/R
Flow Controller	43.7 L/min flowrate; used for hydrogen	Matheson	Model 8270	1
Flow Controller	0-16 L/min hydrogen flowrate	Alicat Scientific		1
Fiber Optic	6 foot, high optical grade, 17 fiber bundle, 1.5 mm diameter			1
Spectrometer	0.275 meter Spectrometer	Action Research Corporation	SpectraPro-275, S/n 275995S	1
ICCD	Intensified CCD, 1024x256 chip	Princeton Instruments	Model: 1024MLDS-E/1, N119302	1
Software	Metal Emissions Labview Program		Custom	1

The sample chamber used for the LIBS experiments was a 4-way, stainless steel vacuum cross with a front UV-grade quartz window and a solid stainless steel rear flange along the sample axis. Attached to the two cross flanges perpendicular to the sampling axis were two gas input flanges. One flange was plumbed to two mass flow controllers connected to nitrogen and hydrogen gas cylinders. The opposite gas flange had a valve and attached gas line used for exhausting sample gases into a dedicated exhaust. A range of hydrogen concentrations were achieved in the sample cell through manipulation of the flow rates for industrial-grade nitrogen and hydrogen using flow controllers. Both flows

were subsequently combined in the fitting tree on the sample chamber gas flange. The flow rates and resulting concentrations are presented below with the experimental methodologies.

Once plasma generation was achieved in the sample chamber, emission was collected through the front gas cell window, along the beam axis in a backscatter orientation, by means of the laser focusing lens to collimate the emission and the pierced collection mirror oriented at 45° to the beam axis as shown in Figure 3.10. The redirected, collected emission was then focused by a condensing lens with a focal length of 100 mm onto a bundled fiber optic at the lens focal spot. While focusing, the emission was passed through a filter holder in which neutral density filters were placed to prevent detector saturation.

The collected emission was transmitted to a spectrometer (2400 g/mm, 0.12 nm optical resolution) and recorded with an ICCD. Gate delay and width for the ICCD were manipulated to optimize the hydrogen signal. Specific ICCD parameters are reported in the experimental results. Visualization and recording of emission spectra was achieved using an in-house Labview program.

3.2.2 Comparison of a Gaseous versus Substrate-Initiated Plasma

In order to determine the best configuration for hydrogen detection using Laser-Induced Breakdown Spectroscopy, two methodologies were examined. The first methodology examined was the use of a substrate-initiated plasma that envelopes gas from the surrounding gas stream for the purpose of hydrogen detection and quantification. The advantage of this methodology lies in the lower energy required to generate the plasma due to the higher free electron density of a solid surface in comparison to a gas. As stated in the Raman experiments, any field detection application

will be limited in excitation energy due to the need for a compact, rugged device therefore a sensitive detection technique with low energy requirements is ideal. The drawback to this approach is the limited lifespan of the plasma initiating substrate. Generation of a plasma results in ablation of the substrate surface so material is lost over time, thus any detection device has a limited lifetime before maintenance is required. The second LIBS detection scheme examined was the use of a breakdown directly in the sample gas stream. Dielectric thresholds are much greater for a gas as opposed to a solid surface but the benefit of plasma initiation in a gas is there is no finite detector lifetime based on the number of plasmas generated. In addition, the availability of emission over 4π steradians allows for a flexible collection optics configuration. While the characteristics of each technique are important, the detection ability of these configurations is the primary focus for any practical implementation. Before a comparison of hydrogen detection ability was made through experimentation, a preliminary investigation was performed for candidate substrates for surface initiation.

A variety of materials were examined to determine the ideal candidate substrate for surface-enhanced LIBS. All materials considered were metals due to their high surface electron densities and electron mobility. These properties are what allows plasma initiation at lower energies which is the main benefit of surface-initiated LIBS for gas sampling in a field environment. In addition, metals have relatively low ablation rates thus increasing surface lifetime which also is a benefit for practical implementation of LIBS. Six metals were examined as potential LIBS surfaces: aluminum and copper were examined due to their high electrical conductivity, stainless steel and titanium because of their high hardness, and tungsten and molybdenum due to their high melting temperatures

as refractory metals. Experimentation was performed using the LIBS apparatus presented in Figure 3.10 with the collection lens positioned in a manner to generate a breakdown on the surface of the rear flange. Candidate substrate materials were affixed to the rear flange cap with the exception of stainless steel for which the flange cap itself was used as the sample. A pulse energy of 55 mJ/pulse was used to generate a plasma at a rate of 2.5 Hz on each solid. Ambient water vapor in air at a concentration of approximately 1.5% by volume or 1000 ppm was used as the source of hydrogen for detection. Plasma emission was collected using a fixed ICCD gate width of 2 μ s while the delay was varied from 2 to 12 μ s by an increment of 2 μ s to generate six samples for each substrate. The spectral window was centered on the 656.28 nm H_{α} line in order to quantify the hydrogen emission. An examination of the spectra for all materials revealed 4 μ s as the delay that yielded the best ratio of hydrogen emission to the background continuum. Using the spectra at a delay of 4 μ s, a qualitative comparison of the emission spectra was made to select the best substrate.

With a substrate selected, experiments were performed to compare the hydrogen detection ability of gas phase versus substrate-initiated LIBS. A fixed detector delay of 4 μ s and a fixed gate width of 4 μ s were used for these experiments. The two mass flow controllers shown in Figure 3.10 were used to generate the sample gas flow for each experiment. A flow of 43.7 lpm of HEPA filtered industrial grade nitrogen was combined with an ultra-pure hydrogen flow varied from 0 to 16 lpm to generate the range of hydrogen flow concentrations listed in Table 3.9. For each of the concentrations, two or three 50 shot average spectra of the hydrogen emission were collected for the surface-initiated plasma.

Table 3.9 Nitrogen and hydrogen flows used for the LIBS gas phase and substrate-initiated experiments with the corresponding hydrogen concentrations.

N ₂ Flow (lpm)	H ₂ Flow (lpm)	H ₂ Concentration (% by volume)	H ₂ Concentration (mass ppm)
43.7	0.04	0.092	65.432
43.7	0.1	0.229	163.564
43.7	0.2	0.456	327.074
43.7	0.5	1.132	817.285
43.7	1	2.239	1633.234
43.7	2	4.38	3261.142
43.7	4	8.392	6501.084
43.7	8	15.485	12918.185
43.7	16	26.817	25506.867

The focusing lens was then repositioned to achieve a breakdown in the middle of the sample chamber and the pulse energy was increased to 100 mJ/pulse. The same data collection procedure was used to obtain spectra at each concentration with the gas phase plasma. In addition, one 50 shot average blank spectrum corresponding to breakdown in a pure nitrogen flow was collected before and after each data set for each LIBS approach. Using all spectra collected, the response and detection limits for each LIBS format were determined as described in the next section on spectral analysis.

3.2.3 Spectral Analysis for Gas-phase and Surface LIBS

In order to quantify the alpha emission line of hydrogen at each concentration and calculate detection limits, the hydrogen alpha line had to be discriminated from the overall LIBS spectra recorded using the ICCD. The raw emission spectrum included the H_α peak of interest as well as other atomic and molecular peaks, continuum emission, and a direct current (DC) offset associated with the ICCD and analog-to-digital converter (A/D). A sample raw spectrum illustrating these components is given in Figure 3.11.

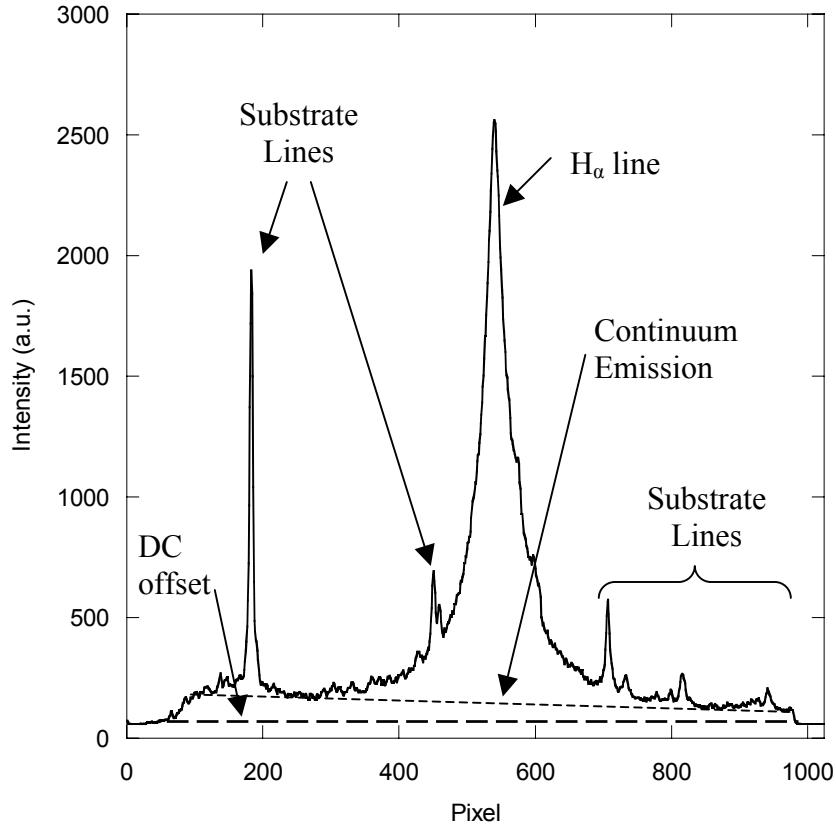


Figure 3.11 A sample raw LIBS emission spectrum from a stainless steel substrate-initiated plasma in 16.62% H₂ in a nitrogen atmosphere. The spectrum shows the H_α peak as well as additional spectral components including atomic peaks, continuum emission and the DC offset associated with the CCD and A/D converter.

As shown in Figure 3.11, the emission spectrum not only contains signals from many sources, as previously stated, but these signals are superimposed on one another making signal separation impossible using only the recorded spectrum. To achieve optimal signal discrimination and quantification for the H_α line in the plasma emission spectrum, the signals from all extraneous sources were first removed. Two blank spectra were recorded for each LIBS experiment. An average blank spectrum was first found from the two measured blank signals. It should be noted that the any attenuation that was performed with neutral density filters at the time of experimentation to prevent ICCD saturation was accounted for at this point. Prior to subtraction of the offset from each

data point, the offset and data point were multiplied by the attenuation factor, the reciprocal of the attenuation, for that particular sample. This negated the effect of neutral density filter changes between the collection of sample spectra thus providing absolute spectra all on the same intensity scale.

To achieve discrimination, the baseline DC offset was first subtracted from the hydrogen emission spectrum and blank spectrum. In order to extract the hydrogen emission for sample spectra, the blank was first scaled to each sample spectrum analyzed. Scaling was required because the absolute intensity of the overall LIBS emission spectrum may vary on a shot to shot basis as discussed below. A metric for the scale of each emission spectrum is the level of the background continuum emission. At low wavelengths in the ultra-violet or low visible range, broadband continuum emission can show a substantial decrease with increasing wavelengths. The H_{α} line occurs at 656.28 nm where broadband continuum emission is low and exhibits only a small decrease with wavelength. Therefore, an approximation of constant continuum emission was made in order to scale the average blank spectrum to each analyte spectrum. Ratios of the continuum for each particular absolute sample spectrum to the continuum of the corresponding absolute average blank were calculated for each data point in two regimes of constant emission in the spectrum where no atomic or molecular peaks were present. An average scale factor was then calculated based on the scale factors found for all pixels in each range. Scaling of the blank was achieved by taking the product of each data point of the raw blank with the average scale factor for the corresponding absolute sample spectrum. This scaled blank could then be used to extract the background signal from the

H_{α} emission line. An example of a scaled blank spectrum with its corresponding hydrogen spectrum is shown in Figure 3.12.

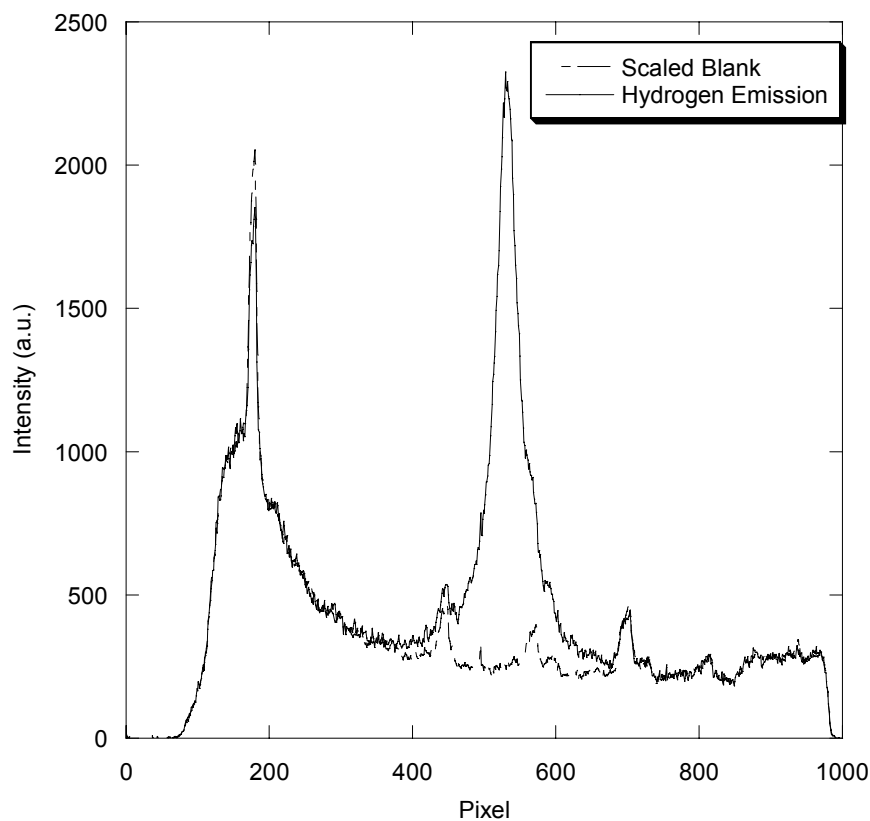


Figure 3.12 Two sample emission spectra showing the absolute analyte emission and the absolute blank emission in the H_{α} region for a stainless-steel substrate initiated plasma. The concentration of the analyte was 16.62% H_2 in a nitrogen background.

Extraction of the hydrogen emission peak was achieved by integrating the full width of the H_{α} peak in each sample spectra and subtracting off the corresponding integrated blank over the same full width of the hydrogen peak. This calculated value is equivalent to the area under the blank subtracted emission peak as shown in Figure 3.13.

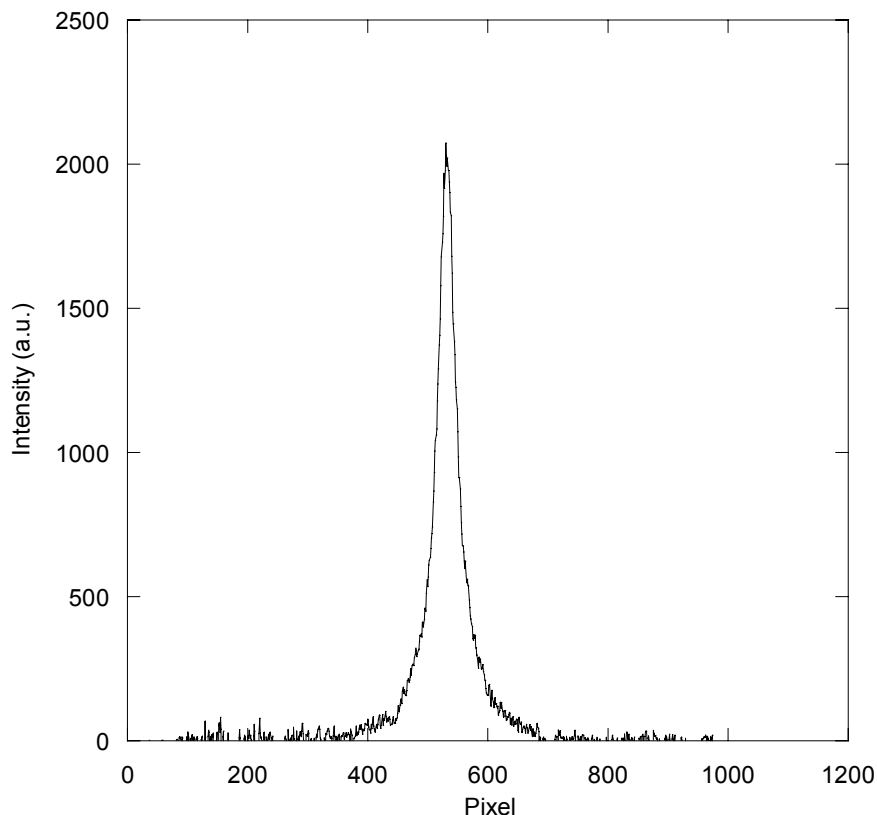


Figure 3.13 Absolute H_{α} peak achieved as a result of blank subtraction. This peak exhibits an integrated area proportional to concentration.

With the hydrogen emission quantized, the response was determined by the peak-to-base (P/B) ratio. This ratio is a commonly used ratio for LIBS analysis because it enhances precision by taking into account the natural fluctuations in plasma emission through scaling to the blank spectrum (Carranza 2002). In addition, any effects of gain, ND filters and detection binning are eliminated by normalizing to the continuum. Calculation of the P/B ratio for all data was achieved by ratioing the absolute integrated hydrogen emission peak to the integrated blank. With the P/B ratios calculated, the response of hydrogen emission to concentration for each LIBS technique was examined.

In order to quantify the detection ability of each LIBS system, a limit of detection was calculated from the response. This limit of detection is similar to the LOD presented

for the Raman experiments in that it represents the lowest concentration that can be detected with statistical significance. The limit of detection (LOD) used for the LIBS experiments is given by Equation 3.4 where m is the slope of the calibration curve at low concentrations and σ_{RMS} is the root-mean-square (RMS) noise.

$$LOD = \frac{3\sigma_{RMS}}{m} \quad \text{Equation 3.4}$$

The σ_{RMS} was first calculated by finding three mean, x_m , intensity values in three constant regions of the spectra recorded at the lowest hydrogen concentration. The difference between each mean and each intensity, x_i , used for its calculation was then found and squared. All squared differences for each group were summed and divided by the number of data points in that group. Finally, the square root was taken of each resulting value to yield that region's RMS noise and all noise values were averaged to yield σ_{RMS} . Equation 3.5 gives the formula for the RMS noise for one spectral region.

$$\sigma_{RMS} = \sqrt{\frac{\sum_{i=0}^N (x_i - x_m)^2}{N}} \quad \text{Equation 3.5}$$

With the RMS noise calculated and the slope of calibration curve known from a linear regression, the LOD was calculated for each sample set response and used to compare gas phase LIBS to substrate-initiated LIBS for hydrogen detection.

A comparison of the free electron number densities for the plasmas observed for gas phase and surface initiated LIBS was made during experimentation to determine the similarities of the plasmas and reinforce the LOD findings. The free electron density for each plasma was determined through measurement of the Stark broadening of the H_α emission line which was assumed to be the dominant broadening mechanism present for

the hydrogen line. As reported by Griem, the free electron density of the plasma is related to the full width at half maximum (FWHM) intensity by Equation 3.6 where $\Delta\lambda_{fwhm}$ is the FWHM of the H_α line in wavelength, $\alpha_{1/2}$ is the fractional half-width of the reduced Stark profile, e is the electron charge (4.8032×10^{-10} esu), and n_e is the free electron number density (Hohreiter 2004).

$$\Delta\lambda_{fwhm} = 2\alpha_{1/2}(2\pi)\left(\frac{4}{15}\right)^{2/3} e(n_e)^{2/3} \quad \text{Equation 3.6}$$

The results of all experimentation and calculations are presented in Chapter 5.

3.2.4 Experimental Apparatus for Surface Degradation Studies

A second laboratory LIBS setup, similar to the first setup, was constructed for the substrate degradation studies. This setup is shown in Figure 3.14. A comprehensive listing of all included components is given in Table 3.10. Another Q-switched, 1064 nm pulsed Nd:YAG laser with an 8 ns pulse width operating at 5 Hz was used for this experiment. The two pulse energies used were 60 mJ/pulse and 110 mJ/pulse corresponding to voltage settings for the laser of 6.2 kV and 8.3 kV, respectively. These pulse energies, as measured with a Scientech Model AC5001 Calorimeter at the exit of the laser head, were used to achieve pulse energies of 55 mJ/pulse and 100 mJ/pulse for plasma generation after losses associated with optical components thus maintaining pulse energies from the previous LIBS experimentation. The laser was oriented perpendicular to the sampling axis as shown in Figure 3.9 with a 45° dichroic mirror used to turn the laser. As in the other setup, the laser beam was passed through an iris aperture to ensure a concentric beam profile prior to focusing. A focusing lens with a 300 mm focal length was used for plasma generation. Before entering the sample chamber, the laser beam was passed through a 0.5 inch hole in the center of the 75 mm square collection mirror while

being focused.

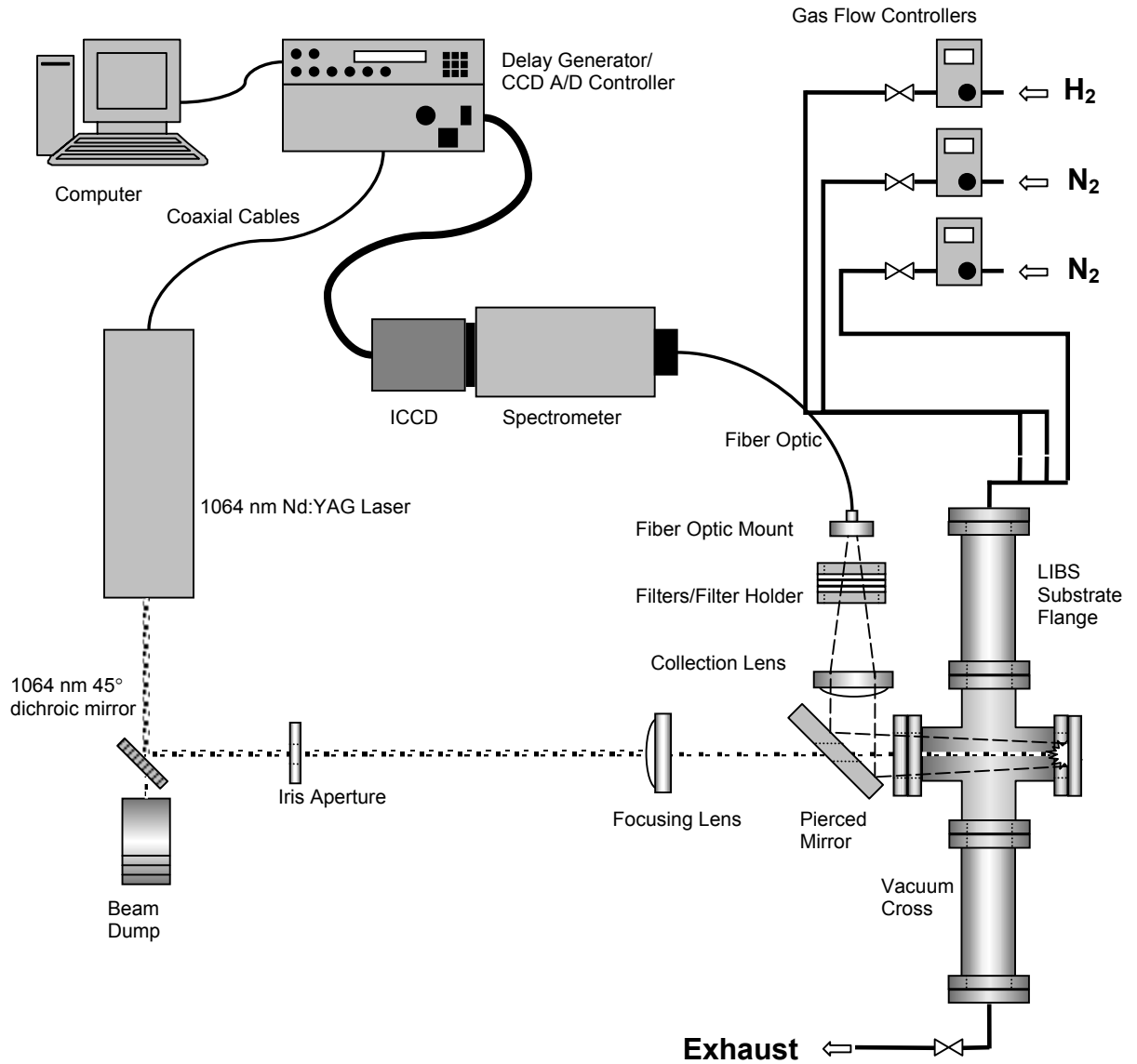


Figure 3.14 Laboratory LIBS configuration used to study the effect of surface degradation on hydrogen detection limits in response to a substrate-initiated plasma.

Table 3.10 Listing of all optical components with specifications for the laboratory LIBS apparatus used to study the effect of surface degradation in substrate LIBS.

Component	Specifications	Vendor	Part No.	Quantity
Laser	1064 nm, 5 Hz, 110 mJ/pulse (8.3 setting), 60 mJ/pulse (6.2 setting) [100 and 55 mJ desired for plasma but extra energy used to account for optic losses)	Big Sky Laser Technologies Inc.	Model: 230A8000 S/N1	1
Laser Turning Mirror	45 degree mirror, 1064 nm A/R coating, 2 inch diameter	CVI Laser Coporation	Y1-2037-45UNP	1
Focusing Lens*	Plano-convex, 300 mm focal length, 2" diameter	CVI Laser Coporation	PLCX-50.8-154.5-UV-1064	1
Square Pierced Mirror	75 mmx75mmx1mm, center pierced-0.5 inch +-0.2" diameter	Rolyn Optics	60.245	1
Gas Chamber	2" O.D., 304 stainless steel 4-way gas cell, solid back flange, UV grade quartz front window, copper gaskets	Huntington Labs		1
Collection Lens	100 mm focal length	CVI Laser Coporation	PLCX-50.8-51.5-UV-1064	1
Neutral Density Filters	0.3 attenuation rating used	Newport		A/R
Flow Controller	0.02-1 L/min flowrate; used for hydrogen	Alicat Scientific		1
Flow Controller	1-10 L/min flowrate; used for nitrogen	Alicat Scientific		2
Fiber Optic	3 foot, high optical grade, 17 fiber bundle, 1.5 mm diameter			1
Spectrometer	0.275 Meter Triple Grating Spectrometer	Action Research Corporation	SpectraPro-275, S/n 275995S	1
ICCD	Intensified CCD, 200 row chip	Princeton Instruments	Model: 1024MLDS-E/1, N119302	1
Software	Metal Emissions Labview Program		Custom	1

The same sample chamber was again used with a front UV-grade quartz window, a solid stainless steel rear flange and two gas input flanges. One gas flange had an attached fitting tree allowing the injection of gaseous analytes from three separate mass flow controllers plumbed to gas cylinders while the opposite gas flange was again used for exhausting of gases. Three mass flow controllers were used for this experiment due to unavailability of the previously used controllers and to achieve the desired flow rates. A picture of the mass flow controllers is shown in Figure 3.15.



Figure 3.15 Three mass flow controllers used for control of sample concentrations during the surface degradation studies.

Plasma emission was collected through the front gas cell window by means of the pierced collection mirror oriented at 45° to the front window. The rest of the collection optics and instrumentation were the same as the setup shown in Figure 3.10. A picture of the collection optics for this experiment is shown in Figure 3.16.



Figure 3.16 Collection optics used for collection of plasma emission during the substrate degradation experiments.

. Figure 3.17 shows a picture of the entire second LIBS laboratory system in the configuration shown in Figure 3.14.

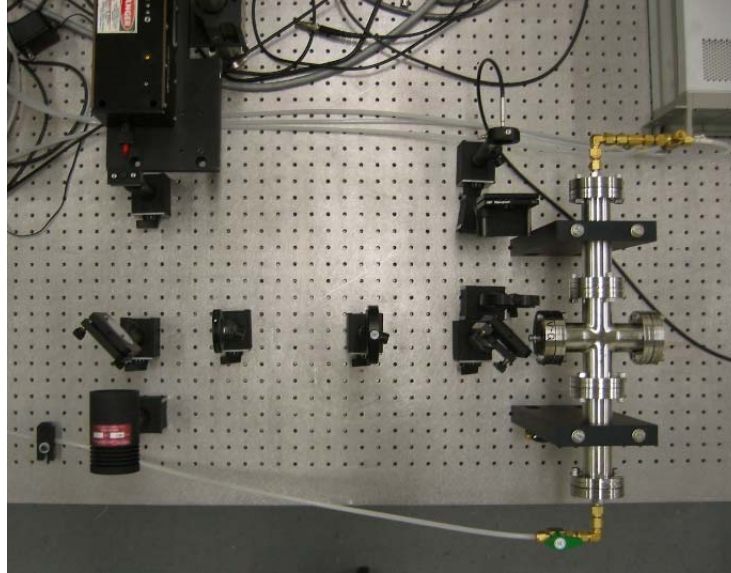


Figure 3.17 Photograph of the LIBS laboratory system used for the investigation of substrate degradation effects on hydrogen detection ability.

3.2.5 Surface Degradation Investigation

With a substrate-enhanced LIBS detection scheme, concern must be taken with the effect of the plasma on the substrate. The free electron density of the surface is beneficial in that it allows a lower threshold for breakdown and subsequently cascade ionization and plasma formation. As expected, the plasma initiated with the aid of the electron density of the surface not only entrains gaseous species from above the surface but also entrains a portion of the substrate molecules. Therefore, surface degradation is observed due to the presence of the plasma. In order for a LIBS based hydrogen detection scheme to be practical and quantifiable, the hydrogen signal at a particular concentration must not exhibit transient fluctuations. While most of the experimental parameters governing transient plasma initiation such as pulse energy, repetition rate, and focal length have been fixed, the substrate surface profile cannot be maintained due the degradation by the plasma. Therefore, this transient change in the surface needed to be examined to estimate any possible effects on detection accuracy and precision.

In order to determine the substrate lifetime for which consistent signals can be obtained, a set of experiments were performed using the experimental LIBS apparatus presented in Figure 3.14. Stainless steel was used as the substrate for surface enhanced breakdown as in the previous LIBS studies. As before, the flange cap surface was placed at the focal point of the plano-convex laser focusing lens to achieve the highest energy density for the initiation of the breakdown. A constant hydrogen flow concentration of 16.6% by volume was used for experimentation.

To examine substrate degradation, three experiments were performed. In the first experiment, average spectra of 100 shots were collected showing the H_{α} line at a 5 Hz repetition rate for one hour resulting in the collection of 180 hydrogen emission spectra. Two more experiments were performed after analysis of the first experiment to study longer substrate degradation. For the two additional experiments, average spectra were collected for 2.5 hours to yield 450 average hydrogen emission spectra. Analysis of all average spectra was carried out using a peak-to-base ratio similar to the P/B used in the LIBS comparison experiments. The only difference in the calculation of the P/B ratio from earlier values was that, due to the large number of spectra, scaled blanks were not used for signal extraction and ratioing. Rather, an average baseline value was calculated in the same constant area of each spectrum where no emission peaks were present. The average baseline intensity was then multiplied by the peak width to achieve the equivalent of the integrated blank. After calculation of P/B ratios with the baseline procedure, the response in hydrogen emission was examined as a function of the total number of shots. Finally, to help understand the response behavior observed and to illustrate the substrate degradation, scanning electron microscopy was used record a

magnified image of all sample craters. The results of these experiments are also illustrated in Chapter 5.

CHAPTER 4

RESULTS AND DISCUSSION OF HYDROGEN DETECTION BY RAMAN BACKSCATTERING

This chapter presents the results of all hydrogen detection experiments using spontaneous Raman backscattering. Preliminary investigations into the use of this technique for hydrogen detection are first presented. These results are followed by studies of optics configuration and excitation source effects on detection limits. Comments on a field detection device are presented although testing of this system was not realized in this work.

4.1 Preliminary Remote Hydrogen Detection Study

An initial experiment was performed to examine the ability to detect hydrogen remotely using the Raman technique as described in Chapter 3. The sample gas cell was positioned at 6.58 m from the collection optics and backscatter signals were collected using the PMT. As stated before, concentrations higher than the desired detection regime were used to yield an ample scattering signal for this initial investigation. Prior to the collection of the scattering signal, PMT linearity and spectrometer calibration were examined.

The Action spectrometer used for all Raman measurements allows the user to select a desired wavelength and adjusts the grating automatically to illuminate the output slit based on the diffraction angle for that wavelength. While precise, the accuracy of the grating calibration had to be examined prior to experimentation to ensure the actual location of the 416.01 nm Raman line corresponding to a 4156 cm^{-1} shift at an incident

frequency of 355 nm. Using the gas cell pressurized at 10, 20, and 30 psig of pure hydrogen, the PMT signals corresponding to ten wavelengths from 415.91 nm to 416.91 nm were examined. Figures 4.1-4.3 show the PMT signal measured at each wavelength for cell pressures of 10, 20, and 30 psig, respectively. The second peak corresponds to the scattering signal for hydrogen as the first peak is a result of fluorescence or stray, scattered light present in the spectrometer. The presence of this peak will be discussed in more detail when discussing the concentration response for the preliminary investigation. For all three hydrogen concentrations examined, the most intense scattering peak was observed at 415.91 nm as shown in Figure 4.1-4.3 by the bold square-traced signal.

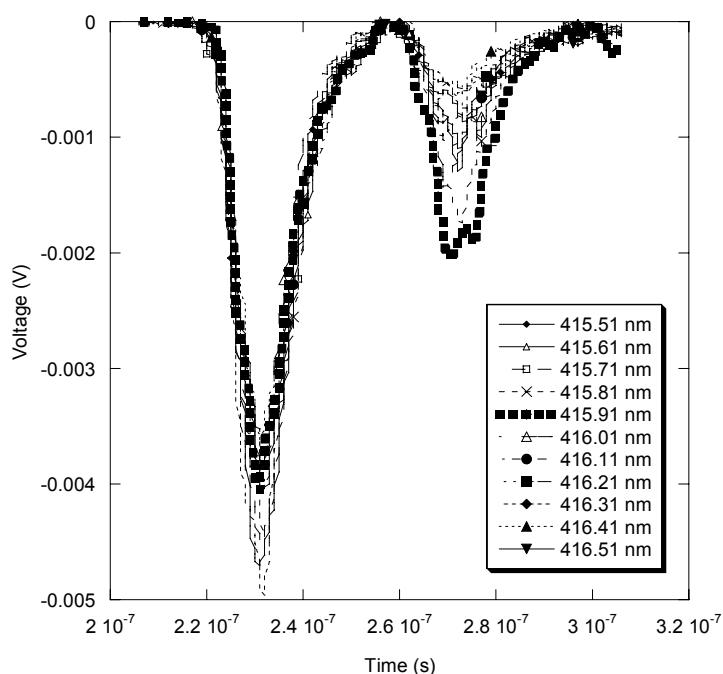


Figure 4.1 PMT scattering signals recorded for ten wavelengths around the Raman Stokes line for hydrogen at 10 psig in the sample cell. Signals are negative due to a negative PMT operating voltage of -782 V.

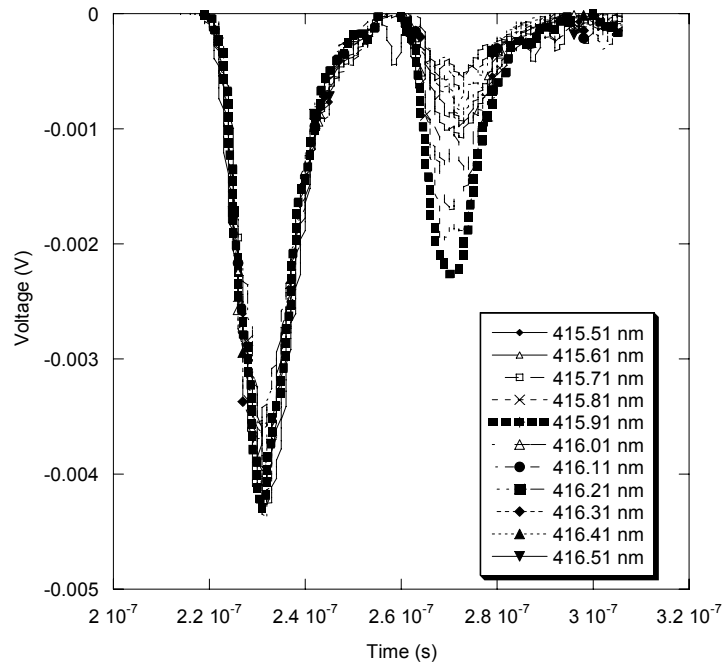


Figure 4.2 PMT scattering signals recorded for ten wavelengths around the Raman Stokes line for hydrogen at 20 psig in the sample cell. Signals are negative due to a negative PMT operating voltage of -782 V.

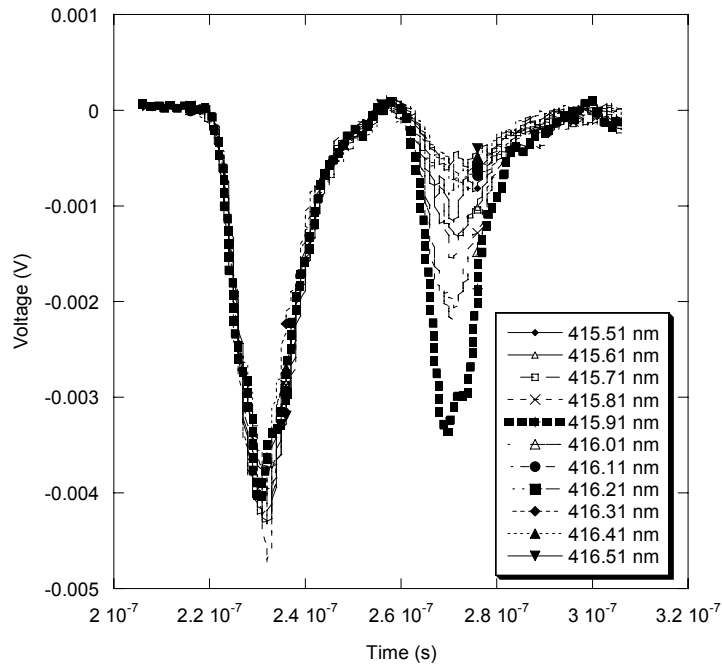


Figure 4.3 PMT scattering signals recorded for ten wavelengths around the Raman Stokes line for hydrogen at 30 psig in the sample cell. Signals are negative due to a negative PMT operating voltage of -782 V.

Also, while the purpose of this first set of measurements was not to examine signal response to concentration, an increase in the scattering signal was observed with higher concentration as well as possible increased sensitivity as shown above.

With the calibrated location of the Raman line identified for hydrogen, three samples were taken at each experimental concentration listed in Table 3.2. Sample PMT signals showing the hydrogen peak for a concentration of 0.126 mol/L at a spectrometer wavelength of 415.91 nm and the off-peak signal at 413.91 nm are shown in Figure 4.4.

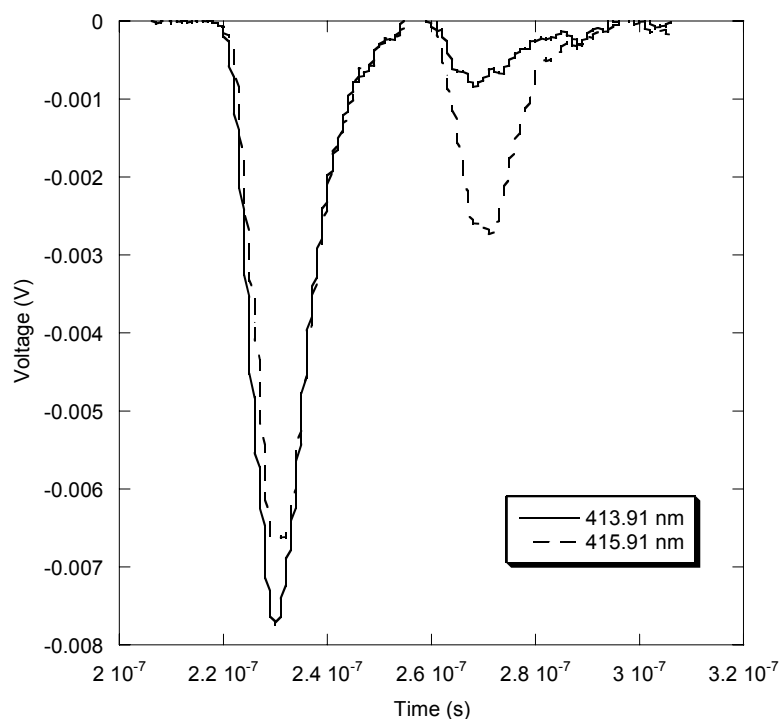


Figure 4.4 PMT signals showing scattering response on the Raman line at 415.91 nm and off the Raman line at 413.91 nm.

As noted before and shown in Figure 4.4, the signal for the preliminary measurements showed two peaks separated by approximately 0.04 μs . The first peak is a relatively constant peak that was present both on and off the Raman line in all recorded signals while the second peak was observed to minimize in offline measurements and grow in proportion to sample hydrogen concentration. For this reason, the second peak

was identified as the hydrogen Raman scattering signal. The use of an ultra-violet excitation source results in noise generated by broadband fluorescence in addition to common forms of background noise such as stray light, shot noise, and signal noise. Visible fluorescence from the mirrors and beam dump in the blue region of visible spectrum was observed during experimentation. If a calculation is made based on the 6.58 m separation distance between the collection mirror and the center of the gas cell using the speed of light as 2.997×10^8 m/s, the time it would take for radiation to travel from the mirror to the cell and back is approximately 0.04 μ s. Therefore, the fluorescence/reflection from the mirror as the laser passes through the pierced hole is observed as the first signal peak, and the Raman scattered light is observed as the second signal peak after the laser has propagated to the cell and the scattered light has backscattered to the collection mirror. Figure 4.4 also shows that significant background noise is present in the offline measurement at 413.91 nm. This noise which most likely resulted from one of the common forms of noise mentioned above or fluorescence of the beam dump behind the gas cell decreases the signal-to-noise ratio. For the high concentrations used in this preliminary investigation, this noise did not limit detection ability but this presented a concern for follow up detection limit studies presented later in the chapter.

With the scattering peak identified, signal noise was subtracted in the method presented in Chapter 3. Figure 4.5 shows the change in absolute PMT signal in response to decreasing hydrogen concentrations at the Stokes line for hydrogen in one preliminary study. The absolute signals have been inverted for clarity.

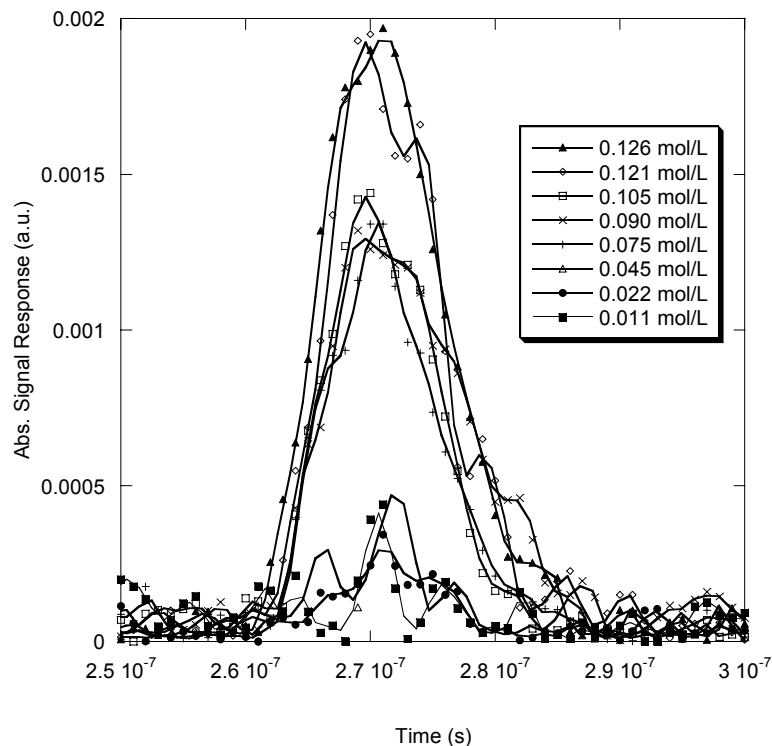


Figure 4.5 Absolute scattering response for decreasing hydrogen concentrations in one preliminary hydrogen detection experiment.

The response of the scattering signal to decreasing hydrogen concentrations was a proportional decrease in intensity. This decrease was expected based on the spontaneous Raman scattering theory presented in Chapter 2. In order to quantify these preliminary measurements and determine if a linear relationship existed between scattering signal and hydrogen concentration, the absolute response peaks were discretely integrated and the values for each concentration were averaged across all three trials. The averaged Raman scattering signal for the preliminary experiments is shown as a function of hydrogen concentration in Figure 4.6 with error bars representing one standard deviation.

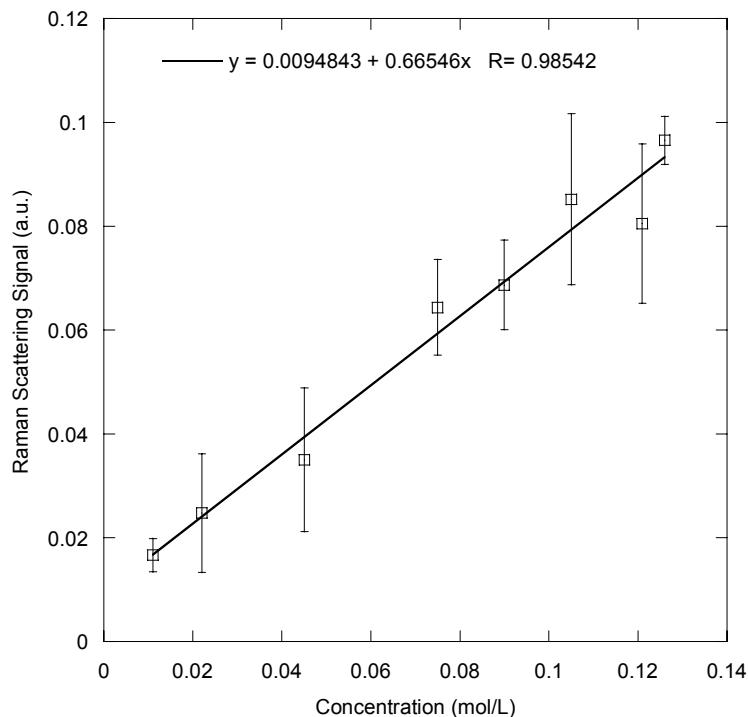


Figure 4.6 Average Raman scattering response for preliminary hydrogen detection at 6.58m as a function of hydrogen concentration.

The averaged Raman scattering signal shows that a linear relationship ($R=0.985$) did exist between scattering signal intensity and hydrogen concentration for the concentration range tested. This is important because it not only demonstrated linearity of the Stokes scattering signal, but that remote hydrogen detection is achievable at a significant distance and the detection system can be calibrated. Large standard deviations, as shown by the error bars, between the samples at most scattering responses can be attributed to fluorescence and other noise present in the offline measurements as shown by the peak in the 413.91 nm line in Figure 4.4, as well as uncertainties in the exact hydrogen concentration. The presence of this significant noise affects the extraction of the absolute Raman signal, thus large fluctuations in noise greatly affect the detection response.

While validating the ability to detect hydrogen concentrations, the lowest concentration tested in these preliminary experiments corresponded to 25% hydrogen by

volume, well above the lower flammability limit of 4% for hydrogen. It is for this reason that detection limits were not calculated for this data. In addition, significant background noise was observed due to fluorescence and stray light with effects that have been previously discussed. The response observed for pure hydrogen at 30 psig, approximately two times atmospheric pressure, as shown in Figure 4.4 was still low and within the same order of magnitude as the offline noise. An increase in the signal-to-noise ratio and the determination of detection limits at concentrations below the flammability limit were goals for the next segment of experimentation.

4.2 Detection Limit Determination

The purpose of the next set of experiments conducted was to examine minimum detection ability by calculation of the limit of detection for concentrations ranging across the lower flammability limit. As described in Chapter 3, the scattering signals for hydrogen concentrations ranging from 0.78% to 100% by volume were examined at 355 nm and 532 nm excitation wavelengths. The 532 nm excitation wavelength was added to the study due to the fluorescence and associated noise seen with 355 nm ultra-violet excitation. The gas cell was positioned closer to the detection optics at a separation distance of 2.26 m to aid in low concentration detection for this initial LOD study.

Scattering signals were recorded and analyzed as described in Chapter 3 with the only difference in analysis from the preliminary experiment being the collection and subtraction of a dark noise signal prior to all response calculations. Figure 4.7 shows the Raman scattering signal and one offline measurement for hydrogen at 100% by volume at atmospheric pressure with an excitation energy of 355 nm.

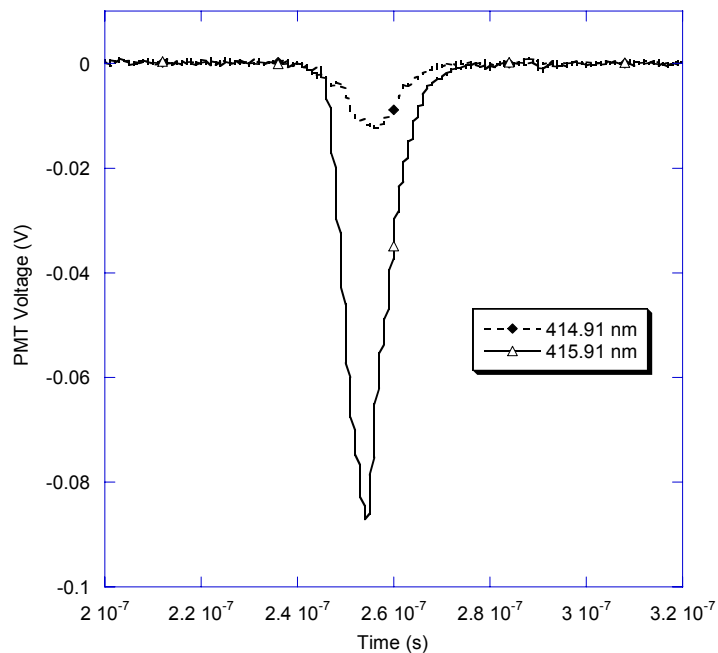


Figure 4.7 Raman scattering signal and one offline measurement for 100% hydrogen by volume at atmospheric pressure excited by 355 nm incident radiation.

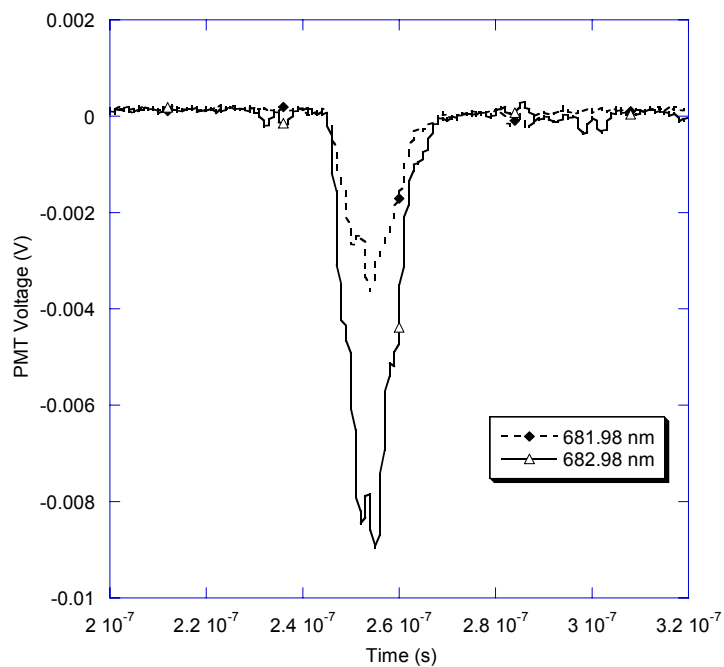


Figure 4.8 Raman scattering signal and one offline measurement for 100% hydrogen by volume at atmospheric pressure excited by 532 nm incident radiation.

Figure 4.8 shows the same information but for an excitation energy of 532 nm. Both signals are corrected for the experimental attenuation used to maintain signal linearity. The signal for 100% hydrogen by volume at atmospheric pressure with 355 nm excitation exhibited a high intensity in comparison to the background noise shown by the peak in the offline signal. A comparison of signal to noise for the same sample concentration with 532 nm excitation showed a scattering signal the same order of magnitude as the offline noise signal. While the use of 532 nm radiation eliminated fluorescence by moving out of the ultra-violet range, the fourth order dependence of Raman scattering intensity on incident wavelength resulted in the observed significant decrease in signal intensity. Detection at 4% or below by volume was not expected for 532 nm scattering after visualization of the signal shown in Figure 4.8. It was also noted that at both wavelengths, an appreciable offline background signal was still observed.

All offline signals were averaged and the baseline subtracted to achieve an average optical noise signal. The baseline was also subtracted from the Raman line signal and finally an absolute Raman line signal was achieved by subtraction of the average optical noise. Figure 4.9 and Figure 4.10 show the absolute scattering signal at 100% hydrogen by volume as well as the average optical noise for incident wavelengths of 355 nm and 532 nm respectively. Examination of the absolute scattering signals for 100% hydrogen by volume in comparison to the average offline noise shows that for 355 nm excitation, detection of the Raman scattered light could be achieved above the noise limit. With 532 nm excitation, the signal for 100% hydrogen by volume was comparable to the optical noise intensity. This confirmed the observations and predications from the raw sample signals shown in Figure 4.7 and Figure 4.8.

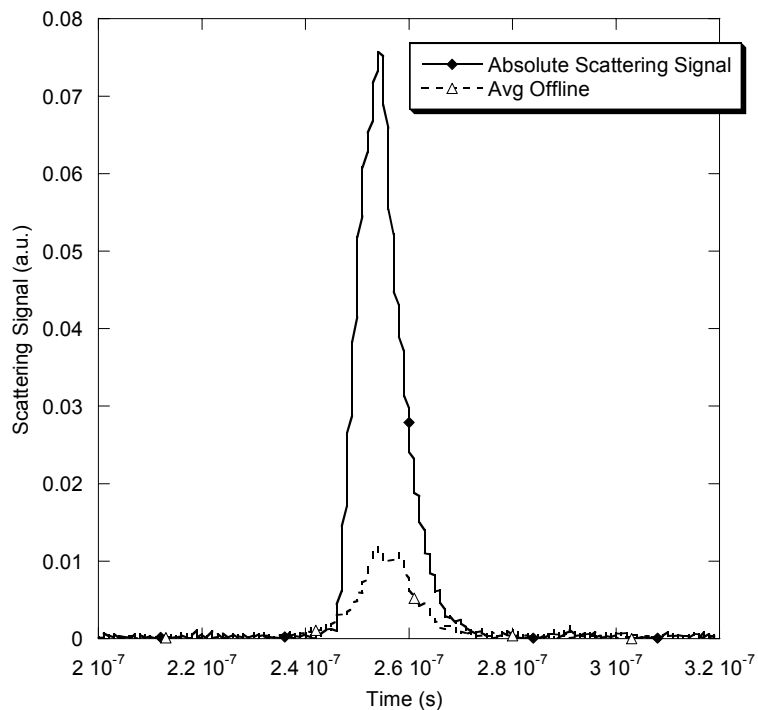


Figure 4.9 Absolute Raman scattering signal and offline noise signal for excitation of the 100% by volume hydrogen sample with 355 nm incident radiation.

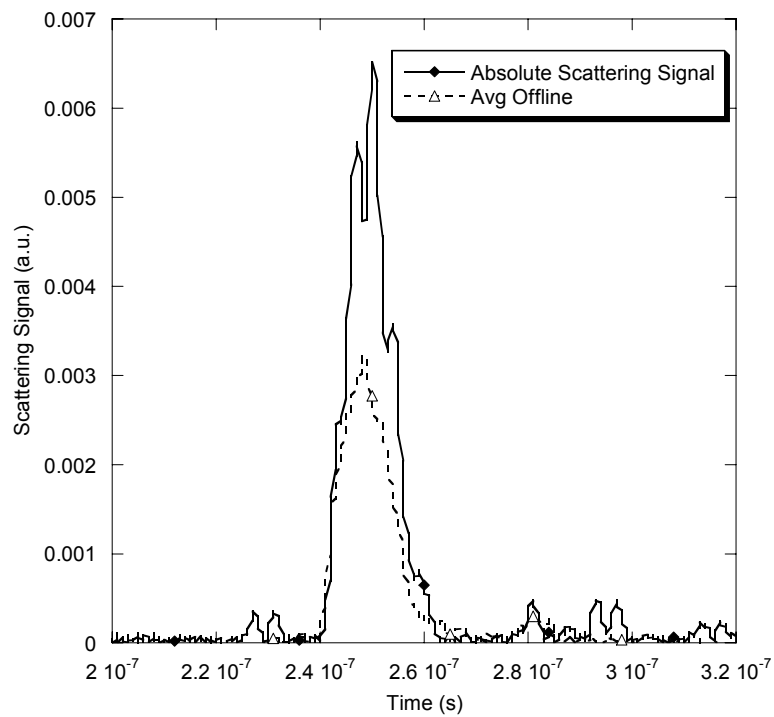


Figure 4.10 Absolute Raman scattering signal and offline signal for excitation of the 100% by volume hydrogen sample with 532 nm incident radiation.

While it was shown that 355 nm excitation yielded a significantly more intense scattering signal than with the 532 nm excitation, both absolute measurements were still on the same order of magnitude as the offline noise at 100% hydrogen by volume.

Sensitive detection at or below the flammability limit of 4% by volume was the goal of experimentation. Figure 4.11 and Figure 4.12 also show the absolute scattering signal and average offline signal for 355 nm and 532 nm excitation but at a concentration of 3.125% hydrogen by volume in a nitrogen background.

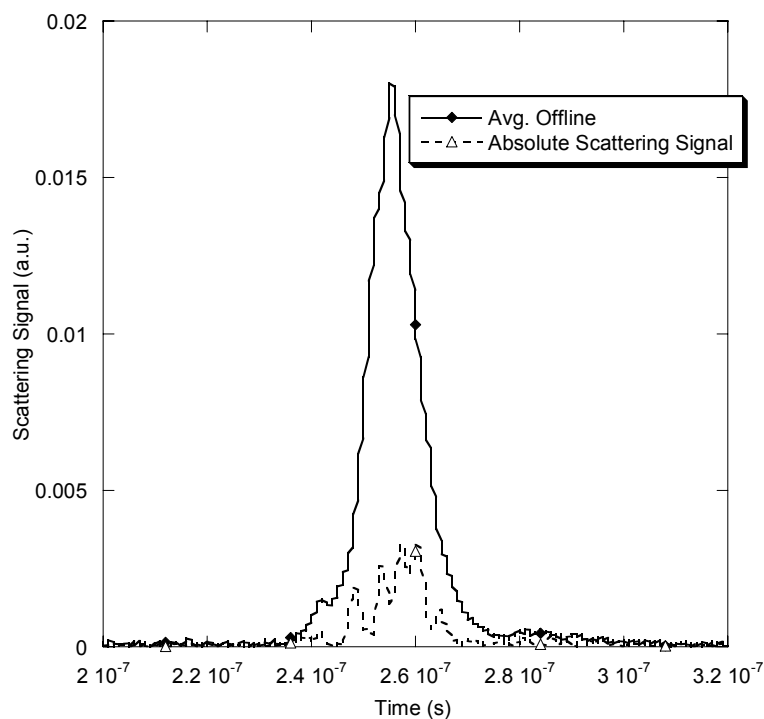


Figure 4.11 Absolute Raman scattering signal and offline signal for excitation of the 3.125% by volume hydrogen sample with 355 nm incident radiation.

Observation of the scattering signal at 3.125% by volume illustrates an interesting trend in signal-to-noise that was observed during these initial detection limit studies. At higher concentrations, the scattering SNR was much greater for 355 nm than for 532 nm signals. Although, at lower concentrations such as 3.125% by volume, the effect of

fluorescence resulted in more significant offline noise than seen for the 532 nm signals offsetting the scattering intensity gain at 355 nm.

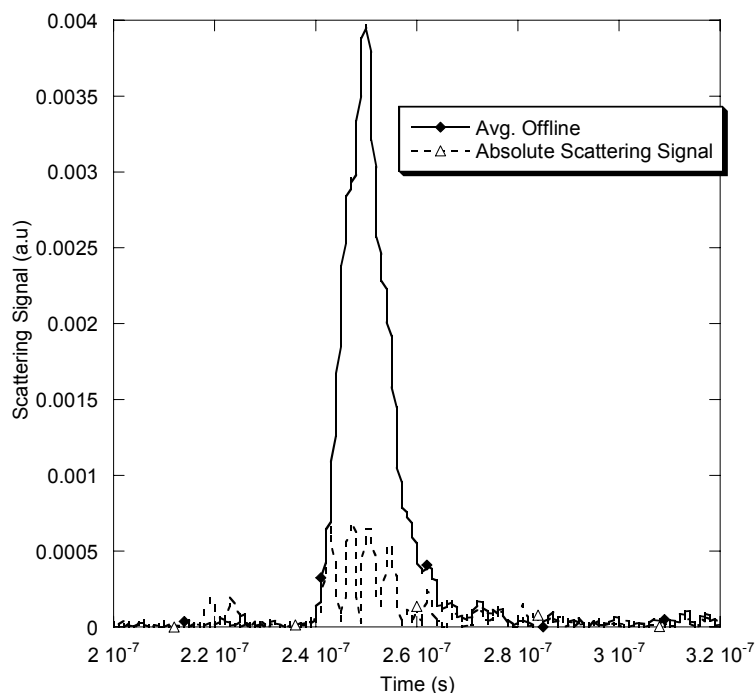


Figure 4.12 Absolute Raman scattering signal and offline signal for excitation of the 3.125% by volume hydrogen sample with 532 nm incident radiation.

The result was comparable scattering responses between the excitation wavelengths at low concentrations with 355 nm yielding only slightly higher response due to signal peak width. The average scattering responses for both 355 nm excitation and 532 nm excitation are given in Figure 4.13 while Figure 4.14 gives an enlarged section of the scattering response plot for concentrations below 25% by volume. The two plots of scattering response show a linear relationship between scattering signal and hydrogen concentration with the response at 355 nm exhibiting higher sensitivity to changes in concentration in comparison to the scattering response for 532 nm incident radiation.

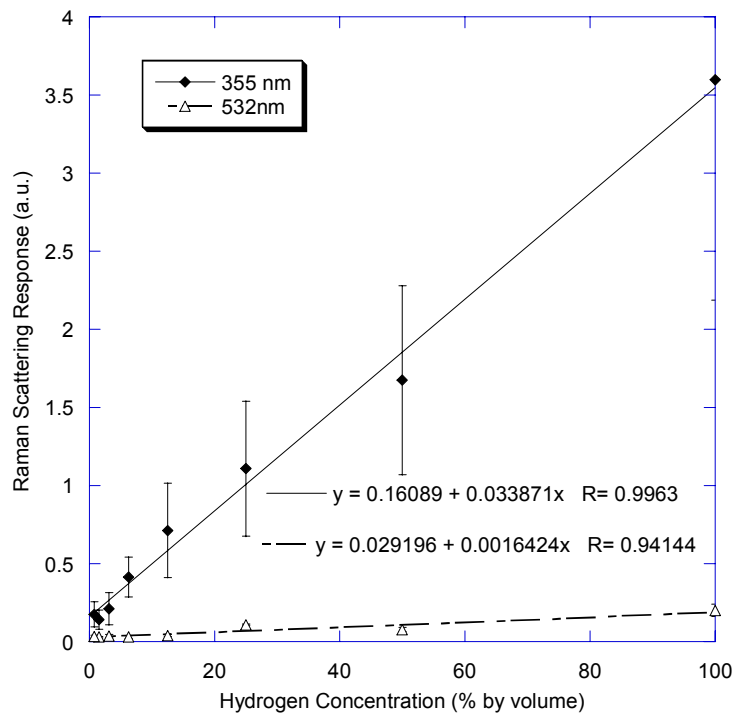


Figure 4.13 Raman scattering response to hydrogen concentration for two excitation wavelengths.

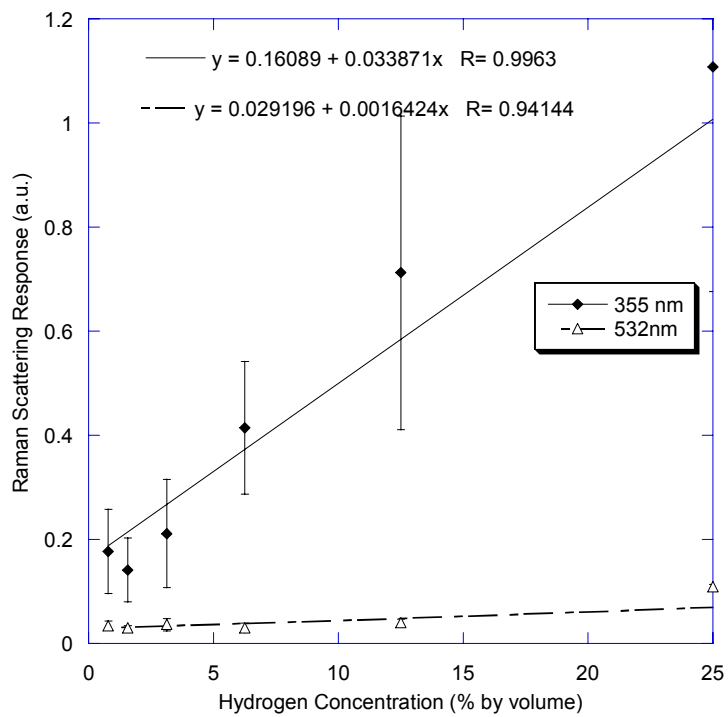


Figure 4.14 Enlarged section of Figure 4.13 to show Raman scattering response to hydrogen concentration for two excitation wavelengths below a hydrogen concentration of 25% by volume.

The 532 nm signal exhibited almost no sensitivity as shown by the horizontal linear regression in Figure 4.13. As with the response in the preliminary investigations, large deviations in scattering signal due to fluorescence were observed at 355 nm, as shown by the error bars for the response. A visual examination of the response plots shows that below 5% hydrogen by volume, scattering signals leveled off and began to fluctuate indicating the signal had reached the level of background noise. This was confirmed by calculation of the limit of detection for each response using the linear regressions shown on the response plots and the standard deviation of the signal noise. A limit of detection of 7.16% hydrogen by volume or 2.93 $\mu\text{mol/L}$ was calculated for the response at 355 nm. For 532 nm incident radiation, a detection limit of 16.04% by volume or 6.56 $\mu\text{mol/L}$ was calculated. These limits of detection give the lowest concentration that can be detected within statistical significance. While the 355 nm response yielded a detection limit that was half that for the 532 nm response, both experiments failed to achieve detection below the 4% flammability limit of hydrogen. As noted throughout the results to this point, significant offline optical noise was seen in all detection measurements. A 2" collection mirror and lens were used to collect the backscattered Raman shifted photons in all experiments. In order to achieve the desired level of detection, lens configuration as well as pulse energy were addressed in conjunction with excitation wavelength with the goal of reducing limits of detection.

4.3 Optical Configuration Effects on Detection Limit

The inability to achieve sensitive detection below the flammability limit of hydrogen up to this point in experimentation was attributed to background optical noise and low collection efficiency of backscattered Raman photons. A set of experiments was conducted to determine the effect of changes in optical configuration on detection limits

for hydrogen at both excitation wavelengths as described in Chapter 3. The parameters varied for each configuration were excitation wavelength, pulse energy and collection lens diameter. In addition, multiple high-pass filters were used for these experiments to further reduce noise due to reflected and scattered light at the incident frequency and broadband fluorescence. The collection mirror was increased in size to a 100 mm, or approximately 4 inch, square pierced mirror for all experiments. The scattering responses achieved and associated detection limits are presented below. Table 4.1 reiterates the configurations examined and lists the corresponding figure number for the figure depicting the scattering response for that configuration.

Table 4.1 Optical configurations examined and figure number for the scattering response.

Wavelength (nm)	Pulse Energy (mJ/pulse)	Collection Lens Diameter (in)	Scattering Response Figure
355	125	2	Figure 4.15
355	250	2	Figure 4.17
355	125	4	Figure 4.19
355	250	4	Figure 4.21
532	125	4	Figure 4.23
532	250	4	Figure. 4.24

The first configuration examined used an excitation wavelength of 355 nm, a pulse energy of 125 mJ/pulse and a collection lens diameter of 2 inches. The scattering response to decreasing hydrogen concentration for this configuration is shown in Figure 4.15. This configuration was similar to the optical configuration used in the initial detection limit study except the pulse energy was reduced to 125 mJ/pulse. Figure 4.15 shows that even with a reduced pulse energy, a linear scattering response ($R=0.994$) was still achieved at 355 nm. Using the linear regression over the entire concentration range, the limit of detection was calculated to be 3.12% by volume.

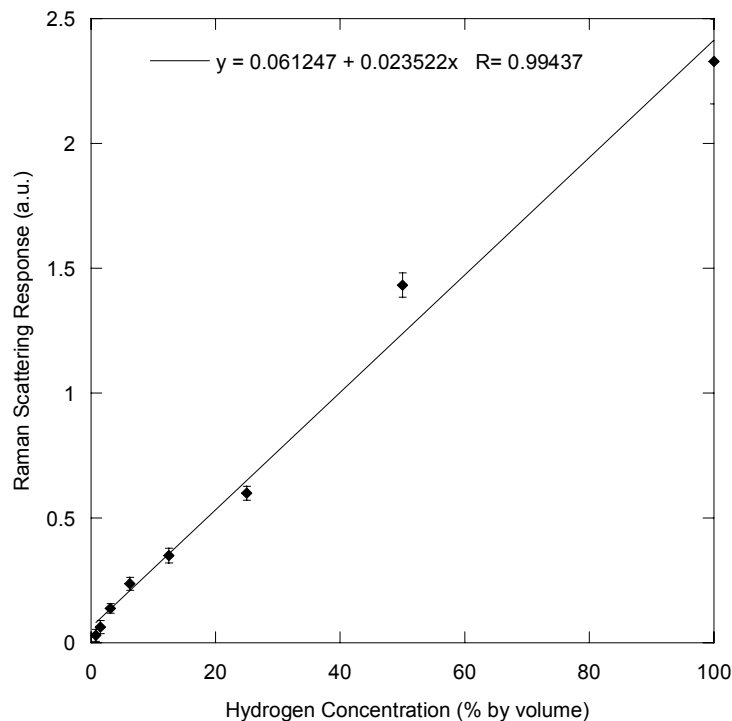


Figure 4.15 Scattering response of hydrogen at an incident wavelength of 355 nm, a pulse energy of 125 mJ/pulse, and collection lens diameter of 2”.

While below the flammability limit, this calculated LOD is not accurate due to the regression falling outside the standard deviation of several of the data points as shown in Figure 4.15. To achieve a more accurate measure of the detection limit, another regression ($R=0.995$) was performed on concentrations below 25%. Figure 4.16 shows an enlarged view of the scattering response for these concentrations along with the second regression. With only the scattering response below 25% by volume considered, the detection limit was found to be 3.22% by volume or 1.32 $\mu\text{mol/L}$. This result was encouraging since it was the first accurate detection limit achieved below the flammability limit for hydrogen. While the same collection lens size of 2 inches and a reduced pulse energy were used in comparison to previous experiments, the use of additional high pass filters greatly reduced the noise thus increasing signal linearity,

decreasing the limit of detection and reducing signal variation as shown by the error bars in Figure 4.15.

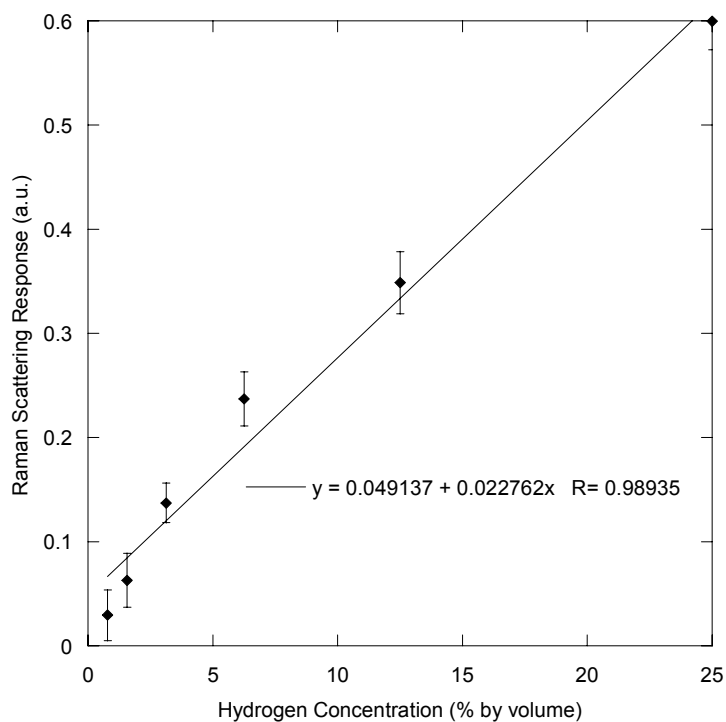


Figure 4.16 Scattering response of hydrogen at an incident wavelength of 355 nm, a pulse energy of 125 mJ/pulse, and a collection lens diameter of 2" for concentrations below 25% by volume.

The second configuration examined increased the pulse energy to 250 mJ/pulse. This experiment was almost an exact repeat of previous detection limits studies in Section 4.2 which used a pulse energy of 244 mJ/pulse at 2.26 m. As expected, a linear scattering response ($R=0.999$) was achieved as shown in Figure 4.17. The significant difference between this measurement and the initial detection limit study of Section 4.2 was again the presence of two additional high pass filters. As a result, the detection limit was expected to be lower due to decreased offline noise. Figure 4.18 shows the scattering response along with a linear regression ($R=0.999$) for less than 25% hydrogen by volume.

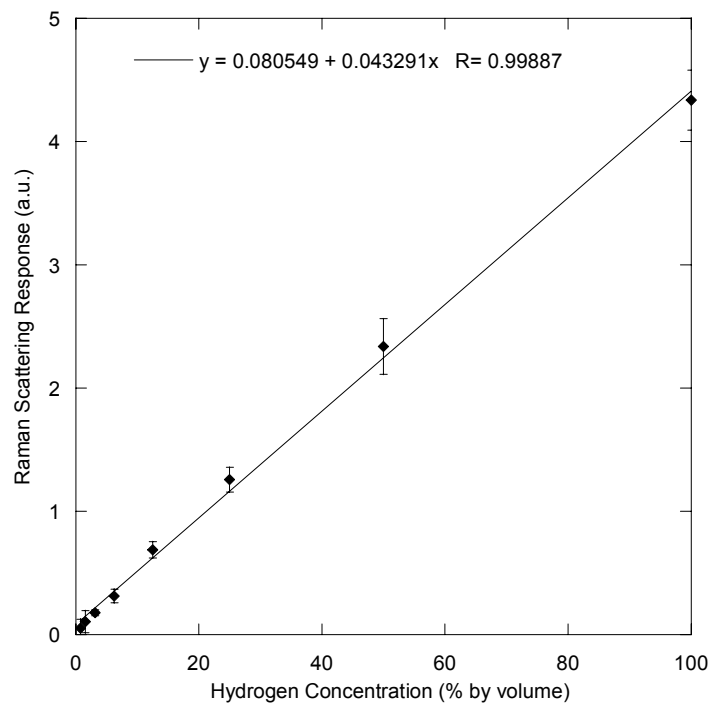


Figure 4.17 Scattering response of hydrogen at an incident wavelength of 355 nm, a pulse energy of 250 mJ/pulse, and collection lens diameter of 2".

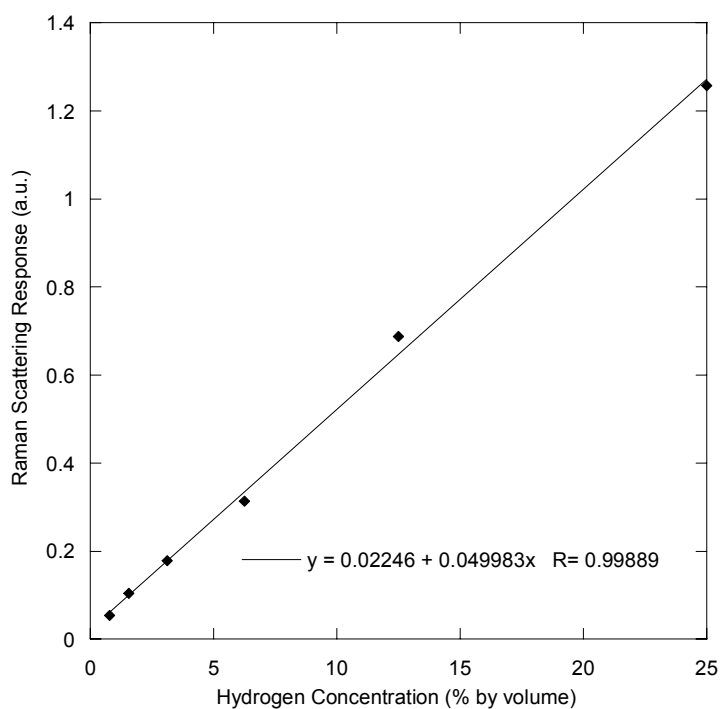


Figure 4.18 Scattering response of hydrogen at an incident wavelength of 355 nm, a pulse energy of 250 mJ/pulse, and collection lens diameter of 2" for concentrations below 25% by volume.

The detection limit found for the response at less than a 25% by volume hydrogen concentration was 4.28% by volume or 1.75 $\mu\text{mol/L}$. This limit, while less than the limit of 7.16% achieved in Section 4.2, was greater than the limit achieved at 125 mJ/pulse energy. This result was not expected. The explanation for this result was unknown but it is believed that collection efficiency with the 2 inch lens was low enough to allow background noise to significantly influence the detection limit thus fluctuation in noise resulted in the unexpected detection limit.

For the third configuration, an excitation wavelength of 355 nm was again used but the pulse energy was returned to 125 mJ/pulse and a 4 inch collection lens was used to increase collection efficiency. The scattering response achieved for this configuration is shown in Figure 4.19

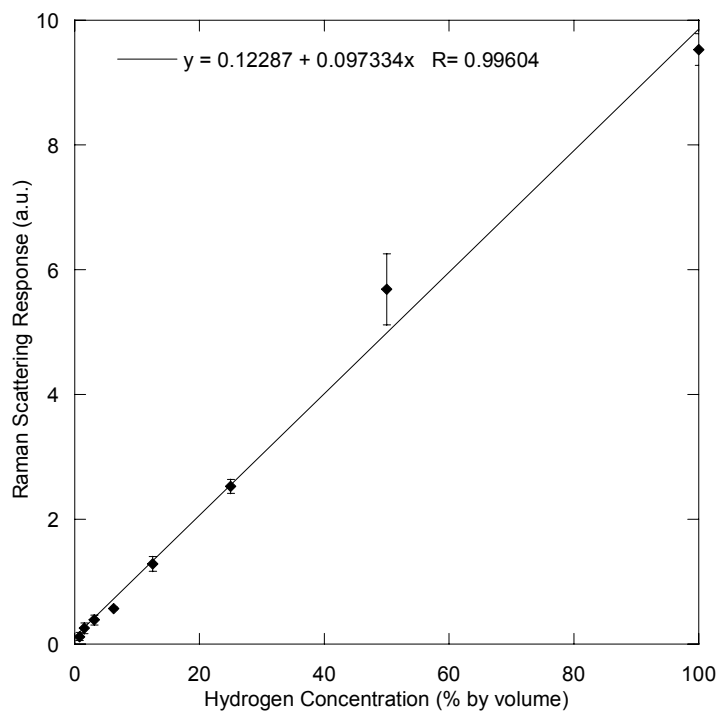


Figure 4.19 Scattering response of hydrogen at an incident wavelength of 355 nm, a pulse energy of 125 mJ/pulse, and collection lens diameter of 4”.

As with previous scattering responses at 355 nm, the response exhibited a strong linear ($R=0.996$) response over the entire concentration range. The response for concentrations less than 25% by volume and the associated regression for detection limit determination are shown in Figure 4.20.

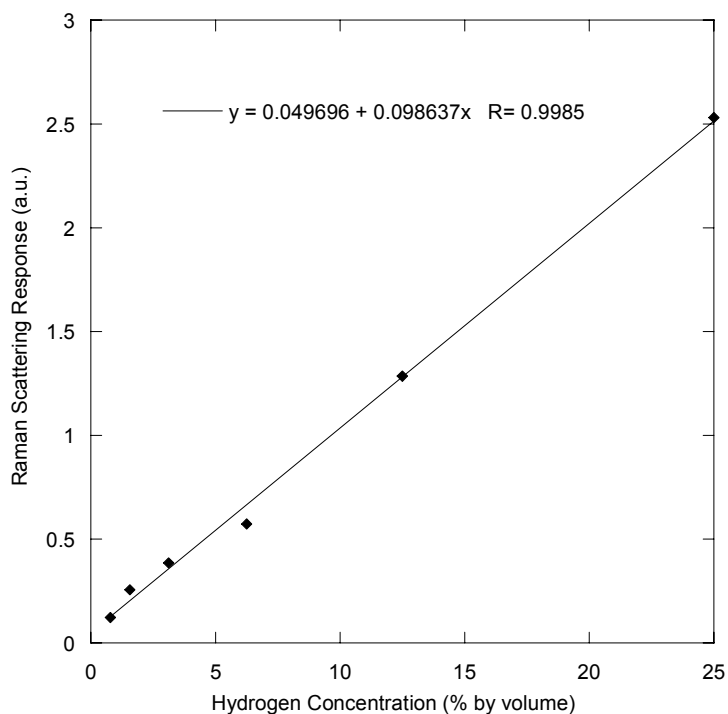


Figure 4.20 Scattering response of hydrogen at an incident wavelength of 355 nm, a pulse energy of 125 mJ/pulse, and collection lens diameter of 4" for concentrations below 25% by volume.

The detection limit calculated for the response in Figure 4.20 was 1.94% by volume or 0.8 $\mu\text{mol/L}$. This was the lowest detection limit achieved up to this point in experimentation. This result showed that increasing the collection lens diameter had more influence on detection limit than increases in pulse energy due to the increase in collection efficiency of backscattered photons gained with a larger collection optic.

The final configuration tested at 355 nm maximized collection through the use of a 4 inch collection lens and a pulse energy of 250 mJ/pulse. The response observed for this configuration is shown in Figure 4.21.

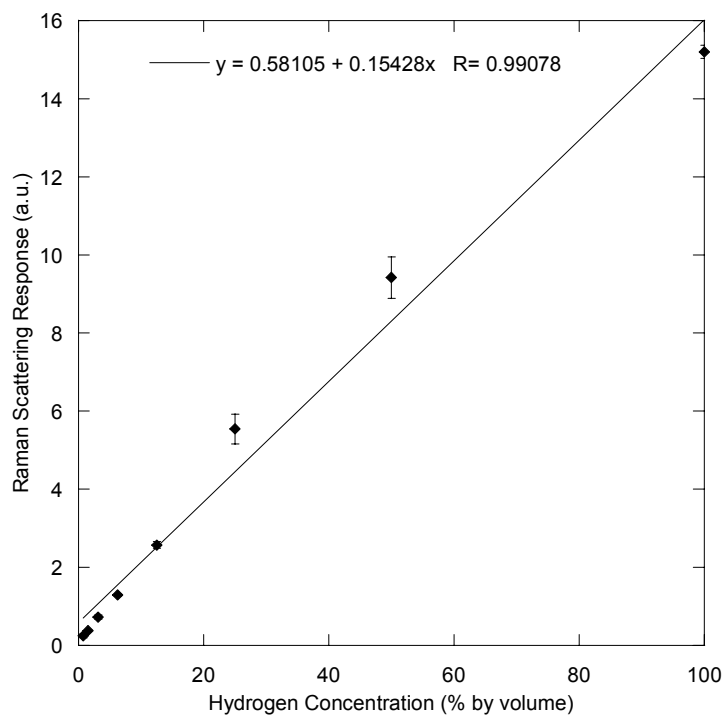


Figure 4.21 Scattering response of hydrogen at an incident wavelength of 355 nm, a pulse energy of 250 mJ/pulse, and collection lens diameter of 4”.

The response observed was slightly less linear ($R=0.991$) than the other responses at 355 nm but exhibited higher sensitivity to changes in hydrogen concentration. Figure 4.22 exhibits the response for less than 25% by volume. Using the linear regression depicted in Figure 4.22, the limit of detection was calculated to be 0.76% hydrogen by volume or 0.31 $\mu\text{mol/L}$, the lowest LOD determined during all Raman experimentation. This result confirmed that successful remote detection of hydrogen below the flammability limit is possible using spontaneous Raman backscattering if collection efficiency and signal noise are addressed.

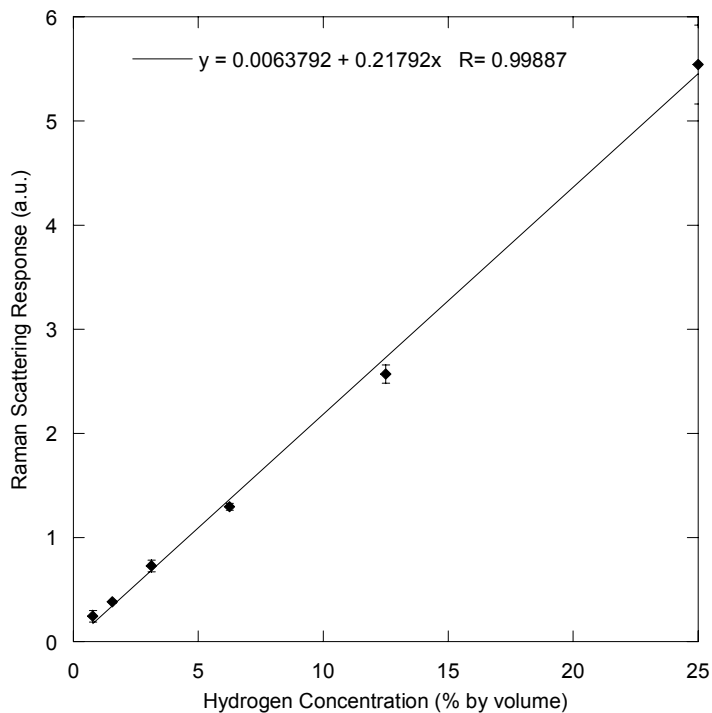


Figure 4.22 Scattering response of hydrogen at an incident wavelength of 355 nm, a pulse energy of 250 mJ/pulse, and collection lens diameter of 4" for concentrations below 25% by volume.

Calculation of photon arrival rates at the detection limit were made to ensure that a significant number of actual scattered photons were being detected. Arrival rates were calculated, using the procedure described in Chapter 3, for the two 355 nm configurations achieving detection limits below the flammability limit. Table 4.2 lists the two photon arrival rates calculated by configuration along with the detection limit used for their calculation. Assuming a loss of 500 photons per pulse due to fiber optic and spectrometer losses at a 10 Hz repetition rate, the number of photons lost per second prior to detection is approximately 5000 photons. Examination of the theoretical photon arrival rates listed in Table 4.2 shows that excess photons are present for signal detection in lieu of instrumentation losses thus the scattering signals observed are actual scattering responses and not artifacts of other optical phenomena.

Table 4.2 Photon arrival rate calculations by optic configuration for 355 nm incident radiation.

Optical Configuration	Detection Limit Concentration (mol/L)	Photon Arrival Rate (photons/sec)
4" lens, 125 mJ/pulse	0.0008	1.04E+05
4" lens, 250 mJ/pulse	0.00031	4.04E+04

A comparison of the response for the four configurations using 355 nm excitation was made to examine relative levels of sensitivity. Figure 4.23 shows the four scattering responses and associated linear regressions by collection lens diameter and pulse energy.

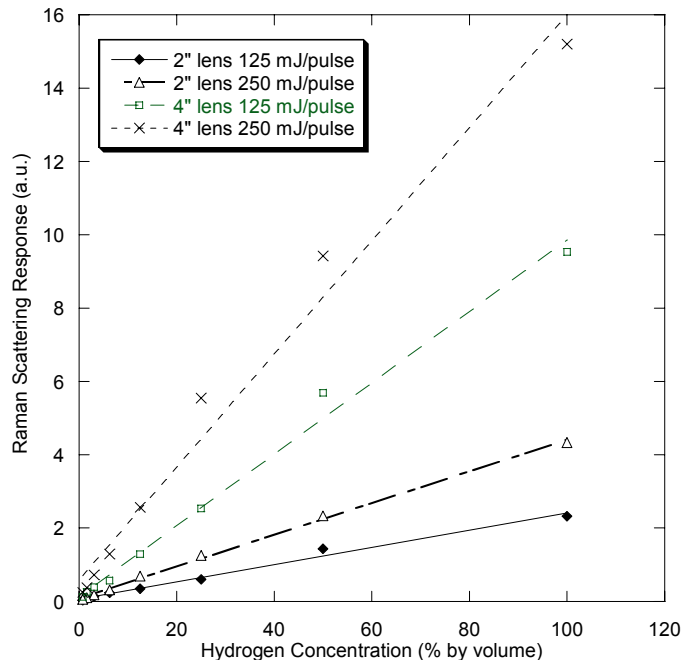


Figure 4.23 Scattering responses for the four optical configurations examined with 355 nm incident radiation. The lines exhibit the linear regression for each response.

An increase in collection lens and an increase in pulse energy both resulted in increased sensitivity for the scattering response as shown in Figure 4.23. The influence of collection lens diameter on response sensitivity was observed to be more significant than the influence of pulse energy as both responses with the 4 inch lens had greater slopes

than the responses with the 2 inch lens. This is an important result for application of this technique to field detection. Due to the need for portability and robustness, a field detection system will not have a laser excitation source with high pulse energies. These results show that by increasing optic size, detection limits below the flammability limit can still be achieved with a lower pulse energy system. In addition, scaling was observed in Figure 4.23 between the response points at individual concentrations. Figure 4.24 is a plot of the response for one hydrogen concentration versus a formulated scaling parameter, the pulse energy times the lens diameter squared.

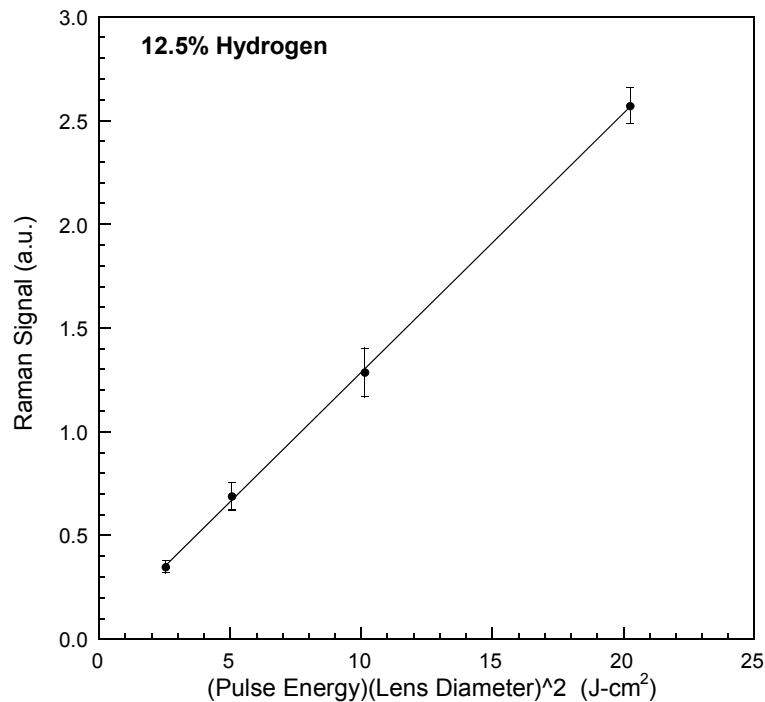


Figure 4.24 Scattering response at 12.5% hydrogen by volume versus the derived scaling parameter.

The linear behavior of Figure 4.24 shows that there is a direct correlation between the scaling parameter which is dependent on pulse energy and the lens diameter and the scattering response as expected from Raman theory. This scaling parameter will be an important design parameter for the construction of a Raman field detection system.

Two optical configurations were also examined for 532 nm incident radiation. The first configuration used a pulse energy of 125 mJ/pulse and a 4 inch collection lens and the second configuration used a pulse energy of 250 mJ/pulse with a 4 inch collections lens. Scattering responses were not examined with a 2” collection due to the low detection limit and sensitivity observed in Section 4.2. Figure 4.25 and Figure 4.26 show the scattering response measured for 125 mJ/pulse and 250 mJ/pulse respectively.

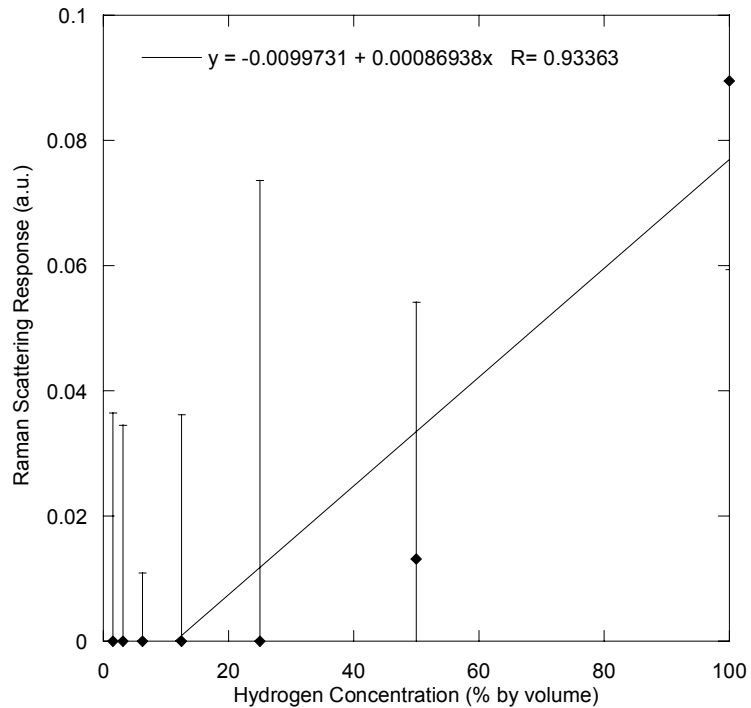


Figure 4.25 Scattering response of hydrogen at an incident wavelength of 532 nm, a pulse energy of 125 mJ/pulse, and collection lens diameter of 4”.

Both scattering responses show no detection was achieved for concentrations below approximately 10% hydrogen by volume. While limited low concentration detection with low sensitivity was seen in Section 4.2 with only one high pass filter, it was concluded based on the response shown in Figure 4.25 and 4.26 that detection was not possible below the flammability limit using 532 nm incident radiation.

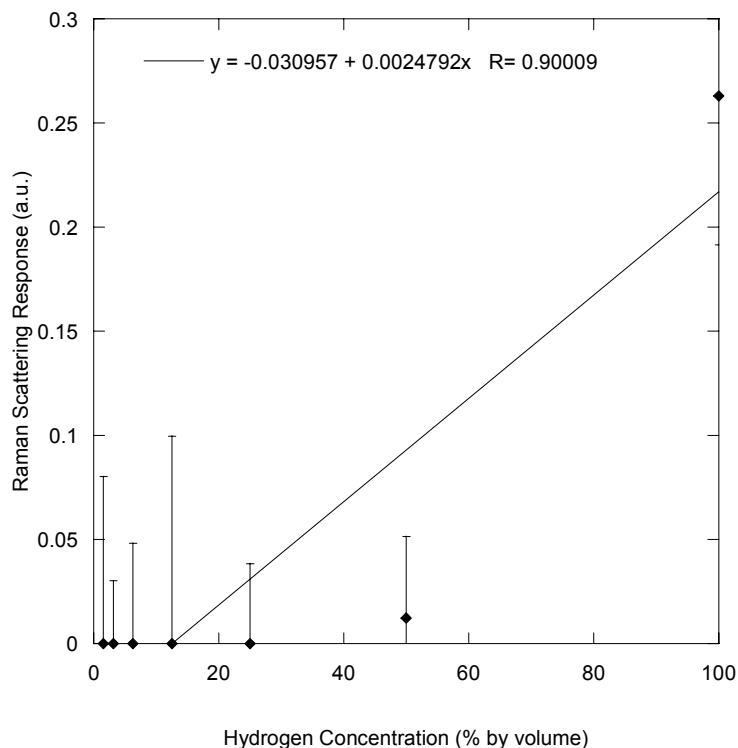


Figure 4.26 Scattering response for hydrogen at an incident wavelength of 532 nm, a pulse energy of 250 mJ/pulse, and collection lens diameter of 4”.

The investigations of optical configuration on scattering response showed that detection well below the flammability limit could be achieved with the use of a 4 inch collection mirror and lens with 355 nm radiation while the use of 532 nm incident radiation was shown to be impractical for hydrogen concentration measurements by spontaneous Raman scattering. In addition, it was shown that low limits of detection could be maintained at decreased pulse energies due to the increase in collection efficiency from increased collection optic diameters. With significant detection limits achieved in the laboratory, a prototype PMT field detection system could be constructed to detect hydrogen gas concentrations. Before a field device was addressed, the use of an ICCD was examined in place of the PMT.

4.4 Limit of Detection using an ICCD

With detection limits achieved in the desired range for two PMT configurations, the detection limit using an ICCD was investigated. As noted in Chapter 3, the incident wavelength used was 355 nm with a pulse energy of 250 mJ/pulse. The 4" collection lens was used in order to make a direct comparison to the PMT configuration achieving the lowest limit of detection. The concentrations, as shown in Table 3.5, were also the same as previous experiments. Three scattering signals were recorded at each concentration. Each signal represented the accumulation of 150 samples therefore all signals were divided by 150 to achieve an average scattering signal. This method is consistent with the PMT signals which were 150 shot averages. Figure 4.27 shows an average scattering signal obtained with the ICCD for 100% hydrogen by volume.

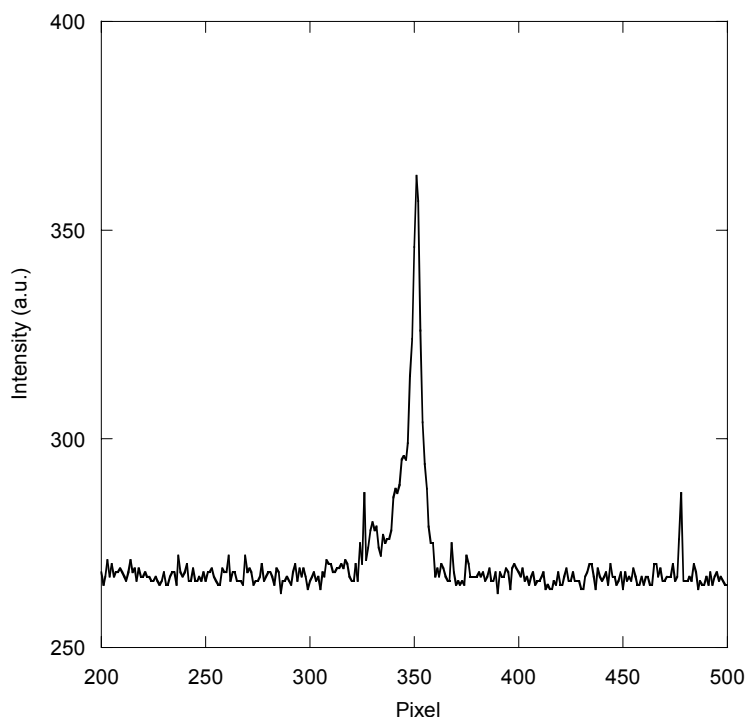


Figure 4.27 ICCD spectrum showing the Raman line for at 415.91 nm for a 100% by volume sample of hydrogen at atmospheric pressure.

Since the ICCD detects a spectrum in contrast to the transient intensity detected by the PMT, the scattering signal is analyzed by a different method. To determine the scattering response, the average baseline which consists of background noise and dark noise was first calculated by averaging the signal intensity over the pixel range 244 to 301. The calculated average baseline intensity was then multiplied by the full peak width of the Raman line of 24 pixels to obtain an integrated baseline signal. The peak was then discretely integrated over its full 24 pixel width and the integrated baseline was subtracted from the integrated peak to yield the scattering response signal for the particular hydrogen concentration under investigation. Once the scattering response was calculated for all data points, the three sample points for each concentration were averaged to yield the average scattering response as shown in Figure 4.28. The error bars depict one standard deviation in scattering response.

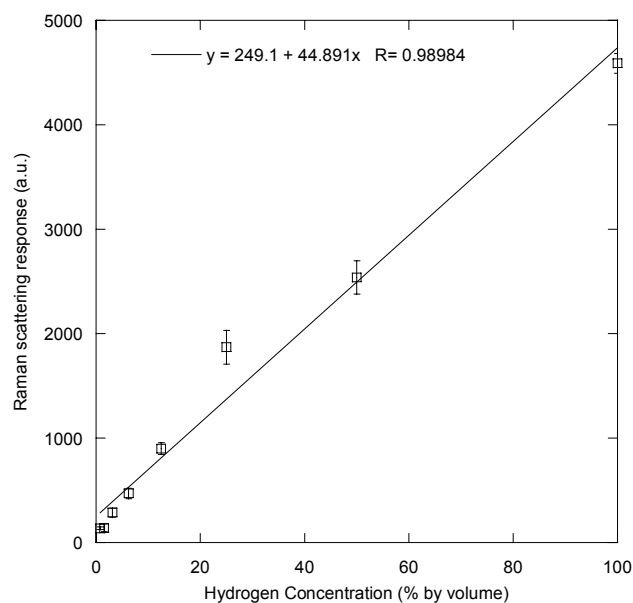


Figure 4.28 Scattering response of hydrogen at an incident wavelength of 355 nm as determined using an ICCD.

Using the ICCD, a linear scattering response ($R=0.989$) was observed that is similar to the response seen with PMT detection. The limit of detection was again calculated using only concentrations below 25% by volume as shown in Figure 4.29.

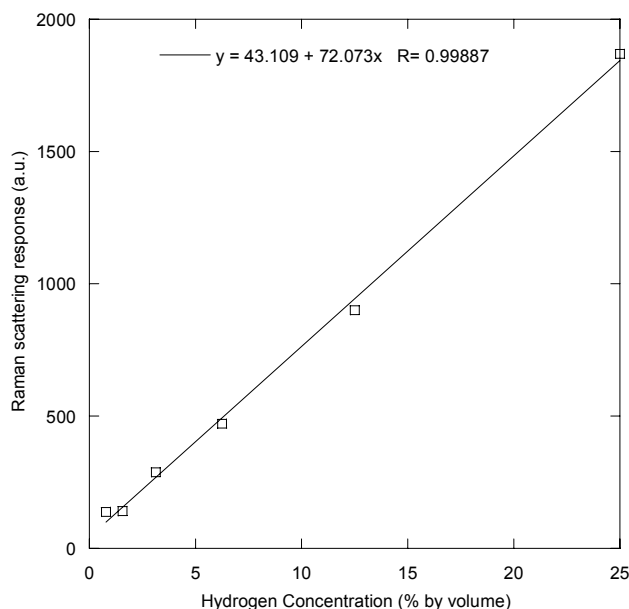


Figure 4.29 Scattering response of hydrogen at an incident wavelength of 355 nm as determined using an ICCD for concentrations below 25% by volume.

The limit of detection determined from the ICCD measurements was 1.79% by volume or 0.74 $\mu\text{mol/L}$. While below the flammability limit of 4% by volume, this detection limit was higher than the detection limit achieved with the PMT configuration at 250 mJ/pulse with a 4" lens. This was an encouraging result as a PMT based detection scheme yields to easier field implementation and detection therefore no additional consideration was given to the ICCD configuration.

4.5 Raman Field Instrument

The laboratory backscatter experiments illustrated that limits of detection well below the flammability limit of hydrogen could be achieved with increased diameter collection optics and multiple high pass filters. With detection limits verified, a field

deployable Raman backscattering monitor for hydrogen was constructed as described in Chapter 3. The testing of the field system was not included within the scope of this work. Implementation and testing is addressed in the future work discussion of Chapter 6.

CHAPTER 5 RESULTS AND DISCUSSION OF HYDROGEN DETECTION BY LIBS

This chapter presents the results of two hydrogen detection experiments using Laser-Induced Breakdown Spectroscopy. This first investigation conducted in this section was a comparison of the hydrogen detection ability for two different LIBS configurations. A comparison was made between the use of a gas-initiated versus substrate-initiated breakdown for the detection of hydrogen by LIBS. As part of this study, multiple candidate surfaces were compared for substrate-initiated LIBS hydrogen detection. The second LIBS investigation presented in this chapter examined the effect of surface ablation of a LIBS substrate on hydrogen detection response.

5.1 Gas-phase versus Substrate-initiated LIBS for Hydrogen Detection

Two LIBS methodologies were examined in this experiment to determine minimum detection limits and sensitivity for hydrogen detection using LIBS. The first methodology examined was the use of a substrate-initiated plasma that envelopes gas from the surrounding gas stream for the purpose of hydrogen detection and quantification. As stated before, the advantage of this methodology lies in the lower energy required to generate the plasma due to the higher free electron density of a solid surface in comparison to a gas, while the drawback to this approach is the limited lifespan of the plasma initiating substrate due to material ablation. The second LIBS detection scheme examined was the use of a breakdown directly in the sample gas stream with the advantage of no finite lifetime based on the number of plasmas generated and the

availability of emission over 4π steradians allowing variable collection optic configurations. The detection ability of these configurations is the primary focus for any practical implementation. An investigation of candidate substrates for surface-initiated LIBS was conducted prior to a comparison of the two LIBS methodologies as described in Chapter 3.

Six metals were examined as candidate substrates, namely: copper, aluminum, stainless steel, titanium, tungsten and molybdenum. Ambient water vapor at a concentration of about 1.5% in air or 1000 ppm was used as an analyte source. All sample metals were adhered to the rear flange of the vacuum cross depicted in Figure 3.10 and the focusing lens distance was adjusted so that the focal spot was at the surface of the candidate material. Six 50 shot average emission spectra of the H_α line for hydrogen were collected for each substrate at a pulse energy of 55 mJ/pulse over six detector delays spanning 2-12 μ s. Comparison of the spectra recorded for each material revealed the greatest ratio of hydrogen emission to continuum background occurred at a delay of 4 μ s. Using spectra collected at a delay of 4 μ s, a comparison was made between the data for the different substrate candidate metals. To accomplish this comparison, scaling of each spectrum was accomplished using ratios of the continuum region of the spectrum as described in Chapter 3. Figure 5.1 shows the scaled spectra for five of the metals, shifted apart for clarity. Titanium was not included with the spectra because, while showing a strong H_α peak, it exhibited many overlapping emission lines in the same region of the spectrum. A strong H_α emission line can be observed for all five metals presented in Figure 5.1. In addition, few strong emission peaks are seen otherwise in the spectra with the exception of the copper peaks at 649.5 nm and 654.8 nm.

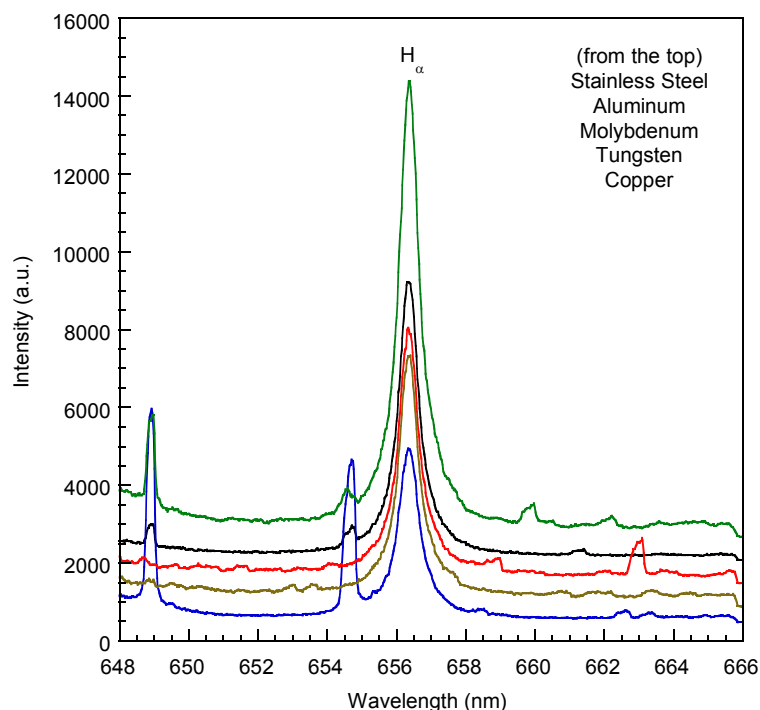


Figure 5.1 LIBS spectra of candidate substrate materials showing the H_{α} line for hydrogen from ambient water vapor at 1.5 % by volume. All spectra have the same scale but have been shifted vertically for clarity.

These peaks correspond to second-order-copper lines generated through higher-order diffraction from resonant Cu(I) lines at 324.8 nm and 327.4 nm. These second-order copper peaks can also be seen in Figure 5.1 at reduced intensities in the spectra for stainless steel and aluminum which contain small, alloyed concentrations of copper. Using these spectra, stainless steel was selected as an ideal candidate for surface-initiated LIBS due to the intense H_{α} peak observed in its spectra, the lack of any significant emission lines around the hydrogen emission line, and for convenience as the rear flange cap used for mounting of all the other metals was constructed of 304 stainless steel thus eliminating the need for substrate preparation.

With stainless steel selected as a substrate for plasma-generation, an experiment was performed to compare the detection limits and sensitivity for hydrogen of gas-phase

versus solid-initiated LIBS plasmas. Using the same experimental setup from the investigation of the surface materials, stainless-steel initiated plasmas were examined with a detector delay of 4 μs and a gate width of 4 μs . Average spectra of 50 shots were collected at each of the concentrations listed in Table 3.9 along with one average spectra for pure nitrogen flow before and after to serve as the blank spectra for spectral analysis. Once all spectra were collected for breakdown on the surface, the focusing lens was adjusted to center the plasma in the center of the sample cell. The power was increased to 100 mJ/pulse to achieve a gaseous breakdown. The same sample collection procedure was repeated to achieve multiple 50 shot average spectra for every concentration and two blank spectra. With all data collected, the two blank signals were averaged for each configuration and a scaled average blank spectra was generated for all hydrogen sample spectra as described in Chapter 3. Two sample spectra with their scaled blank spectra are illustrated in Figure 5.2. Subtraction of the blank spectra from the sample spectra yielded the absolute signals peaks. Figure 5.3 shows four absolute peaks corresponding to four different sample hydrogen concentrations. The blank spectra and the hydrogen spectra were integrated over the full hydrogen peak width and the integrated blank was subtracted from the integrated hydrogen peak to determine the integrated absolute hydrogen peak value for response measurement.

As discussed in Chapter 3, various levels of CCD binning were used during collection of the sample data so a peak-to-base (P/B) method was employed which corrects for these levels of binning through a ratio of the integrated absolute hydrogen peak to the integrated base.

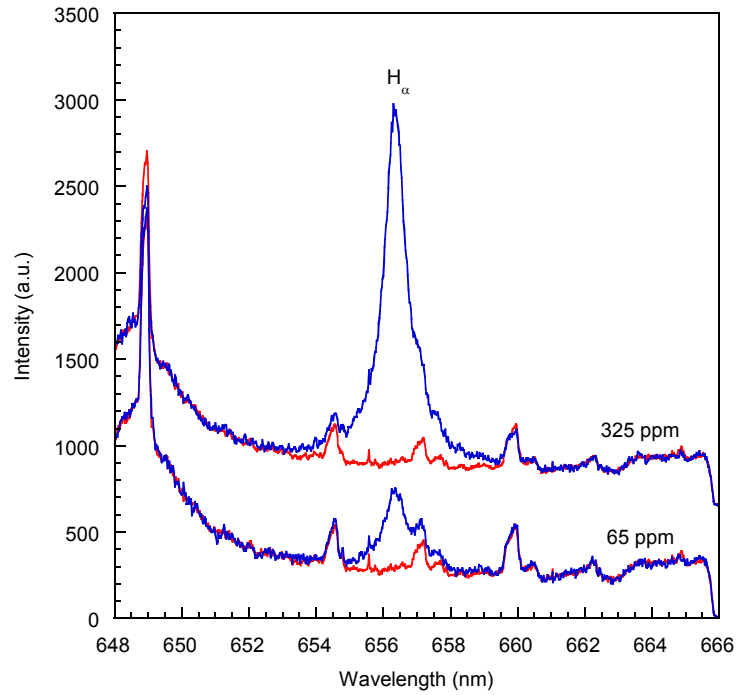


Figure 5.2 Example plasma emission spectra for 65 ppm and 325 ppm hydrogen concentrations with the corresponding scaled background spectra.

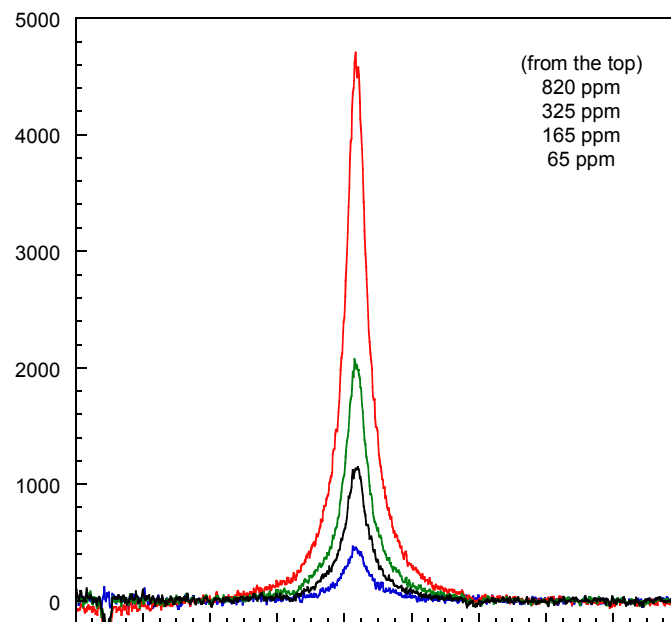


Figure 5.3 Background subtracted LIBS spectra for four experimental hydrogen concentrations in nitrogen.

In addition, the P/B ratio helped to account for natural fluctuations in plasma emission, therefore, P/B ratios served as a good measure of the response of the LIBS technique to changing hydrogen concentrations. The P/B ratios for both the gas phase and substrate LIBS plasmas as a function of hydrogen concentration are shown in Figure 5.4 for a concentration up to 4.4%, which is beyond the flammability limit for hydrogen. Error bars depict one standard deviation in the values of the P/B ratio.

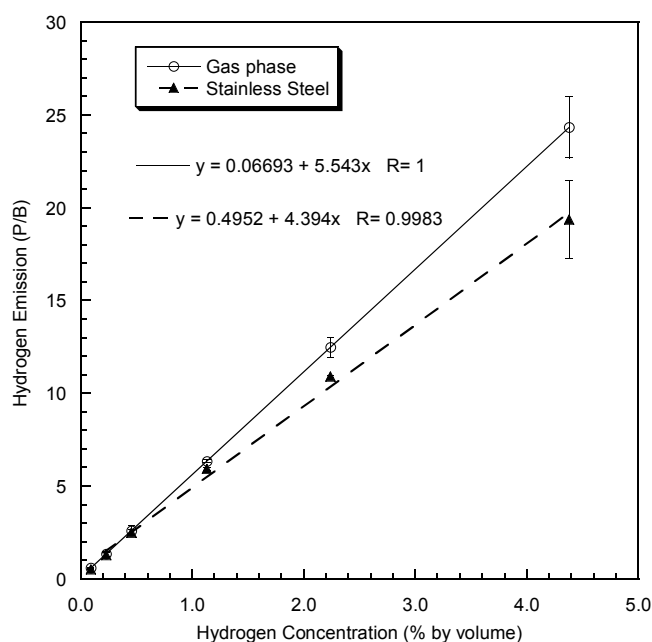


Figure 5.4 Gas phase and stainless steel LIBS emission response to hydrogen concentration below 4.4% by volume.

The response of the plasma emission to hydrogen concentration below 4.4% by volume was observed to be highly linear for both the gas-phase and substrate-initiated cases, as shown in Figure 5.4, with regression coefficients of $R=1.00$ and $R=0.998$, respectively. A closer inspection of the data in Figure 5.4 revealed that below a concentration of 1.13%, the two LIBS approaches had approximately the same response. For a better comparison, regressions for the response only up 1.13% hydrogen by volume were calculated as shown in Figure 5.5.

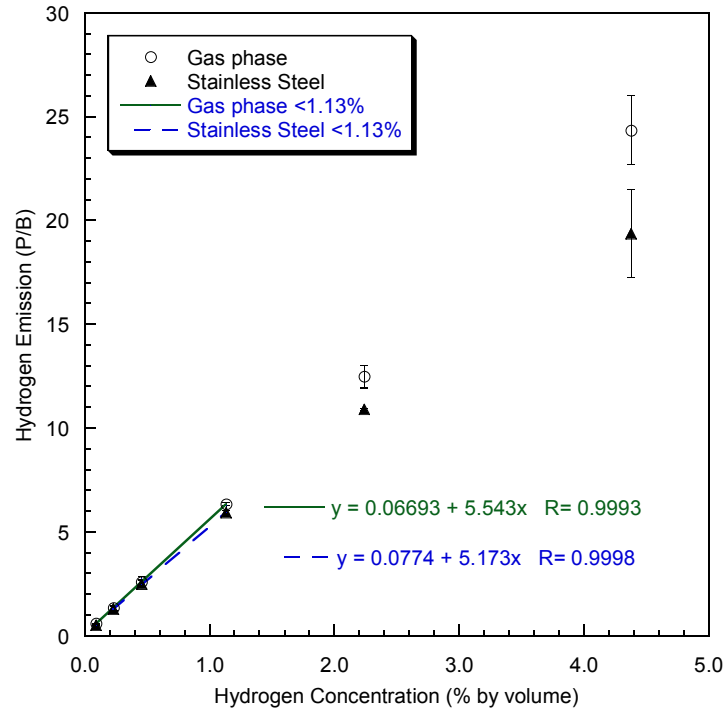


Figure 5.5 Gas phase and stainless steel LIBS emission response to hydrogen concentration. Linear regressions are shown for data below 1.13% hydrogen by volume.

Examining only the data below 1.13% hydrogen by volume, both the gas phase and stainless steel methods exhibited comparable linear ($R > 0.999$) responses to changes in hydrogen concentration. Above 1.13%, the departure from linearity observed previously could be due to optical depth and the resultant self absorption of emission by the plasma. This possibility will be examined later in this section.

With a highly linear response observed at low hydrogen concentrations for both the gas phase plasma and the surface plasma, the limits of detection for both configurations were calculated as described in Chapter 3. Limits of detection were calculated for each of the individual calibration curves that comprised the average curves in Figure 5.4 and 5.5. The detection limits were then averaged in their respective gas phase or substrate group. For substrate-initiated LIBS, the detection limit was found to

be 15 ppm by mass or approximately a quarter of the lowest concentration measured in this experiment. For gas phase LIBS, the detection limit was found to be 23 ppm by mass. These results are almost identical, suggesting not only that effective hydrogen detection can be achieved with either technique but that the plasma generated in each method was similar, even with different initiation procedures.

A comparison of the plasma emission signals was performed to determine if the plasmas were comparable in electron density and thus similar. Previously, it was noted in Figure 5.4 that the substrate-initiated plasma exhibited a slightly less linear response than that of the gas phase plasma. This could be the result of a smaller plasma resulting from the lower pulse energy employed for those experiments. To determine the plasma electron densities, the level of Stark broadening was examined for the H_{α} peak of the gas phase and substrate-initiated plasma. Calculations of electron density were made in the manner presented in Chapter 3 at three intermediate hydrogen concentrations using the FWHM of the associated H_{α} peak. An average plasma temperature of 20,000 K was used for all calculations with an uncertainty of $\pm 10,000$ K used to evaluate the maximum error. The calculated electron densities are shown as a function of hydrogen concentration in Figure 5.6 for the gas phase and substrate-initiated plasmas. The calculated electron densities show that the two plasmas were comparable, falling within experimental uncertainty, at each of the three sample concentrations. Figure 5.6 also shows that a higher electron density was found for the substrate initiated plasmas at all three concentrations. This was most likely due to the elevated electron density of the solid in comparison to the gas prior to breakdown. The finding of comparable plasmas supports the conclusion that the detection limits indicate almost identical plasmas.

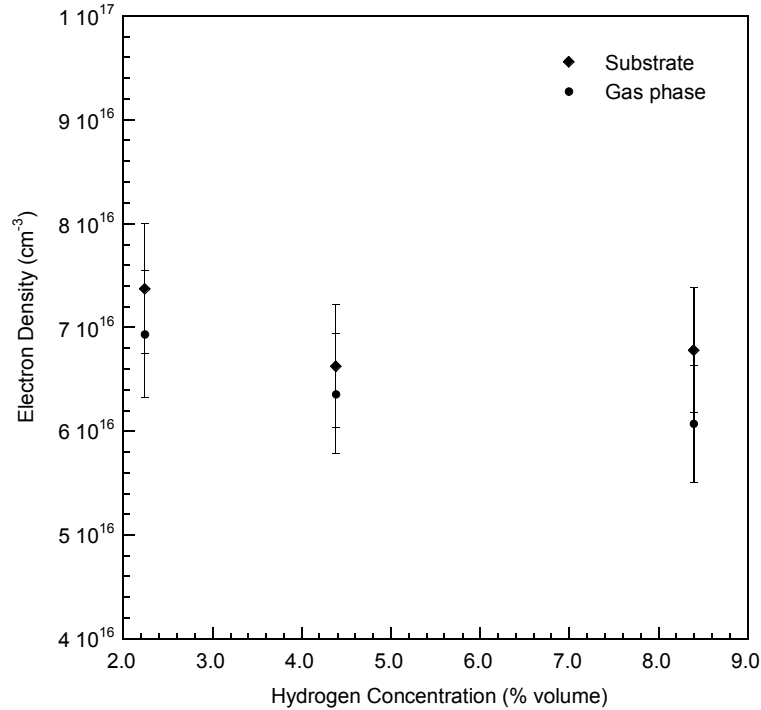


Figure 5.6 Plasma electron densities at three sample hydrogen concentrations for substrate and gas phase initiated plasmas.

Finally, the slight deviation from linearity observed in plasma response was examined to determine if self-absorption of emission was present in the plasma. Hydrogen emission for concentrations up to 26.8% or 25,500 ppm by mass was recorded during experimentation. The P/B ratios for the gas-phase over the full concentration range are shown in Figure 5.7. A log-log plot was used in Figure 5.7 to examine the linearity of the curve of growth for hydrogen emission over a broad range of concentrations. The illustrated line, added for clarity, shows that the curve of growth was highly linear for the plasma over a broad concentration range illustrating that emission was not appreciably affected by optical depth and thus no self-absorption mechanisms were present (Aguilera 2003).

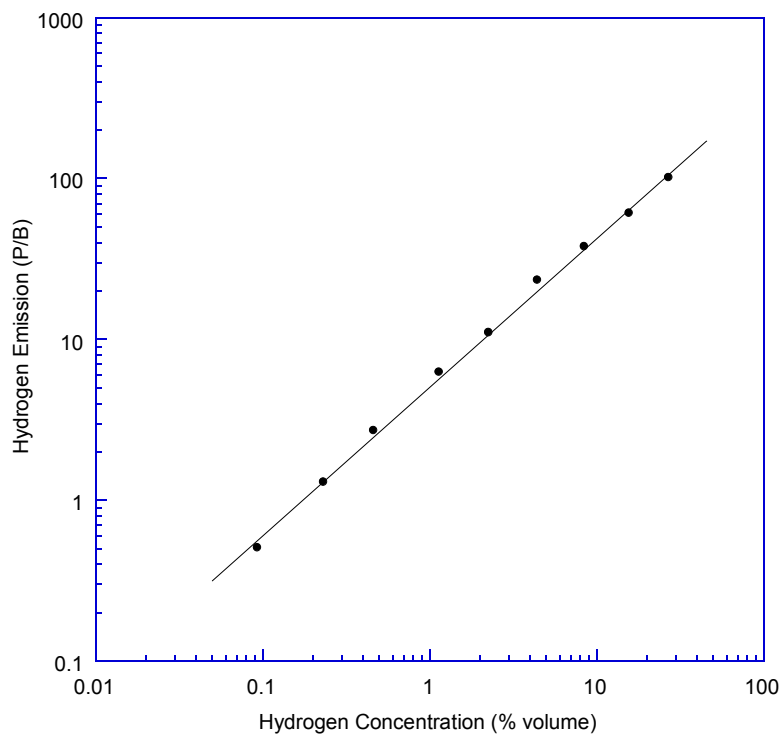


Figure 5.7 H_{α} emission for a gas phase LIBS plasma. A solid line has been added for clarity.

Gas-phase and surface-initiated laser induced breakdown spectroscopy have been shown to provide low limits of detection, 15 ppm and 23 ppm respectively, and high sensitivity for hydrogen. The comparable nature of the results for both plasmas was encouraging as the use of surface-initiated LIBS is preferred for field detection applications due to the lower laser pulse energy required. While exhibiting effective hydrogen detection, two concerns arise from these experiments regarding the use of LIBS as a detection technique. The first concern is with regards to LIBS being a form of atomic spectroscopy. Any species containing atomic hydrogen will be detected by this method as illustrated by the ambient water vapor used for substrate testing. Therefore, for a practical detection technique, LIBS must either be performed in a sample chamber with an inline cold trap prior to the chamber to condense water and other pollutants from

the sample, or performed with algorithms to account for ambient hydrogen concentrations. The second concern is with regards to the ablation of the substrate during surface-initiated LIBS. Ablation of a substrate dictates that maintenance of the detection device will be required at certain intervals depending on the material toughness. In addition, there could possibly be an effect of ablation on detection ability as a crater is formed on the sample surface. All experiments performed to this point consisted of a few thousand shots on a surface that was previously unablated. To address this concern, a brief investigation was performed to examine the effect of substrate degradation on hydrogen emission.

5.2 Substrate Degradation Experiments

Surface-initiated LIBS takes advantage of the high free electron density and mobility in a solid surface to initiate plasma formation with lower incident energy. While effective as a plasma former, some of the surface material is entrained in the plasma. Ablation of the surface results in small concentrations of lost surface material which, after many plasma formations, can result in the formation of a crater in the solid surface. As stated previously, this ablation is of interest for two reasons. The first reason is that surface ablation can result in increased maintenance requirements for any practical LIBS field detection system. Second and most importantly is the issue of whether surface changes can result in changes in signal response for chemical identification. For these reasons, surface degradation by LIBS plasmas is now briefly examined.

Using scanning electron microscopy (SEM), an image of one of the stainless steel flange caps from the detection limit studies was collected as shown in Figure 5.8. Scanning electron microscopy probes surface structure by displacing surface electrons

with the use of a scanning beam of incident electrons. These displaced electrons are collected and amplified yielding a highly magnified image of the surface.

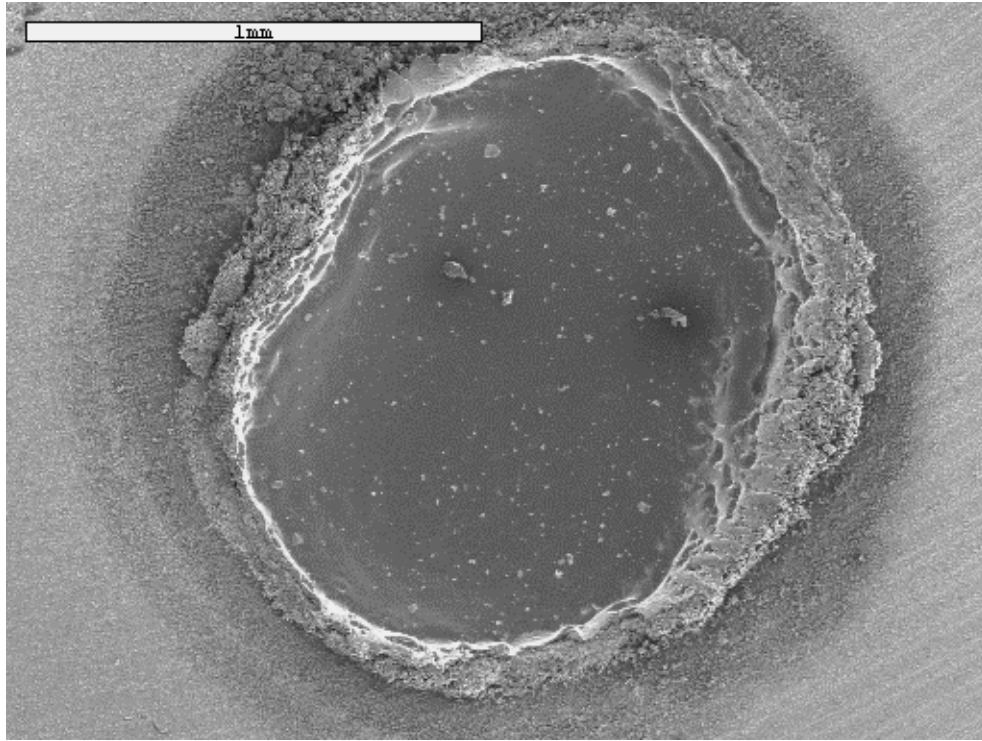


Figure 5.8 Stainless steel surface crater formed by ablation after repeated detection limit studies at the same substrate location.

The crater shown in Figure 5.8 exhibits some interesting structural features. The first is the accumulation of solidified metal around the edges of the crater. This increased surface area could increase the energy of the surface thus lowering the threshold over time for plasma initiation. The second feature of interest is the almost vertical wall of the ablated crater. This feature could possibly affect signal response by limiting emission solid angle if the crater is of sufficient depth. Also, a large crater depth could result in the buildup of hydrogen gas in the crater over short time spans with a different concentration in relation to a sample flow passing over the surface. This would thereby generate plasma emission that is not proportional to the sample flow concentration. A final note on the crater presented in Figure 5.8 is the presence of a relatively flat and smooth crater base.

This flat structure is not always seen as will be discussed below. With these issues denoted, a series of experiments were conducted to examine crater structural changes and emission response in relation to the number of plasmas generated on the substrate.

The first experiment conducted involved recording hydrogen emission for 100 shot averages for a period of one hour as described in Chapter 3 using the second LIBS experimental setup. The concentration of hydrogen in the sample gas flow rate was constant at 16.6% hydrogen by volume and an unablated stainless steel flange cap was used as the substrate. Two blank spectra were recorded at a previously unablated site on the sample disc. With the blank spectra recorded, the disc was rotated on the flange to a new unablated spot at the focal spot of the laser. Subsequently, 100 shot averages were collected at a 5 Hz repetition rate for a period of one hour thereby exposing the sample surface to 18,000 laser shots. For each of the 180 hydrogen average emission spectra, a simple peak-to-base ratio was calculated for the H_{α} line, as described in Chapter 3, to measure the hydrogen signal response to the total number of shots impacting the surface. A plot of the P/B ratios as a function of total laser shots is given in Figure 5.9. A study of the substrate P/B ratios after an hour showed an initial trend of decreasing hydrogen emission for the first few thousand shots followed by a gradual increase in emission which appeared to level off by the time 10^4 total shots were reached. A few outlier points are seen around 10^4 total shots but the emission otherwise followed the observed pattern as shown in Figure 5.9. This data suggested that there might be a relationship between signal response and the total number of shots to which a surface had been subjected.

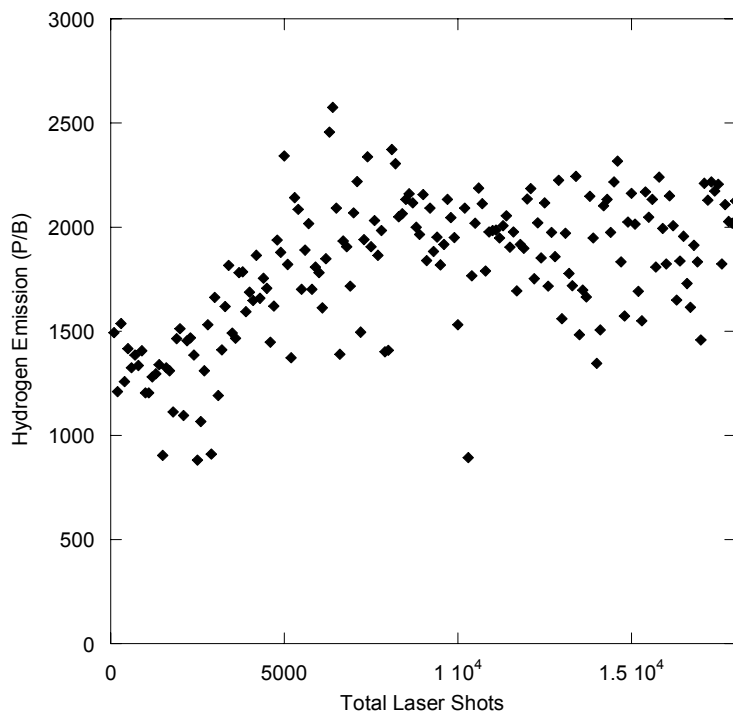


Figure 5.9 Hydrogen P/B ratios as a function of the total number of laser shots for stainless-steel initiated LIBS. The hydrogen gas sample had a concentration of 16.6% hydrogen by volume.

A picture of the crater in Figure 5.10 shows a relatively small amount of ablation over the 18,000 shots. The original substrate examined from the detection limit studies showed a more pronounced crater signifying it was subjected to many more laser shots.

With a possible trend observed in hydrogen emission as a function of the total shots to which the LIBS substrate was exposed, a second experiment was conducted. In addition, the time of sampling was increased to 2.5 hours to achieve a crater depth of similar magnitude to that of the crater seen from the detection limit studies. With the same repetition rate of 5 Hz and 100 shot averages, the stainless steel substrates for this study were subjected to a total of 45,000 shots in 2.5 hours. Two sample sets were collected and averaged to observe the variation in response. All other experimental parameters were held constant from the first substrate study.

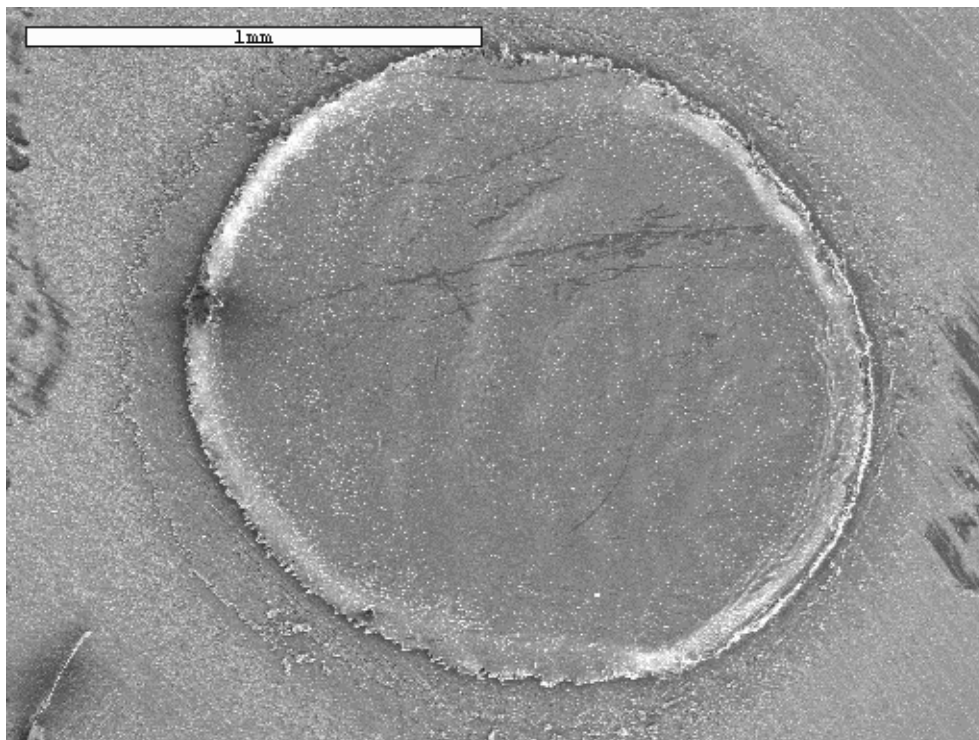


Figure 5.10 Stainless steel substrate crater after ablation by 18,000 laser shots in a hydrogen and nitrogen atmosphere.

Using simple peak-to-base ratios, the response of hydrogen emission to the total number of shots for the averaged samples is shown in Figure 5.11. A similar trend was observed in emission as a function of total shot number for this second experiment. The hydrogen emission showed a brief decline followed by an increase up to around 10^4 total shots. A somewhat steady regime of hydrogen emission was then observed between approximately 10^4 to $2(10)^4$ total shots as shown in Figure 5.11. Following the steady emission, a decline in the P/B ratio was observed until the end of the sampling period. While investigation of the fundamental process accounting for this observed emission behavior was not the goal of this experiment, the results are important for any practical application of substrate-initiated LIBS.

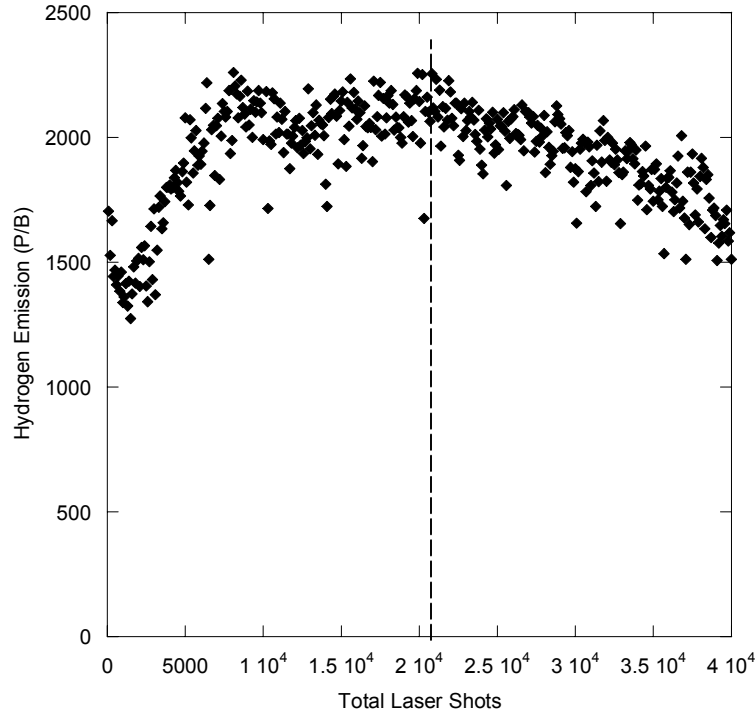


Figure 5.11 Average hydrogen P/B ratios as a function of the total number of laser shots for stainless-steel initiated LIBS. The hydrogen gas sample had a concentration of 16.6% hydrogen by volume.

Fluctuation of the hydrogen emission signal over the lifetime of a detection system due to substrate degradation would not only result in inaccurate concentration monitoring, as demonstrated by these response measurements, but could pose a significant safety risk by incorrectly identifying hazardous hydrogen leaks. The two substrates used for the longer degradation study were also examined using a scanning electron microscope. The recorded images are shown in Figure 5.12. The craters from the 45,000 shot study both exhibit large crater depths and appreciable flow buildup around the crater lip. While the behavior for the first 10^4 shots can be theorized as before, the continually decreasing P/B ratio over a greater number of shots might be attributed to the continually increasing crater depth. As the crater deepens, plasma

“confinement” takes place in the crater thus possibly changing the sampling behavior of the gas by the plasma and the observed emission response.

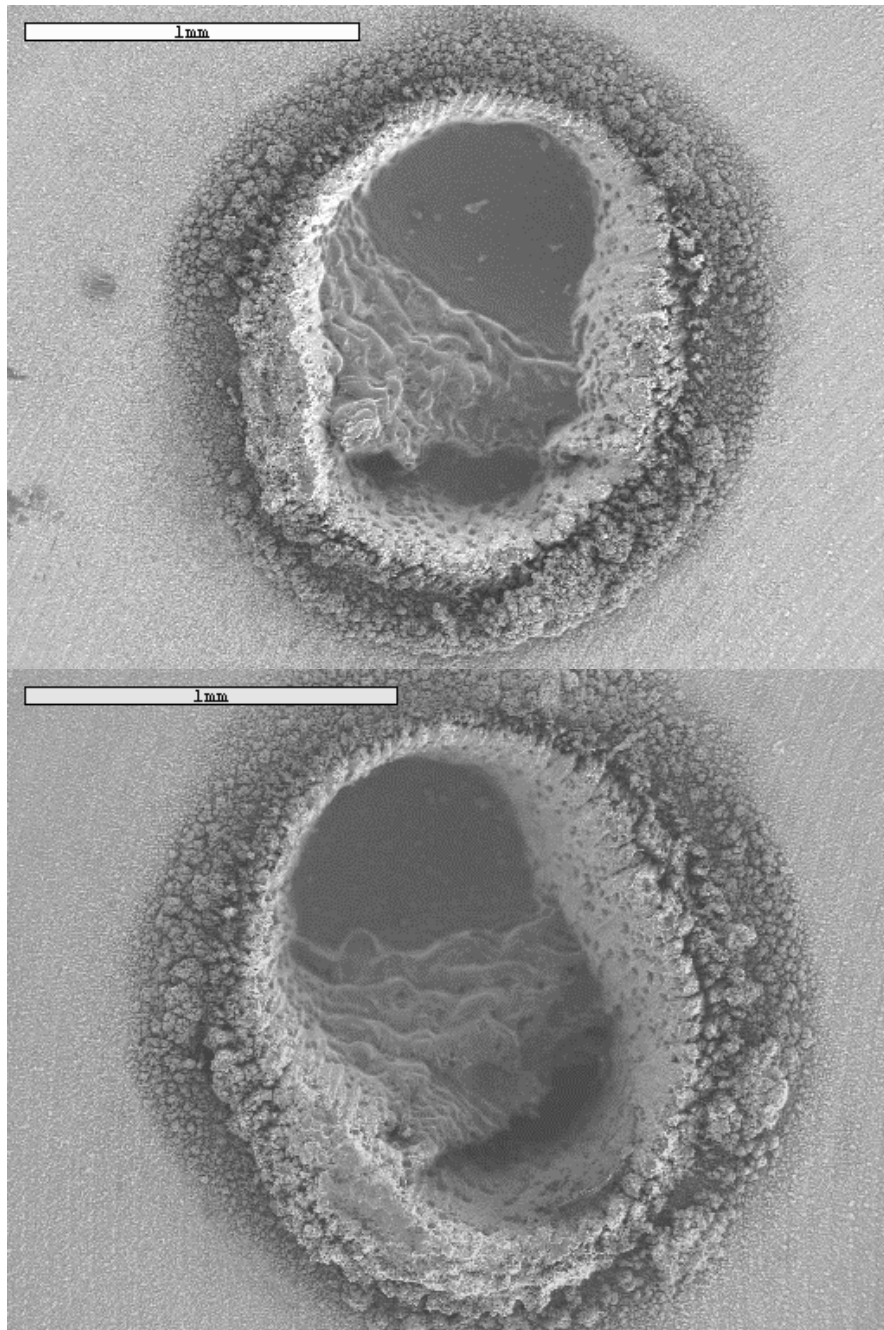


Figure 5.12 Stainless steel substrate craters after ablation by 45,000 laser shots in a hydrogen and nitrogen atmosphere.

To maintain signal response, a hydrogen detection system would need to be limited to a certain number of shots based on this behavior before substrate replacement is required. For instance, at a rate of 2 Hz using 100 shot average samples, substrate replacement would be required after 200 samples or approximately every two hours and forty-five minutes. Increased substrate lifetime would increase the practicality of a LIBS field detection system. Finally, an interesting feature observed for both craters was the flow of metal back into the base of the crater as shown in Figure 5.12. Characterization of this flow might allow for understanding of the decrease in response seen after a large number of laser shots.

The goal of this study was not to characterize substrate ablation behavior but rather to briefly address the effect of substrate degradation on hydrogen emission. It has been shown that a fluctuation in hydrogen emission exists at a constant concentration as the total number of ablation events increases. This variation must be addressed in the design of a practical hydrogen detection system using surface-initiated LIBS to ensure measurement accuracy safety.

CHAPTER 6 SUMMARY AND CONCLUSIONS

The problems associated with current fossil fuels have prompted governments and industry to research new energy sources. Hydrogen is the primary energy carrier being promoted for fossil fuel replacement due to its abundant supply and improved environmental and political attributes. The prevalence of current and future hydrogen use coupled with hydrogen safety concerns dictates a need for accurate, rugged, real-time hydrogen detection and monitoring schemes with low limits of detection below the hydrogen flammability limit of about 4% by volume and high sensitivity. Spontaneous Raman scattering and laser-induced breakdown spectroscopy were examined in this work to provide a new remote sensing and point sensing technique, respectively, to hydrogen detection and monitoring with the intention of demonstrating improved detection metrics over current systems.

Spontaneous Raman scattering was examined as a practical scheme for hydrogen detection not only because of its ability to detect species at low concentrations but also because it allows for remote monitoring with a simple, optic configuration and can provide real-time feedback. A backscatter orientation was presented in this work to increase spatial resolution and for ease of practical implementation. Preliminary studies found that Raman exhibited a highly linear response ($R=0.985$) to changes in hydrogen concentration. Low concentration remote detection is challenged by the low scattering intensities associated with Raman scattering and background noise due to fluorescence as a result of a 355 nm excitation source and stray light. A comparison of scattering in

response to 355 nm and 532 nm was conducted to determine if signal-to-noise improvements could be made using a less energetic wavelength. While a significant decrease in noise was observed at the longer wavelength (presumably due to less fluorescence), the loss in scattering intensity resulted in a limit of detection well above the flammability limit for hydrogen. A lower limit of detection was observed for 355 nm hydrogen than with 532 nm but it also was still above the flammability limit. The inability to achieve detection below the flammability limit prompted an examination of various optical configurations to increase collection efficiency for scattered Raman-shifted photons. Improvements in signal response were found to be more dependent on the dimensions of collection optics than pulse energy. This was an encouraging result as field implementation of Raman scattering will require the use of lower energy sources. In addition, scaling in Raman sensitivity was found with the optic dimension. Limits of detection for hydrogen of 1.94% and 0.76% by volume were achieved at pulse energies of 125 mJ/pulse and 250 mJ/pulse demonstrating the ability to detect hydrogen below its flammability limit. While demonstrating encouraging metrics for hydrogen detection, two issues are noted for remote detection by Raman scattering for field detection applications. The first issue is ignition of the hydrogen sample must be prevented in field detection by ensuring the laser beam does not generate an optical breakdown on any substrates on which the laser impinges around the sample volume. Second, due to low Raman scattering intensities, detection at large distance may or may not be limited. An increase in sampling distance will result in decreased scattering intensities due to a decreased solid angle of collection but a reduction in background noise will also result with the increased distance. Therefore, the change in signal-to-noise at large detection

distances is difficult to predict. A field detection system must be tested over a range of detection distances before implementation to ensure an adequate signal-to-noise ratio is achievable for effective hydrogen detection and monitoring.

The second technique examined in this work was laser-induced breakdown spectroscopy. This form of atomic spectroscopy was examined because of its ability to detect species in the parts per million range and its ability to provide real-time point sensing with a simple optical configuration. Gas phase and substrate-initiated LIBS were both examined to determine LIBS hydrogen detection ability. Both approaches exhibited a linear response to changing concentrations of hydrogen with similar low limits of detection around 20 ppm and comparable plasma characteristics. Substrate-initiated LIBS was determined to be the better candidate for practical hydrogen detection because detection was achieved at a lower pulse energy of 55 mJ/pulse which is more suitable for field implementation. A study of the detection response of substrate-initiated LIBS to substrate degradation suggested a possible correlation between the degree of surface ablation and detection response exhibiting one possible drawback to the use of surface-initiated LIBS for hydrogen detection. An issue noted for both LIBS approaches was the need to alleviate or account for other sources of hydrogen in the sample since LIBS is an atomic technique. Simple solutions to this requirement are the use of a liquid nitrogen cold trap to condense out water vapor and other sample pollutants or multi-species algorithms to account for ambient species concentrations. Finally, any implementation of LIBS should be conducted in a sampling chamber with all inlets below the quenching diameter for hydrogen (~ 0.61 mm) to prevent ignition of hydrogen in air. In addition,

the sample cell volume should be minimized and a pressure regulator installed to safely minimize and relieve the effects of a possible hydrogen ignition inside the cell.

Overall, both Raman scattering and laser-induced breakdown spectroscopy satisfied the criteria presented for effective hydrogen detection by demonstrating detection limits below the hydrogen flammability limit with high sensitivity. In addition, both exhibited a broad detection range and relatively simple implementation with a real-time response to changing hydrogen concentrations. For these reasons, spontaneous Raman scattering and laser-induced breakdown spectroscopy are concluded to be viable techniques for hydrogen detection and monitoring allowing for effective remote and point sensing respectively.

With the demonstration of both spontaneous Raman backscattering and LIBS as sensitive analytical techniques for practical hydrogen detection, the next phase of the investigation is to build and test field detection devices for use in monitoring of hydrogen pipelines and storage facilities. Future activities should include:

1. Further investigation of the effects of surface ablation on LIBS signal response to determine the source of response variation after repeated plasma sampling and the associated signal-to-noise ratios and limits of detection.
2. Investigation of the effect of surface contamination of the LIBS substrate on detection response.
3. Testing of a cold-trap for elimination of ambient water vapor and other pollutants from LIBS hydrogen samples.

4. Evaluation of the necessary spectral bandwidth and resolution for Raman detection to support the design of compact monochromators for the field system.
5. Correlation of the change in the signal-to-noise ratio with a wide range of field sampling distances for remote Raman detection.
6. Examination of a hybrid system using both techniques to achieve simultaneous remote and point sensing for more effective hydrogen leak monitoring.

With these additional activities addressed, spontaneous Raman scattering and laser-induced breakdown spectroscopy will be valuable detection and monitoring tools to support an expanding hydrogen infrastructure.

LIST OF REFERENCES

- Aguilera, J.A., J. Bengoechea, C. Aragon. Curves of growth of spectral lines emitted by a laser-induced plasma: influence of temporal evolution and spatial inhomogeneity of the plasma. *Spectrochimica Acta Part B* 58:2-3 (2003) p221-237.
- Alder-Golden, S.M., N. Goldstein, F.Bien, M.W. Matthew, M.E. Gersh, W.K. Cheng, F.W. Adams. Laser Raman sensor for measurement of trace-hydrogen gas. *Applied Optics* 31:6 (1992) pp831-835.
- Amos, W.A. Costs of storing and transporting hydrogen. National Renewable Energy Laboratory (NREL) Golden, CO, November 1998.
- Arbab, A., A. Spetz, I. Lundstrom. Gas sensors for high-temperature operation based on metal-oxide silicon carbide (MOSIC) devices. *Sensors and Actuators B* 15:1-3 (1993) pp19-23.
- Armgarth, M., C. Nylander. Blister formation in Pd gate MIS hydrogen sensors. *IEEE Electron Device Letters* 3 (1982) pp384-386.
- Audibert, M., J. Lukasik. Observation of stimulated Raman scattering between $\nu=1$ and $\nu=2$ levels in hydrogen gas. *Optics Communications* 21:1 (1977) pp137-138.
- Ausubel, J.H. Where is energy going? *Industrial Physicist* (2000) pp 16-19.
- Baranska, H., A Labudzinska, J. Termanski. *Laser Raman Spectrometry: Analytical Applications*. Ellis Horwood Limited. Chichester, England 1987.
- Baranzahi, A., A. Spetz, B. Anderson, I. Lunstrom. *Sensors and Actuators B* 26 (1996) p165.
- Barbieri, S., J. Pellaux, E. Studemann, D. Rosset. Gas detection with quantum cascade lasers: an adapted photoacoustic sensor based on Helmholtz resonance. *Review of Scientific Instruments* 73:6 (2002) pp2458-2461.
- Barrett, J. Generation of coherent anti-Stokes rotational Raman radiation in hydrogen gas. *Applied Physics Letters* 29:11 (1976) pp722-724.
- Basu, S., A. Dutta. Modified heterojunction based on zinc-oxide thin-film for hydrogen gas sensor application. *Sensors and Actuators B* 22:2 (1994) pp83-87.

- Bearzotti, A., C. Caliendo, E. Verona, A. D'Amico. Integrated optic sensor for the detection of H₂ concentrations. *Sensors and Actuators B* 7 (1992) pp685-688.
- Bevenot, X., A. Trouillet, C. Veillas, H. Gagnaire, M. Clement. Hydrogen leak detection using an optical fibre sensor for aerospace applications. *Sensors and Actuators B* 67 (2000) pp57-67.
- Bevenot, X. A. Trouillet, C. Veillas, H. Gagnaire, M. Clement. Surface plasmon resonance hydrogen sensor using an optical fibre. *Measurement Science and Technology* 13 (2002) pp118-124.
- Bloembergen, N., G. Bret, P. Lallemand. A. Pine, P. Simova. Controlled stimulated Raman amplification and oscillation in hydrogen gas. *IEEE Journal of Quantum Electronics* QE-3:5 (1967) pp197-201.
- Butler, M., R. Buss. Kinetics of the micromirror chemical sensor. *Sensors and Actuators B* 11 (1993) pp161-166.
- Caranza, J.E., D.W. Hahn. Sampling statistics and considerations for single-shot analysis using laser-induced breakdown spectroscopy. *Spectrochimica Acta Part B* 57:4 (2002) pp 779-790.
- Chadwick, B., M. Gal. Enhanced optical detection of hydrogen using the excitation of surface plasmons in palladium. *Applied Surface Science* 69 (1993) pp135-138.
- Chen, L., G. Hunter, P. Neudeck, G. Bansal, J. Petit, D. Knight. Comparison of interfacial and electronic properties of annealed Pd/SiC and Pd/SiO₂/SiC Schottky diodes. *Journal of Vacuum Science and Technology A* 15:3 (1997) pp1228-1234.
- D'Amico, A., E. Verona. SAW gas sensors. *Sensors and Actuators* 17 (1989) pp55-66.
- Davis, C., E. Carome, M. Weik, S. Ezekiel, E. Einzig, *Fiberoptic Sensor Technology Handbook*. Optical Technologies, 1986.
- De Groot, W.A. The use of spontaneous Raman scattering for hydrogen leak detection. NASA Contractor Report 195373, AIAA-94-2983, August 1994.
- Decker, C., W. Mori, T. Katsouleas, D. Hinkel. Spatial temporal theory of Raman forward scattering. *Physics of Plasmas* 3:4 (1996) pp1360-1372.
- Dobos, K., M. Armgarth, G. Zimmer, I. Lundstrom. The influence of different insulators on palladium-gate metal-insulate-semiconductor hydrogen sensors. *IEEE Transactions on Electronic Devices* 31:4 (1984) p508-510.
- Dong, S., F. Bai, J. Li, D. Viehland. A piezoelectric-sound-resonance cavity for hydrogen gas detection. *IEEE Transactions on Ultrasonics, Ferroelectrics, and Frequency Control* 50:9 (2003) pp 1105-1113.

Duardo, J., F. Johnson, L. Nugent. Some new aspects in stimulated Raman scattering from hydrogen gas. *IEEE Journal of Quantum Electronics* QE-4:6 (1968) pp397-403.

Dudragne, L., P. Adam, J. Amouroux. Time resolved laser-induced breakdown spectroscopy: application for qualitative and quantitative detection of fluorine, chlorine, sulfur, and carbon in air. *Applied Spectroscopy* 52:10 (1998) pp1321-1327.

Dunn, Seth. Hydrogen futures: toward a sustainable energy system. *International Journal of Hydrogen Energy* 27 (2002) pp 235-264.

Elam, Carolyn C., C.E.G. Padro, G. Sandrock, A. Luzzi, P. Lindblad, E.F. Hagen. Realizing the hydrogen future: the International Energy Agency's efforts to advance hydrogen energy technologies. *International Journal of Hydrogen Energy*. 28 (2003) pp 601-607.

Energy Information Administration (EIA). Annual Energy Review 2000. Document DOE/EAI-0384. Washington, DC, 2000.

Energy Information Administration (EIA). U.S. Department of Energy. International energy outlook 2001. Washington, D.C., 2001 pp 1-6.

Fischer, M., H. Eichert. Safety aspects of hydrogen energy. Hydrogen as an energy carrier. C.J. Winter and J. Nitsch eds. Springer-Verlag. Berlin, 1988.

Frommhold, L., J. Poll, R. Tipping. Collision-induced Raman trace spectra of pairs of H₂ molecules. *Physical Review A* 46:5 (1992) pp2955-2958.

Ghosh, S., S. Bhattacharyya, S. Saha. Polarization and nonadiabatic effects on resonance enhanced stimulated Raman Scattering in H₂. *Journal of Chemical Physics* 107:14 (1997) pp5332-5344.

Goltsov, V.A., T.N. Veziroglu. A step on the road to hydrogen civilization. *International Journal of Hydrogen Energy* 27 (2002) pp 719-723.

Griem, H.R., *Spectral Line Broadening by Plasmas*. Academic Press. New York, 1974.

Griffin, T., G. Breznik, C. Mizell, W. Helms. A fully redundant on-line mass spectrometer system used to monitor cryogenic fuel leaks on the space shuttle. *NASA Technical Briefs* 2002.

Hamagami, J., Y. Oh, Y. Watanabe, M. Takata. Preparation and characterization of an optically detectable H₂ gas sensor consisting of Pd/MoO₃ thin films. *Sensors and Actuators B* 13-14 (1993) pp281-283.

Hancock, R., K. Bertagnolli, R. Lucht. Nitrogen and hydrogen CARS temperature measurements in a hydrogen/flame using a near-adiabatic flat-flame burner. *Combustion and Flame* 109 (1997) pp322-331.

Hoffman, P. *Tommorrow's Fuel: Hydrogen, Fuel cells, and the Prospect for a Cleaner Planet*. MIT Press. Cambridge, M.A, 2001.

Hohreiter, V., J.E. Carranza, D.W. Hahn. Temporal analysis of laser-induced plasma properties as related to laser-induced breakdown spectroscopy. *Spectrochimica Acta Part B* 59 (2004) pp 327-333.

Hord, J. *Is hydrogen safe?* NBS Technical Note 690. Institute for Basic Standards, National Bureau of Standards. Bolder, Colorado, 1976.

Huo, Y., K. Shimizu, T. Yagi. Vacuum ultraviolet generation by anti-Stokes Raman scattering of KrF laser radiation in H₂. *Journal of Applied Physics* 72:8 (1992) pp3258-3263.

Hydrogen Technical Advisory Panel (HTAP). *Fuel Choice for Fuel Cell Vehicles*. Government Printing Office. Washington, D.C., May 1999.

Ingle, J.D. Jr., S.R. Crouch. *Spectrochemical Analysis*. Prentice Hall. Upper Saddle River, New Jersey, 1998.

Intergovernmental Panel on Climate Change (IPCC). *Climate Change 2001: The Scientific Basis, Summary for Policymakers, Working Group I Contribution to the Third Assessment Report of the IPC*. Geneva, 2001.

Ito, K., T. Ohgami. Hydrogen detection based on coloration of anodic tungsten oxide film. *Applied Physics Letters* 60 (1992) pp938-940.

Jakubik, W.P., M.W. Urbanczyk, S. Kochowski, J. Bodzenta. Bilayer structure for hydrogen detection in a surface acoustic wave sensor system. *Sensors and Actuators B* 82 (2002) pp265-271.

Kang, W., Y. Gurbuz. Comparison and analysis of Pd- and Pt-GaAs Schottky diodes for hydrogen detection. *Journal of Applied Physics* 75:12 (1994) pp817-8181.

Kang, W., Y. Gurbuz, J. Davidson, D. Kerns. A polycrystalline diamond thin-film-based hydrogen sensor. *Sensors and Actuators B* 25:1-3 (1995) pp421-425.

Kobayashi, H., K. Kishimoto, Y. Nakato. Reactions of hydrogen at the interface of palladium titanium-dioxide Schottky diodes as hydrogen sensors, studied by workfunction and electrical characteristic measurements. *Surface Science* 306:3 (1994) pp393-405.

Krylov, V., A. Rebane, D. Erni, O. Ollikainen, U. Wild. Stimulated Raman amplification of femtosecond pulses in hydrogen gas. *Optics Letters* 24:21 (1996) pp2005-2006.

Lallemant, P., P. Simova, G. Bret. Pressure-induced line shift and collisional narrowing in hydrogen gas determined by stimulated raman emission. *Physical Review Letters* 17:19 (1966) pp1239-1241.

- Lallemand, P. and P. Simova. Stimulated Raman spectroscopy in hydrogen gas. *Journal of Molecular Spectroscopy* 26 (1968) pp262-276.
- Long, Derek A. *The Raman Effect*. John Wiley and Sons. West Sussex, England 2002.
- Lundstrom, K.I., S. Shivaraman, C. Svensson. Hydrogen-sensitive Pd-gate MOS-transistor. *Journal of Applied Physics* 46:9 (1975) pp3876-3881.
- Lundstrom, K.I., C. Svensson. Gas-sensitive metal gate semiconductor devices. *Solid State Chemical Sensors*. eds. J. Janata and R. J. Huber. Academic Press. New York, 1985.
- Marland, G., T.A. Boden, R.J. Andres. Global, regional, and natural fossil fuel emissions. *Trends: a compendium of data on global change*. Carbon Dioxide Information Analysis Center. Oak Ridge, Tennessee, 2000.
- McAuliffe, Charles. *Hydrogen and Energy*. Gulf Publishing Company. Houston, Texas 1980.
- Melaina, M.W. Initiating hydrogen infrastructures: preliminary analysis of a sufficient number of initial hydrogen stations in the U.S. *International Journal of Hydrogen Energy*. 28, 2003, pp 743-755.
- Meng, L., K. Repasky, P. Roos, J. Carlsten. Widely tunable continuous-wave Raman laser in diatomic hydrogen pumped by an external-cavity diode laser. *Optics Letters* 25:7 (2000) pp472-474.
- Morozov, V., A. Olenin, V. Tunkin. Quasi-rotational spectral structure of optical radiation due to stimulated Raman scattering and parametric processes in high-pressure hydrogen. *Applied Physics B* 67 (1998) pp573-576.
- Nafie, L. Theory of Raman scattering. *Handbook of Raman Spectroscopy*. ed. Lewis, I., H. Edwards. Marcel Dekker, Inc. New York, 2001.
- Oksengorn, B. Observation of coherent beats in backward stimulated Raman scattering. *Optics Communications* 97 (1993) pp79-82.
- Oki, Y., S. Nakazono, Y. Nonaka, M. Maeda. Sensitive H₂ detection by use of thermal-lens Raman spectroscopy without a tunable laser. *Optics Letters* 25:14 (2000) pp1040-1042.
- Okuyama, S., K. Umemoto, K. Okuyama. Pd/Ni-Al₂O₃-Al tunnel diode as high concentration hydrogen gas sensor. *Japanese Journal of Applied Physics Part 1* 36:3A (1997) pp1228-1232.
- Ottens, A., W. Harrison, T. Griffin, W. Helms. Real-time quantitative analysis of H₂, He, O₂, and Ar by quadrupole ion trap mass spectrometry. *American Society for Mass Spectrometry* 13 (2002) pp1120-1128.

Papayannis, A., G. Tsirikas, A. Serafetinides. Generation of UV and VIS laser light by stimulated Raman scattering in H₂, D₂, and H₂/He using a pulsed Nd:Yag laser at 355 nm. *Applied Physics B* 67 (1998) pp563-568.

Peng, Y., Y. Tang, J. Sirkis. Hydrogen sensors based on palladium electroplated fiber bragg gratings (FBG). *Proceeding of the 13th International Conference on Optical Fiber Sensors*, Kyongju, Korea (1999) pp13-16.

Radziemski, L.J., D.A. Cremers. *Laser-Induced Plasmas and Applications*. Marcel Dekker, Inc. New York, 1989.

Romm, J. *The Hype About Hydrogen*. Island Press. Washington, 2004

Scharnagle, K., M. Eriksson, A. Karthigeyan, M. Burgmair, M. Zimmer, I. Eisele. Hydrogen detection at high concentration with stabilized palladium. *Sensors and Actuators B* 78 (2001) pp138-143.

Scharnagle, K., A. Karthigeyan, M. Burgmair, M. Zimmer, T. Doll, I. Eisele. Low temperature hydrogen detection at high concentrations: comparison of platinum and iridium. *Sensors and Actuators B* 80 (2001) pp163-168.

Schrotter, H.W., H.W. Klockner. Weber, A. *Raman Spectroscopy of Gases and Liquids*. Springer-Verlag, 1979.

Scripps Institute of Oceanography. Atmospheric CO₂ concentrations (ppmv) derived from in situ samples collected at Mauna Loa Observatory, Hawaii. La Jolla, CA, 16 August 2000.

Shukla, S., S. Patil, S.C. Kuiry, Z. Rahman, T. Du, L. Ludwig, C. Parish, S. Seal. Synthesis and characterization of sol-gel derived nanocrystalline tin oxide thin film as hydrogen sensor. *Sensors and Actuators B* 96 (2003) pp343-353.

Simeonsson, J.D., A.W. Mizeolek. Spectroscopic studies of laser-produced plasmas formed in CO and CO₂ using 193, 266, 355, 532 and 1064 nm laser-radiation. *Applied Physics B* 59 (1994) pp1-9.

Smith, B.W., D.W. Hahn, E. Gibb, I. Gornushkin, J.D. Winefordner, *KONA Power and Particle* N0 19, 2001, p25-33.

Tan, O.K., X.F. Chen, W. Zhu. Amorphous ferroelectric thin film capacitive device for hydrogen detection. *Journal of Materials Science* 38 (2003) pp4353-4363.

Tang, Y., T. Peng, S. Lee, J. Sirkis, B. Childers, J. Moore, L. Melvin. Characterization of fiber bragg gratings (FBG) based palladium tube hydrogen sensors. *Proceedings of the 13th International Conference on Optical Fiber Sensors*, Kyongju, Korea 13 (1999).

Tardy, P., J. Coulon, C. Lucat, F. Menil. Dynamic thermal conductivity sensor for gas detection. *Sensors and Actuators B* 98 (2004) pp63-68.

Tobiska, P., O. Hugon, A. Trouillet, H. Gagnaire. Integrated optic hydrogen sensor based on SPR on palladium. *Sensors and Actuators B* 74 (2001) pp168-172.

UN Development Programme (UNDP), UN Department of Economic and Social Affairs (UNDESA), and World Energy Council (WEC). *World Assessment Report*. 2000.

U.S. Department of Energy (DOE). *Hydrogen Posture Plan: An Integrated Research, Development, and Demonstration Plan*. Government Printing Office, Washington D.C., 2004.

Uwira, V., A. Schutze, D. Kohl. Detection of low hydrogen concentrations by a Cu-Pc sensor. *Sensors and Actuators B* 26-27 (1995) pp153-157.

Vasa, N., A. Hatada, S. Nakazono, Y. Oki, M. Maeda. Feasibility of nonlinear Raman lidar based on stimulated Raman gain spectroscopy without a tunable laser. *Applied Optics* 41:12 (2002) pp2328-2332.

Villeneuve, D., H. Baldis. Observation of forward Raman scattering enhanced by backward Raman scattering in a laser plasma. *Physics of Fluids* 31:6 (1988) pp1790-1794.

Wade, L. *Organic Chemistry* 5th edition. Prentice Hall. Upper Saddle River, New Jersey, 2003.

Wang, X., R. Fedosejevs, G. Tsakiris. Observation of Raman scattering and hard X-rays in short pulse laser interaction with high density hydrogen gas. *Optics Communications* 146 (1998) pp363-370.

Wilkerson, C., E. Sekreta, J. Reilly. Raman shifting of picosecond light pulses in hydrogen gas. *Applied Optics* 30:27 (1991) pp3855-3861.

Williamson, C.K., R.G. Daniel, K.L. McNesby, A.J. Miziolek. Laser-induced breakdown spectroscopy for real-time detection of halon alternative agents. *Analytical Chemistry* 70:6 (1998) pp1186-1191.

Winter, Carl-Jochen. *From fossil fuels to energies-of-light. On Energies of Change-the Hydrogen Solution*. Munich: Gerling Akademie Verlag, (2000) pp67-82

Wong, Y.M., W.P. Kang, J.L. Davidson, A. Wisitsora-at, K.I. Soh. A novel microelectronic gas sensor utilizing carbon nanotubes for hydrogen gas detection. *Sensors and Actuators B* 93 (2003) pp 327-332.

BIOGRAPHICAL SKETCH

Allen Joseph Ball was born on January 13, 1980, in Pella, Iowa, the only child of John and Beth Ball. Allen was predominantly raised in the Midwest prior to relocation to Florida for high school. In August 1998, he began his undergraduate studies at the University of Florida. Allen graduated with a Bachelor of Science degree in mechanical engineering with honors in December 2002 and decided to continue his studies in graduate school at the University of Florida. This work is the culmination of his pursuit of a Master of Science degree in mechanical engineering.